THREE-DIMENSIONAL STRONG ACOUSTO-OPTIC INTERACTION THEORY

BY

MARK D. MCNEILL

Dissertation submitted to the Faculty of the

Virginia Polytechnic Institute and State University

in partial fulfillment of the requirements for the degree of

DOCTOR OF PHILOSOPHY

in

Electrical Engineering

APPROVED:

T.-C. Poon, Chairman

W. A. Davis

I. M. Besieres

A. Safaai-Jazi

G. J. Indebetouw

May, 1996
Blacksburg, Virginia

Key Words: Acousto-Optic, Diffraction, Three-Dimensional

THREE-DIMENSIONAL STRONG ACOUSTO-OPTIC INTERACTION THEORY

by

Mark D. McNeill

Chairman: Dr. Ting-Chung Poon

Electrical Engineering

(ABSTRACT)

This dissertation presents two different three-dimensional theories that examine the interaction between light and "strong" sound fields. Strong refers to a sound field strength sufficient to deflect most of the incident light into the first diffracted order, but not strong enough to induce nonlinear behavior in the acousto-optic cell. Primary emphasis is placed on deriving and experimentally verifying theories that predict the interaction process. All strong interaction theories to date consider only two transverse dimensions, where sound and light travel predominantly in the x and z directions, respectively. Our theories employ "split-step" type numerical methods to solve the theoretical equations derived for the interaction. The first method is called the Fourier-Optics approach and applies directly to a nondiffracting sound column. An incident light beam propagates through the cell by alternating between interaction and diffraction. The second method is called the Wave-Equation approach because it solves the coupled differential equations derived from Maxwell's equations. This method differs from the Fourier-Optics approach because it includes sound field diffraction into the interaction process. Throughout both theories we assume the sound field represents a bulk acoustic wave. Theoretical predictions show and experimental measurements verify

that adding the y dimension into the interaction process enables one to examine acousto-optic interaction effects in a different way. Specifically, we show that the height (measured along the y-direction) of the sound beam contributes to distortions of the zero diffracted order not predicted by other theories. We also show that the y-dimension contributes to a reduction in diffraction efficiency as the light beam is incident at greater distances away from the acoustic transducer. This effect while observed in practice has not been shown in theory by previous acousto-optic interaction theories. Both theoretical predictions and experimental results are presented below.

Dedication

I dedicate the body of this work to my wife, Addie, my first child, Ashley, and my parents, Oscar and Dorothy McNeill. Each of you provide inspiration in my life, and without you my life would have no purpose.

Acknowledgements

I first offer my thanks to God for without his guidance and strength, I would not have been able to endure the peaks and valleys of this journey. My heart felt appreciation goes to my wife, Addie, and our daughter, Ashley. Addie stood as solid support from beginning to end and never wavered in her belief in me. I also thank my parents for their continued guidance and support.

I extend my deepest appreciation to the advising committee. I want to especially thank Prof. T.-C. Poon for supervising my work and accepting me into his group when my initial optics background was limited. He served as an excellent mentor and friend. I thank Prof. W. Davis for providing me the framework and the motivation to complete this task. Likewise, I appreciate the conversations and insightful comments given to me by Prof. Safaai-Jazi. To have Prof. Besieres, who taught me the fundamentals of Electromagnetic theory, on my committee was especially rewarding for me. I thank Prof. G. Indebetouw for giving me a different view of Fourier optics and a better understanding of the physics involved. I also thank Prof. Partha Banerjee of the University of Alabama at Huntsville for his comments and suggestions. He was especially helpful with the wave-equation approach. A special thanks goes to Prof. Wayne Scales for agreeing to sit in on my defense, for his willingness to be a role-model, and for serving as mentor during my last three years at Virginia Tech.

Special thanks goes to Martha Johnson in the graduate school and to Loretta Estes in the Electrical Engineering Department. I deeply appreciate the financial support given by

the state of Virginia through the State Graduate Dean's fellowship. I give equal thanks to NASA's George C. Marshall Space Flight Center for support through their GSRP fellowship. I also wish to thank the members of the Optical Image Processing Laboratory. Lastly, I express the most sincere gratitude to my circle of support: Derrek Dunn, John Wicks, Andre Cropper, Art Williams, Joy Poindexter, Rosendo Molina, and the Black Graduate Student Organization.

Table of Contents

List of Figures

1. Introduction

Acousto-optic interaction plays an important role in practical devices. These devices typically operate as deflectors, modulators, switches, spectrum analyzers, and mode couplers. A French physicist named Leon Brillouin[1] made the original prediction regarding the interaction between light and sound in 1922. Following this discovery many theories have explained the interaction process. Past treatment has often cast the process into two different regimes based on the strength of the sound field. Standard terminology refers to interaction between a light field and a weak sound field as weak interaction and interaction with a strong sound field as strong interaction. While investigators have historically considered the two regimes, their theories often make simplifying assumptions regarding light and sound field profiles due to the mathematical difficulty involved. Most theories generally modeled the process as a physically unrealistic plane wave of light incident upon a rectangular sound column. Scientists began to incorporate bounded light beams (usually Gaussian) into existing theories when lasers began to replace other light sources in acousto-optic experiments[2,3,4,5]. Korpel and Poon[6] developed a more general theory that includes arbitrary light and sound fields. The formalism, however, restricts acousto-optic interaction to two dimensions, one transverse and one longitudinal (i.e. The interaction is restricted to the x-z plane).

The purpose of this work is to develop a formalism that addresses three-dimensional strong acousto-optic Bragg diffraction for arbitrary light and sound fields. For the first time, we include the 'y' coordinate and sound field diffraction into the interaction process. Our

analysis focuses on strong interaction because it is the preferred mode of operation in many practical situations. We employ two different split-step type algorithms to accurately model the process. Both theories employ a technique that is closely related to the split-step Fourier technique of Hardin and Tappert[7], and used by Hasegawa and Tappert[8,9] to calculate nonlinear pulse propagation in dispersive fibers. Fisher and Bischel used a similar method to investigate one-dimensional self-phase modulation[10]. In both cases, the advantage of the technique is that diffraction is calculated in the Fourier domain and interaction in the spatial domain. Each action requires only straightforward multiplications in its prospective domain. In this respect, our method is comparable to that used by Bojarski[11] to calculate scattering by an external potential. Other investigators used Fourier transform methods to calculate propagation in three-dimensional linear media[12] and two-dimensional nonlinear media[13]. Yevick and Thylen used a split-step method to investigate the propagation of light beams through rectangular phase gratings.[14] They produced a detailed set of figures and tables to validate the method and quantify its accuracy. Although an acousto-optic cell can be modeled as a rectangular grating (in the limit), our problem differs because it investigates arbitrary sound fields and strong acousto-optic interaction. Venzke et.al.[15] developed a method similar to the Fourier-optics approach discussed in Chapter 5. Although their method is similar, we clearly demonstrate that our algorithm applies to three dimensions. Lastly, the most recent application of the split-step numerical technique is illustrated in the work by Hare and Morrison where they apply the "multislice" method (i.e. their version of the split-step method) to near-field X-ray diffraction.[16]

We refer to the first split-step method as the Fourier-optics approach. This method divides the acousto-optic cell into multiple slices and propagates the optical field through each slice twice. The slice is homogeneous and diffracting during the first step and inhomogeneous and nondiffracting during the next step. Fresnel diffraction is used to propagate an incident light beam through the width of one homogeneous slice. The next step multiplies this resultant field by a thin phase grating (inhomogeneous slice) representing sound field perturbations within that slice. The Fourier-optics approach allows two transverse dimensions to interact within the acousto-optic cell. However, the formalism still uses an unrealistic bounded sound column model for the sound field.

The second split-step algorithm is referred to as the wave-equation approach. We begin with Maxwell's equations and derive the three-dimensional wave equation for strong acousto-optic interaction. After introducing harmonic variations into the incident light and sound fields, we derive an infinite set of coupled differential equations. This system of equations is solved with a modified split-step algorithm, where Fresnel diffraction propagates each order generated by the differential equations. The interaction portion of the formalism multiplies the sound field by orders adjacent to each desired diffracted order (i.e., to calculate the interaction for order 1, the sound field must multiply orders 0 and 2). Section 5.3 discusses this in greater detail. This algorithm incorporates diffraction of the sound field into the theory and allows the distance between the input light beam and the acoustic transducer to be adjusted.

To begin, chapter 2 provides a historical sketch of different acousto-optic formalisms

that generally falls into the following four basic categories:

1. Plane wave of light and plane wave of sound,
2. Gaussian light profile in 2-D and plane wave of sound,
3. Gaussian light profile in 2-D and Gaussian sound profile,
4. Gaussian light and sound profiles each in 3-D.

The review provides greater insight into the development of acousto-optics. Chapter 3 provides fundamental approaches to the interaction process and introduces the Bragg and Raman-Nath regimes. This section also introduces basic parameters used in acousto-optics such as the Bragg angle, Klien Cook parameter, and Doppler shift. Chapter 4 presents a transfer function formalism to investigate the interaction problem. This method applies to category (2) and is used to verify two-dimensional results produced by each split-step algorithm. This section also investigates how the process evolves for strong interaction and large Q values (wide interaction regions). Chapter 5 presents a theoretical discussion for the Fourier-optics and wave-equation approaches. It includes simulation results and comparisons to the method outlined in chapter 4. This section stresses the additional benefits of each formalism and highlights the contributions these methods add to better understand acousto-optic interaction. Chapter 6 explains the experimental setup used to measure the profiles of the diffracted beams (i.e. minus-1 order, zero order, first order, and second order). We measure a two-dimensional profile on the x-y plane at a distance z away from the transducer. Authors of previous methods measured only a slice of the diffracted orders along the y equal zero axis because their theories did not account for acousto-optic effects along the y

direction. We present agreement between theoretical predictions and actual measurements by comparing calculated intensity distributions to measured two-dimensional profiles taken at a convenient distance away from the transducer. Chapter 7 gives a detailed account of how each numerical method help to better define the interaction between light and sound. It draws conclusions from the previous chapters and provides the reader with a detailed summary of all findings concerning acousto-optic interaction. It summarizes by restating major contributions and discussing future research directions.

2. Literature Review

Acousto-optics is perhaps the most reinvented, reapplied, and renamed scientific field in history. Each new formalism attempts to provide a firm mathematical theory and a deeper physical insight into the overall process. Historically, this has led to duplications of original material. The primary reason for this is that acousto-optics was created while investigating a purely physical problem. Shortly after being placed onto its initial theoretical platform, the field quickly developed into a purely mathematical area. This treatment continued until the invention of the laser in the 1960's. Subsequently, bulk acousto-optics gained new life in the technology arena, and scientist began to reformulate existing theories into mathematical models that provided insight into their experiments.

As stated in chapter 1, acousto-optics developed from the original research of Brillouin. His original theory predicted a phenomenon closely related to x-ray diffraction in crystals. In acousto-optic diffraction, plane waves of light striking acoustically induced planes of compression and rarefaction at a certain critical angle will be partially reflected. Unlike x-ray diffraction, however, he stated that there would be only one critical angle (Bragg angle) because the spatial structure of acoustically induced density variations is essentially sinusoidal and hence contains no space harmonic components. In addition, Brillouin predicted that reflected light would be Doppler shifted by an amount equal to the sound frequency because the reflecting grating moves at the sound velocity.

The first experiment demonstrated that many orders of reflected light were generated,

indicating the presence of a range of critical angles. Debye and Sears[17] suggested that this was due to the generation of higher harmonics of the sound. Lucas and Biquard[18], on the basis of calculated ray trajectories, showed that the ray distribution of light leaving the column of sound was periodic in space. They concluded that the resulting effect would be similar to multiple orders produced by a static thin phase grating. Brillouin[19], in a second paper, suggested that the multiple orders only occurred with the application of high sound intensity (strong interaction), a condition for which his original weak interaction theory did not apply. He suggested that the multiple order effect might be interpreted as a rescattering of diffracted light. Although Brillouin did not solve the strong interaction problem in detail, he showed that it could be formulated in terms of a Mathieu equation (i.e. differential equations with time varying coefficients). The solution of which would contain multiple orders of light scattered into the experimentally observed directions.

In 1935 Raman and Nath[20] presented an analysis based on earlier work by Lord Rayleigh[21] concerning diffraction by a corrugated surface. They assumed that the sound column would function as a two-dimensional thin phase grating in the direction of light propagation. Their theory correctly predicted the Bessel function intensity variation of various orders as a function of sound pressure. While in this first analysis the light beam was assumed to be incident perpendicular to the sound column, a second article[22] treated the case of oblique incidence. Their next publication[23] examined the frequency change in the diffracted light. In a fourth article[24] they formulated the problem in terms of a wave equation defining propagation of incident light in an acoustically perturbed medium. They went on to derive

an infinite set of coupled differential equations which described the spatial behavior of various orders traversing the sound beam. In deriving these equations it was assumed that the light field was incident perpendicular to the sound column. There was no limitation on the interaction length. Raman and Nath showed that if the sound column was sufficiently thin, the infinite set of equations led to the same solution as the phase grating model. Finally, in a fifth article[25], the authors extended their theory to include light incident at arbitrary angles.

Although the infinite set of differential equations was derived by Raman and Nath in a formal way by applying the wave equation to an acoustically perturbed medium, these equations may also be derived by a intuitive approach. This was shown by Van Cittert[26], who treated the sound column as an infinite set of infinitesimally thin parallel phase gratings. Repetitive diffraction of the initial few orders through successive gratings ultimately led to the generation of infinitely many orders and defined a set of recurrent differential equations identical to those of Raman and Nath.

Many other authors have used different methods to derive similar sets of equations. Bhatia and Noble[27] formulated the problem in terms of an integral equation for the scattered field, Phariseau[28] further developed the Mathieu equation approach originally proposed by Brillouin while Extermann[29] employed a method that involved concepts used in the analysis of x-ray diffraction in crystals. Although most of these theories are considerably more complicated than the Raman-Nath and Van Cittert formulation, they only appear to differ in the method of approach. For instance, it may be shown that an extension of Van Cittert's theory to include reflected orders produce results that are identical to those obtained by

Phariseau. Generally, however, the intensity of the reflected orders is negligible and the Raman-Nath Van Cittert equations adequately describe the problem. Many investigators[30,31,32] have derived specific solutions of these equations applying to various angles of incidence, interaction lengths, and sound pressures.

Most of the theories previously mentioned restrict themselves to a two-dimensional interaction model where the sound field consists of a single plane wave (in a finite width approximation) and the incident light field is taken to be an infinitely large plane wave. The emphasis of these theories is in the description of the rescattering process using the simplest model, rather than on the weak interaction of more complicated fields. A majority of the older theories obscure the physical treatment of sound-light diffraction as a Bragg angle scattering and rescattering of individual plane wave components.

The weak interaction formalisms are of more recent origin. They arose out of a need to accurately describe such diverse phenomena as Brillouin scattering[33], beam parameter effects on Bragg diffraction[34,35] and Bragg diffraction imaging[36]. After introducing the laser, quantum mechanical considerations regarding energy and momentum in photon-phonon collision processes were incorporated into a rather simple theory[37,38,39]. Earlier theories were presented in terms of ultrasonic gratings.

As stated before, a uniform sound column model is mathematically convenient because of its periodic nature and simple boundary conditions, but it is not physically realistic. In most physical situations, a Gaussian light beam is used instead of a physically unrealistic plane wave. Second, the sound field diffracts as it propagates through the acoustic medium and

therefore cannot maintain its uniform wave front due to the finite width of the column.

An improvement in the sound column model was introduced by Leroy and Claeys[40] and by Pieper et al.[41], who assumed that the sound field had a constant but arbitrary cross-section profile. The incident light field was still a plane wave and the sound field had plane-wave fronts. The model was only slightly more realistic than the uniform sound column model.

The plane wave of light was replaced with a two dimensional Gaussian beam by misspelled Magdich and Molchanov[2] and by Chu, Kong, and Tamir.[3,4,5] Poon and Chattergee[42] introduced a transfer function formalism that was similar to the Magdich-Molchanov theory, but much easier to understand and implement. The essence of this formalism is to convert the input Gaussian beam profile into its angular plane wave spectrum by using the Fourier transform. Once in the spectrum domain, a set of coupled differential equations representing acousto-optic interaction is redefined as the transfer function for the Bragg cell. Because the set of coupled differential equations applies strictly to plane waves, it is assumed that the input Gaussian beam is made up of many plane waves, each traveling in a direction slightly different than the ideal Bragg angle. By multiplying the input angular spectrum with the acousto-optic transfer function, it is possible to obtain the angular spectrum for each diffracted order. Note, however, that although the incident light field is arbitrary, the sound field is still a physically unrealistic uniform sound column.

A more general theory was developed by Korpel and Poon[6] where both arbitrary light fields and arbitrary sound fields in two dimensions are assumed. Feynman-type diagrams are

used to describe path integrals that represent the successive scattering of the light field in the interaction region. By interpreting the path integrals in terms of complex quantum-mechanical probability amplitude densities, these paths may be simulated by using a Monte Carlo simulation.[43] The disadvantages of this method are that it is restricted to two dimensions and many paths must be evaluated to produce accurate results.

3. Background Information

3.1 Basic Concepts

Section 3.1.1 presents a quantum mechanical treatment of acousto-optic interaction. This approach accurately defines the Bragg angle, frequency shift, and operating regime for a typical configuration. The analysis presented exists in most textbooks about acousto-optics, therefore only results relevant to our study are presented. The reader is referred to references[44,45,46] for a more detailed analysis.

Section 3.1.2 specifies the physical configurations investigated in this work. Special attention is given to terminology involving two-dimensional (2-D) and three-dimensional (3-D) geometries.

3.1.1 Quantum Mechanical Description

The interaction between plane waves of light and sound can be illustrated by a momentum or wave vector diagram. This approach considers acousto-optic interaction as a collision between photons and phonons, thereby enabling the conservation of energy and momentum laws to be applied to the process. If we denote the wave vectors of incident light, scattered light, and sound by $\mathbf{k}_0$, $\mathbf{k}_1$, and $\mathbf{K}$, respectively, conservation of momentum may be written as

$$\frac{h}{2\pi}\mathbf{k}_1 = \frac{h}{2\pi}\mathbf{k}_0 + \frac{h}{2\pi}\mathbf{K}, \qquad (3.1\text{-}1)$$

where h denotes Planck's constant. From Figure 3.1a and the division of (3.1-1) by $h/2\pi$, it is apparent that the condition for wave matching to occur becomes

$$\mathbf{k}_1 = \mathbf{k}_0 + \mathbf{K}. \tag{3.1-2}$$

For most practical cases $|\mathbf{K}| \ll |\mathbf{k}_0|$, therefore the magnitude of $\mathbf{k}_1$ essentially equals that of $\mathbf{k}_0$, and the wave vector triangle shown in Figure 3.1a is nearly isosceles. Because a traveling sound wave exists in the acousto-optic cell, the frequency of the diffracted beam is Doppler shifted by an amount equal to the sound frequency. By multiplying equation (3.1-1) by $2\pi c$ (c is the speed of light) and dividing through by h, we express the conservation of energy as

$$\omega_1 = \omega_0 + \Omega, \tag{3.1-3}$$

where ω_1, ω_0, and Ω are radian frequencies of the diffracted light, incident light, and sound, respectively. Since the frequency of the diffracted light beam is upshifted by an amount equal to the sound frequency, the interaction described above is called upshifted interaction. Consider if the direction of the incident light is changed such that it is incident at an angle opposite to that for upshifted interaction as shown in Figure 3.1b. This will cause a downshift in the frequency of the diffracted light beam. Again, the conservation laws for momentum and energy can be applied, respectively, to obtain relationships similar to those expressed in equations (3.1-2) and (3.1-3), i.e.,

$$\mathbf{k}_{-1} = \mathbf{k}_0 - \mathbf{K} \tag{3.1-4}$$

and

$$\omega_{-1} = \omega_0 - \Omega, \tag{3.1-5}$$

where the (-1) subscripts indicate downshifted interaction. The closed triangles in figures 3.1a and 3.1b stipulate that plane waves of light and sound interact at a specific angle of incidence. This angle is called the Bragg angle, ϕ_B, and is given by

$$\sin(\phi_B) = \frac{K}{2k} = \frac{\lambda}{2\Lambda}, \tag{3.1-6}$$

where λ is the wavelength of light inside the acoustic cell, and Λ is the wavelength of sound. The diffracted beams differ in direction by an angle equal to $2\phi_B$ as shown by the wavevector diagrams in figure 3.1.

In actual experiments, scattering happens even though the direction of incident light is not exactly at the Bragg angle. However, maximum diffraction occurs when light is incident at the Bragg angle. The reason is that a finite length transducer does not produce ideal plane waves, and sound waves actually spread as they propagate inside the acoustic medium. As the width of the transducer decreases, the sound column will act less and less like a single plane wave, in fact, it is now more appropriate to consider it an angular spectrum of plane waves. Physical reality dictates that a complete energy transfer between the two diffracted beams is impossible because there always exists more than two diffracted beams. As shown in figure 3.2, an incident light field interacting with an arbitrary sound field produces multiple diffracted orders where $\mathbf{E}_n$ is the nth order diffracted light beam at

frequency $\omega_n=\omega_0+\Omega_n$. The generation of multiple diffracted light beams defines the so-called Raman-Nath regime. In contrast, only two diffracted orders exist in the ideal Bragg regime. The Klein-Cook parameter,

$$Q = \frac{K^2}{k}L = 2\pi\frac{\lambda}{\Lambda^2}L, \qquad (3.1\text{-}7)$$

has been defined to allow the proper classification of an acousto-optic modulator as a Bragg or Raman-Nath cell (L is the width of the transducer). The Bragg regime is defined arbitrarily as the condition when the diffraction efficiency for the first order diffracted light beam (i.e., n = 1 for upshifted diffraction or n = -1 for downshifted diffraction) equals 90 percent. Consequently, operation in the Bragg regime is defined by $Q \geq 7$.[45] Notice that for ideal Bragg diffraction, Q would have to be infinite (i.e. $L = \infty$).

3.1.2 Two and Three Dimensional Terminology

This chapter overviews the proper terminology for two-dimensional (2-D) and three dimensional (3-D) acousto-optic configurations. We use 2-D to refer to an experimental configuration with one transverse dimension and one longitudinal dimension. The incident light beam propagates in the nominal 'z' direction and the sound field propagates in the nominal 'x' direction. Figure 3.3 gives an example of the typical rectangular sound column used in most acousto-optic formalisms to date. Clearly this figure depicts a two-dimensional model where the sound field propagates in the x-direction and the light field propagates in the z-direction. Notice that cell height is neglected in this model, and therefore the 'y' dimension

of the incident light and sound fields is not incorporated into the 2-D model.

Using the same nomenclature, we use 3-D to refer to two transverse dimensions and one longitudinal dimension. Figure 3.4 shows a three-dimensional sound column that incorporates cell height into the model. The height and width of the transducer allows the sound field to possess two transverse dimensions and to receive a light field with two transverse dimensions. As evident in the figure, this terminology allows one to incorporate sound fields that vary in both the transverse y and z directions. Consequently, an arbitrary incident light beam can now interact with an arbitrary sound field. For example, it is possible to have a two-dimensional (transverse dimensions are 'x' and 'y') Gaussian light beam incident on a Bragg cell containing a two-dimensional Gaussian sound field (transverse dimensions are 'y' and 'z'). Developing a theory and providing a solution for 3-D acousto-optic interaction is the focal point of this thesis. As implied in figure 3.4, we introduce the sound field by its profile only. We do not include details about how to design acoustic transducers to produce specific sound field profiles. Our desire is to investigate how varying the transverse profile of the sound field affects the acousto-optic interaction process.

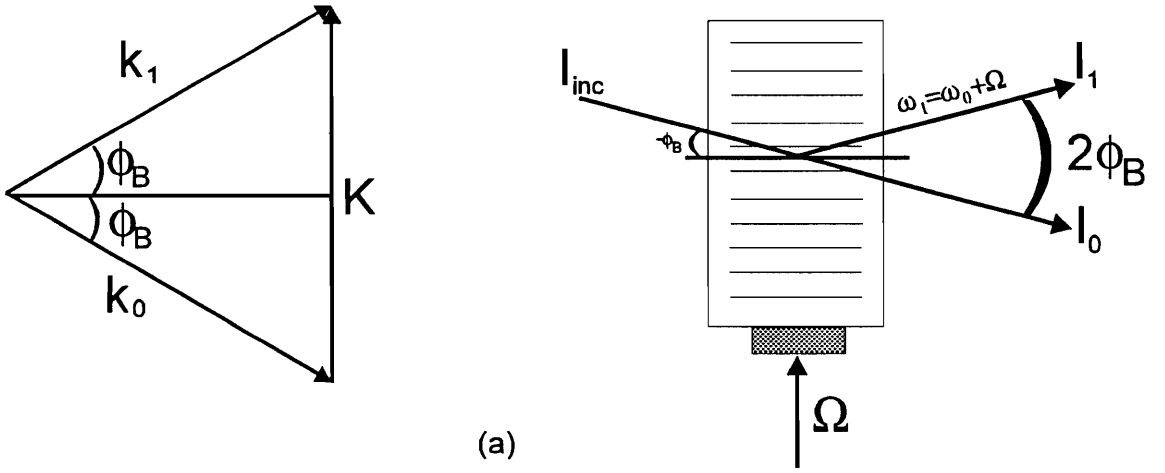

(a)

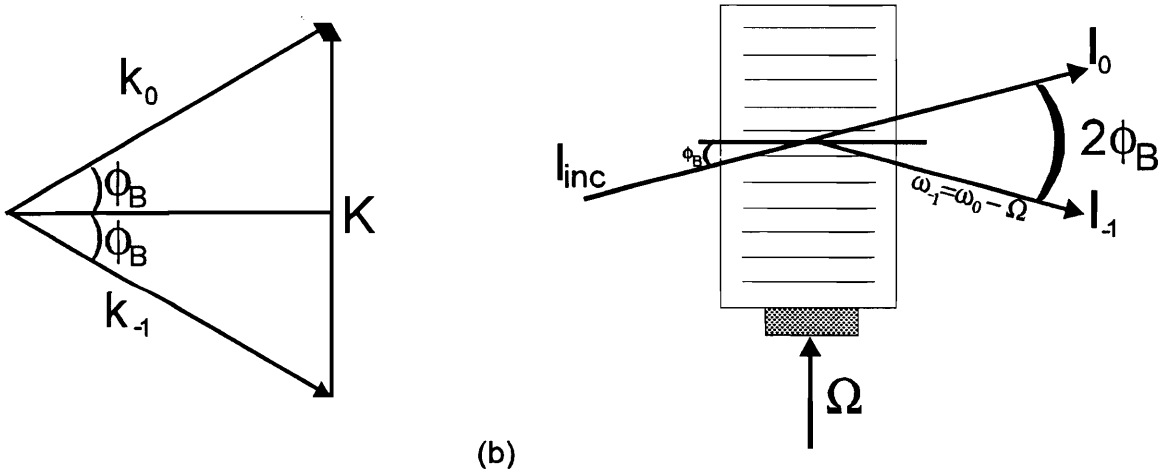

(b)

Fig. 3.1: (a) Wavevector diagram and AOM cell for upshifted Bragg diffraction. (b) Wavevector diagram and AOM cell for downshifted Bragg diffraction.

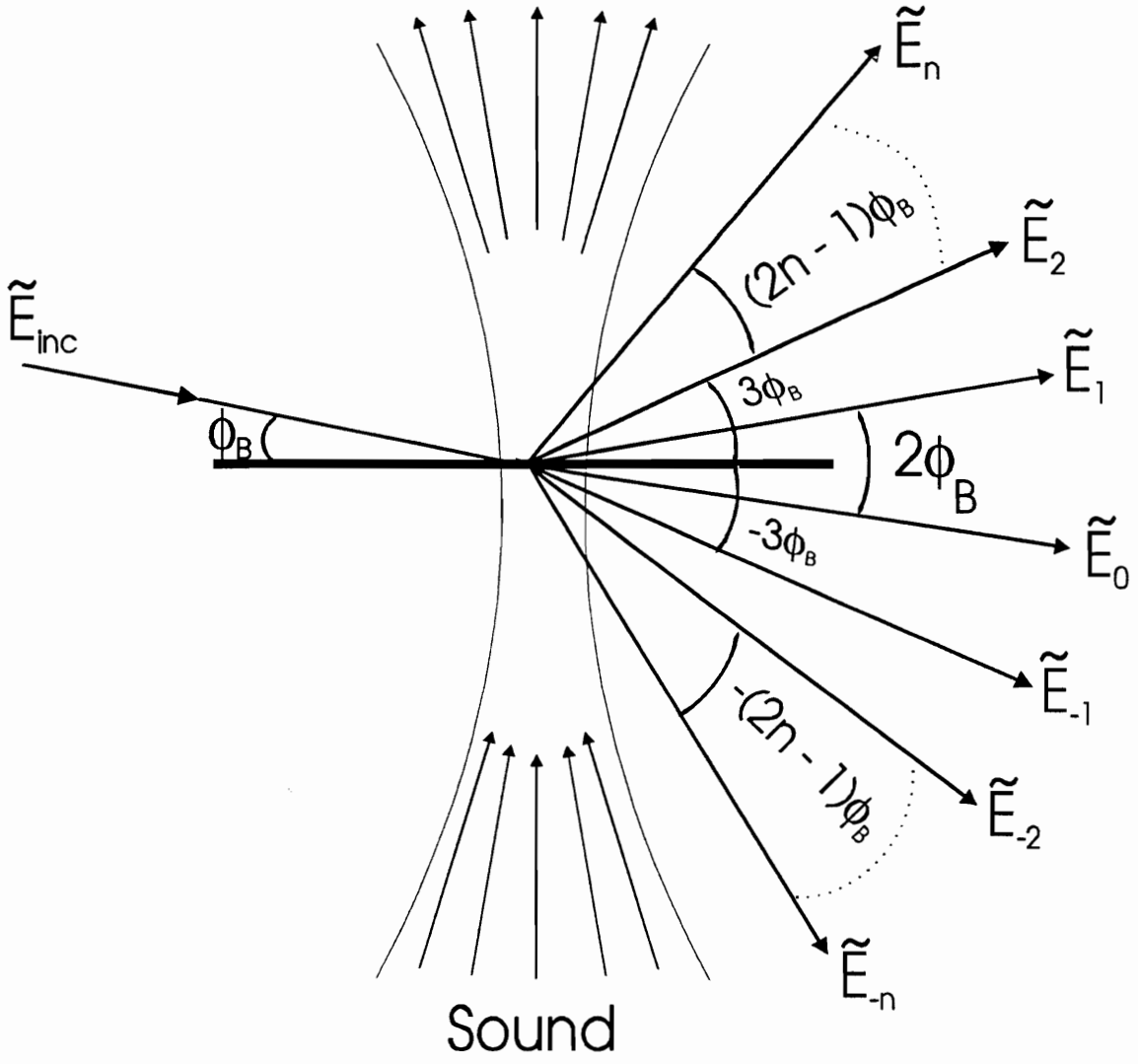

Fig. 3.2: Interaction between an optical plane-wave and an arbitrary sound beam. The multiple orders are due to the sound field specturm.

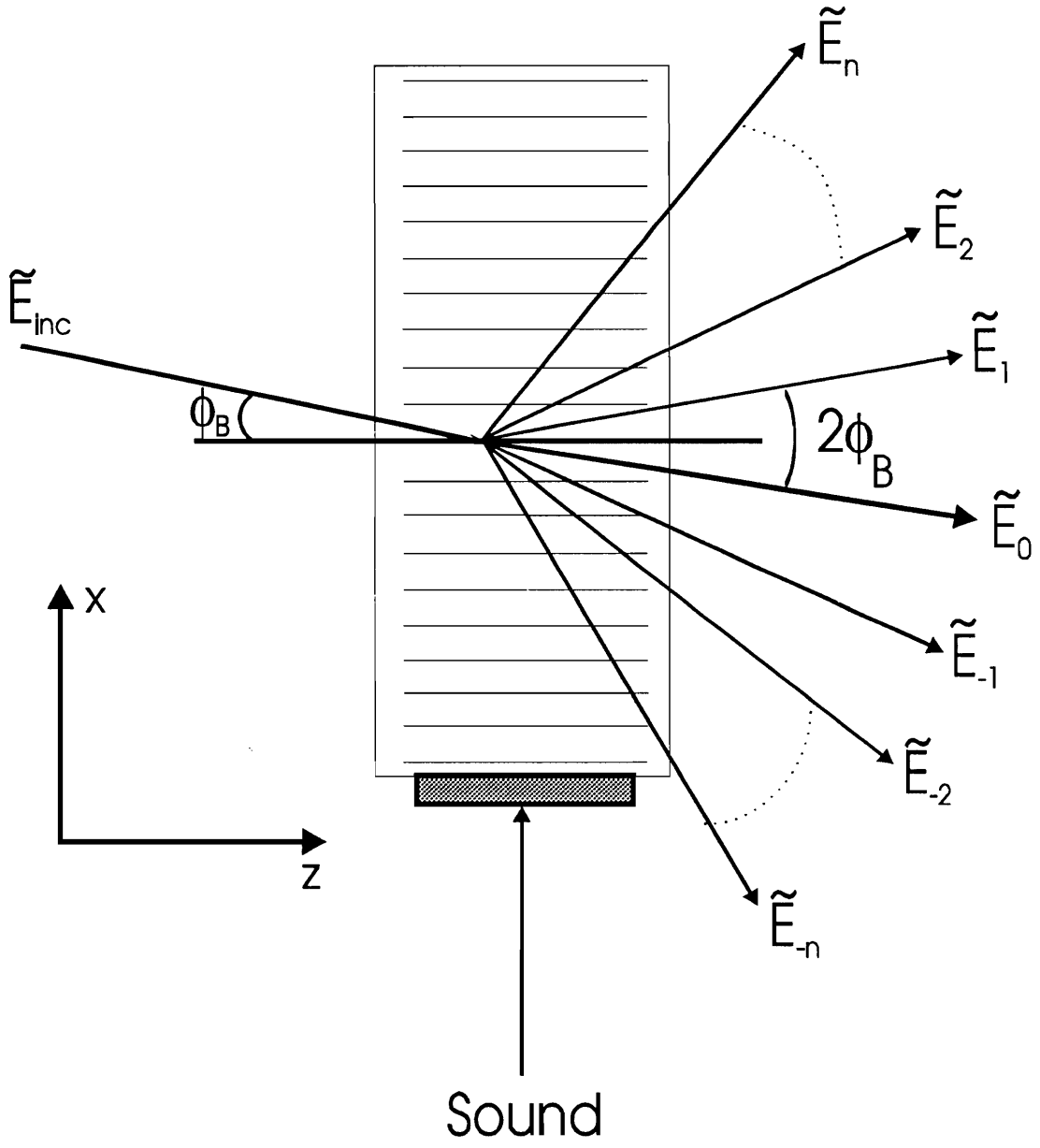

Fig. 3.3: Acousto-optic interaction between a plane-wave of light and a rectangular sound column (2-D configuration).

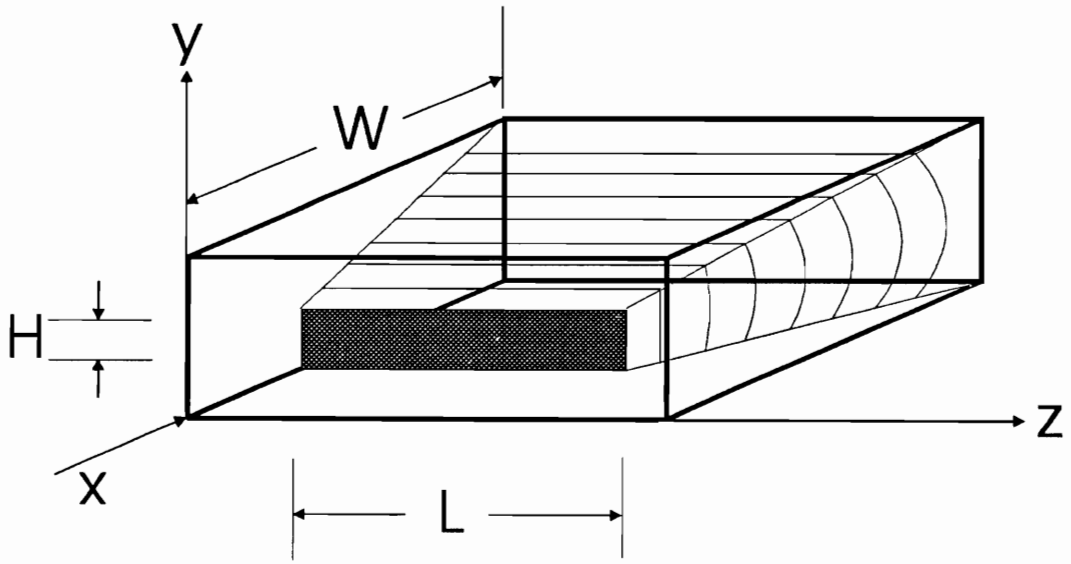

Fig. 3.4: 3-D perspective of an acousto-optic Bragg cell with curved wavefronts.

4. Strong Acousto-Optic Interaction in One Transverse Dimension

4.1 Basic Concepts

This chapter introduces the Korpel-Poon multiple scattering theory and the transfer function formalism. The significance of this method is to provide physical insight into the interaction process and to serve as a comparison algorithm for the split-step methods presented in chapter 5. The theory, however, includes one transverse dimension and one longitudinal dimension, thus making it applicable to 2-D configuration models only.

Section 4.1.1 begins with a discussion about the Korpel-Poon multiple plane wave scattering theory. Next is a description explaining how this theory generates acousto-optic transfer functions. The introduction of a Gaussian laser beam as the arbitrary incident light beam serves as a test case for the formalism. Finally, section 4.1.4 concludes with a discussion about how to predict and control beam distortion caused by acousto-optic interaction.

4.1.1 Korpel - Poon Multiple Plane Wave Scattering Theory

There are many theoretical approaches to the acousto-optic interaction problem. We have chosen the Korpel-Poon multiple-scattering theory[6] for the present investigation. The theory starts from the 2-D generalized Raman-Nath equations[20,23] and represents light and

sound fields as plane-wave decompositions together with multiple scattering for the interaction. The general formalism is not only applicable to physically realistic sound fields subject to diffraction, but also to hologram type configurations. For a typical rectangular sound column with plane wave incidence as shown in figure 4.1, the general multiple scattering theory can be reduced to the following set of infinite coupled equations:

$$\frac{d\tilde{E}_n}{d\xi} = -j\frac{\alpha}{2}\exp\left\{-\frac{j}{2}Q\xi\left(\frac{\phi_{inc}}{\phi_B}+(2n-1)\right)\right\}\tilde{E}_{n-1} - j\frac{\alpha}{2}\exp\left\{-\frac{j}{2}Q\xi\left(\frac{\phi_{inc}}{\phi_B}+(2n+1)\right)\right\}\tilde{E}_{n+1} \tag{4.1-1}$$

with the boundary condition $\tilde{E}_n = \tilde{E}_{inc}\delta_{n0}$ at $z \le 0$, where δ_{n0} is the Kronecker delta, and $\tilde{E}_n$ is the complex amplitude of the nth-order plane wave of light in the direction $\phi_n = \phi_{inc} + 2n\phi_B$. ϕ_{inc} is the incident angle for the plane wave, $\tilde{E}_{inc}$, and ϕ_B is the Bragg angle defined as $\phi_B=\lambda/2\Lambda$, where λ and Λ denote the wavelengths of light and sound inside the acoustic medium, respectively. The other parameters in equation (4.1-1) are as follows: α=CkSL/2 is the peak phase delay through the medium, where C represents the strain-optic coefficient of the medium, k is the propagation constant of the light in the medium, S is the amplitude of the sound field, and L is the width of the sound column. Q is the Klein Cook parameter.[44] Lastly, ξ=L/z is the normalized distance inside the sound cell. ξ=0 signifies when a plane wave of light enters into the acousto-cell, and ξ=1 denotes when a plane wave of light exits from the cell.

Equation (4.1-1) is similar to the well-known Raman-Nath equations. In fact, it can be shown[6] that it is identical to the approximate (i.e. retaining no terms higher that ($\lambda/2\Lambda$)

Raman-Nath equations. Equation (4.1-1) identifies the plane wave contributions to $\tilde{E}_n$ from neighboring orders, with the phase terms indicating the degree of phase mismatch. It is a special case of the general multiple scattering theory valid for any sound field, not just a sound column. Note the equation (4.1-1) is valid only for small diffraction angles (i.e., paraxial approximation). For a given value of α and Q, the solution to (4.1-1) represents the contributions to the nth-order plane wave of light, $\tilde{E}_n$, due to the plane wave $\tilde{E}_{inc}$ incident at ϕ_{inc}. Note that the sign convention for ϕ_{inc} is counter-clockwise positive, that is, $\phi_{inc} = -\phi_B$ signifies upshifted Bragg diffraction.

Choosing $\phi_{inc} = -(1+\delta)\phi_B$, where δ represents the deviation of the incident plane wave away from the Bragg angle as illustrated in figure 4.2, and limiting ourselves to $\tilde{E}_0$ and $\tilde{E}_1$ we have the following set of coupled differential equations:

$$\frac{d\tilde{E}_0}{d\xi} = -j\frac{\alpha}{2}\exp\left[-j\frac{Q\xi\delta}{2}\right]\tilde{E}_1 \qquad (4.1\text{-}2a)$$

$$\frac{d\tilde{E}_1}{d\xi} = -j\frac{\alpha}{2}\exp\left[j\frac{Q\xi\delta}{2}\right]\tilde{E}_0 \qquad (4.1\text{-}2b)$$

Equations (4.1-2a) and (4.1-2b) can be solved analytically, and the solutions are given by the well-known Phariseau formula[28]:

$$\tilde{E}_0(\xi) = \tilde{E}_{inc}\exp\left\{-j\delta Q\frac{\xi}{4}\right\}\left[\cos\sqrt{(\delta\frac{Q}{4})^2+(\frac{\alpha}{2})^2}\,\xi + j\frac{\delta Q}{4}\sin\frac{\sqrt{(\delta\frac{Q}{4})^2+(\frac{\alpha}{2})^2}}{\sqrt{(\delta\frac{Q}{4})^2+(\frac{\alpha}{2})^2}}\xi\right] \tag{4.1-3a}$$

$$\tilde{E}_1(\xi) = \tilde{E}_{inc}\exp\left\{-j\delta Q\frac{\xi}{4}\right\}\left[-j\frac{\alpha}{2}\frac{\sin\sqrt{(\delta\frac{Q}{4})^2+(\frac{\alpha}{2})^2}}{\sqrt{(\delta\frac{Q}{4})^2+(\frac{\alpha}{2})^2}}\xi\right] \tag{4.1-3b}$$

Equation (4.1-3) is similar to the standard two-wave solutions found by Aggarwal[32] and adapted by Kogelnik[47] to holography. More recently, it has been re-derived using the Feynman diagram technique[6]. The equations in (4.1-3) represent plane wave solutions due to oblique incidence. By letting $\delta = 0$, they reduce to the following set of well known expressions for ideal Bragg diffraction:

$$\tilde{E}_0 = \tilde{E}_{inc} \cos\left(\frac{\alpha}{2}\xi\right) \tag{4.1-4a}$$

$$\tilde{E}_1 = \tilde{E}_{inc} \sin\left(\frac{\alpha}{2}\xi\right) \tag{4.1-4b}$$

Notice that the diffracted orders are out of phase by 90 degrees.

4.1.2 Transfer Function Formalism

Equation (4.1-3) motivated Poon and Chatterjee[42] to define the plane-wave transfer function for the Bragg cell. The transfer functions of the zeroth-order and the first-order light are defined, respectively, as follows:

$$H_0(\delta) = \frac{\tilde{E}_0(\xi)|_{\xi=1}}{\tilde{E}_{inc}} \tag{4.1-5a}$$

$$H_1(\delta) = \frac{\tilde{E}_1(\xi)|_{\xi=1}}{\tilde{E}_{inc}} \tag{4.1-5b}$$

where $\tilde{E}_0(\xi)$ and $\tilde{E}_1(\xi)$ are, in general, the results from equation (4.1-1) evaluated at the exit of the Bragg cell. For relatively low sound pressures, analytical results from equation (4.1-3) can be used to accelerate computer calculations. A transfer function approach allows the input angular spectrum, $\tilde{E}_{in}(\delta)$, to be related to the output spectrum, $\tilde{E}_{out}(\delta)$ by the following

expression,

$$\tilde{E}_{out}(\delta) = \tilde{E}_{in}(\delta)\, H(\delta) \tag{4.1-6}$$

For a specific diffracted order of light, we only need to replace $H(\delta)$ in (4.1-6) by the appropriate transfer function, for example $H_0(\delta)$ or $H_1(\delta)$, and then allow $\tilde{E}_{out}(\delta)$ to become $\tilde{E}_0(\xi)$ or $\tilde{E}_1(\xi)$ respectively. Note that this transfer function approach has recently been extended to include the propagational diffraction effect[48] and the case of large Bragg angles.[49]

4.1.3 General Formalism for Arbitrary Incident Light

This section serves to summarize the techniques used to calculate the spatial profile of any diffracted order governed by strong acousto-optic interaction. To find the input angular spectrum, we refer to the coordinate system introduced in figure 4.2, which illustrates how an arbitrary incident field propagates through a Bragg cell operating in the upshifted mode. The incident field is decomposed into multiple plane waves with different amplitudes propagating in directions defined by $-\phi' = \delta\phi_B$. We relate the angular spectrum $\tilde{E}(\phi')$, under paraxial approximation, to the spatial distribution E(r) as follows:

$$E(r) = F^{-1}\{\tilde{E}(\phi')\} = \int_{-\infty}^{\infty} \tilde{E}(\phi') \exp\left\{-j\frac{2\pi}{\lambda}\phi' r\right\} d\left(\frac{\phi'}{\lambda}\right) \tag{4.1-7a}$$

$$\tilde{E}(\phi') = F\{E(r)\} = \int_{-\infty}^{\infty} E(r)\exp\left\{-j\frac{2\pi}{\lambda}\phi' r\right\} dr \qquad (4.1\text{-}7b)$$

where $(r,-\phi'/\lambda)$ represent the transform variables.

Equations (4.1-6) and (4.1-7) may be combined to develop a general formalism for computing the profiles of any scattered light field in the spatial domain from any arbitrary input field. For the zeroth-order light,

$$E_0(r) = \int_{-\infty}^{\infty} \tilde{E}_{in}(\delta)H_0(\delta)\exp\left\{-j2\pi\frac{\delta}{2\Lambda}r\right\} d\left(\frac{\delta}{2\Lambda}\right) \qquad (4.1\text{-}8a)$$

and for the first-order light,

$$E_1(r) = \int_{-\infty}^{\infty} \tilde{E}_{in}(\delta)H_1(\delta)\exp\left\{j2\pi\frac{\delta}{2\Lambda}r\right\} d\left(\frac{\delta}{2\Lambda}\right) \qquad (4.1\text{-}8b)$$

where we have substituted $\delta\phi_B$ for ϕ' in the case of the zeroth-order light, and $-\delta\phi_{-B}$ for ϕ' in the case of the first-order light when using (4.1-7). This is consistent with the diffraction geometry defined in figure 4.2. In writing the final forms of (4.1-8), we have also used $\delta/2\Lambda$ for ϕ_B. It is important to note that we chose $H_0(\delta)$ and $H_1(\delta)$ as special cases. For any diffracted order, $H_n(\delta)$ may be found by first solving equation (4.1-1) for that particular value of n, using the definition of (4.1-5), and then substituting that solution into (4.1-8). This technique is reminiscent of the Fourier decomposition method independently developed by Magdich and Molchanov[2]. Equation (4.1-3) shows that a transfer function can modify the output profile by varying α and Q. Because this formalism involves the Fourier transform,

a FFT algorithm is used to calculate the output field distribution corresponding to a variety of arbitrary incident field profiles.

4.1.4 Beam Distortion

In this section, we investigate the behavior of $H_1(\delta)$, and based on these results we explain the beam distortion phenomena. Equation (4.1-1) provides the starting point for our general theory. Although equation (4.1-1) involves a set of infinite coupled differential equations, the effect of including more than two diffracted orders is significantly diminished as the value of Q increases. For example, we calculated the transfer functions and compared the solutions for 10 orders (i.e. $-4 \le n \le 5$) to well known ideal solutions for 2 orders defined by (4.1-3) and found that when Q exceeds 40, the solutions were nearly identical in intensity when $|\delta| \le 0.5$ and $0 \le \alpha \le 4\pi$. For Q=14.64, figures 4.3a and 4.3b show the magnitude of $H_1(\delta)$ produced by solving equation (4.1-1) with 2 orders and 10 orders, respectively. We employed a fifth order Runge-Kutta numerical method to find the solution to equation (4.1-1). The two plots have nearly the same shape along the δ-axis for small values of α. For large values of α, the plot with a larger number of diffracted orders tends to expand more along the α-axis as well as distort some features along δ. Similar behaviors are observed for Q=40 as shown in figure 4.4a and 4.4b. Results indicate that when Q is greater than 40 for the range of α investigated, solutions involving 2 and 10 diffracted orders are equivalent to the fifth decimal place. Therefore, when computing the magnitude of $H_1(\delta)$ for Q>40, we numerically solved equation (4.1-1) while limiting it to only two orders to accelerate the numerical calculations.

Figure 4.5 shows how larger values of Q modify the spectrum of the transfer function. Notice that the zeros of the transfer function move inward as the value of Q increases. The location of these zeros, particularly the first zeros, determines how severely the system distorts the profile of the input field. As an example, we inspect one of the plots for a large value of Q, say figure 4.5b for the case when Q=160. Due to the Fourier transform relationship, a narrower beam in the spatial domain leads to a wider spread in the angular spectrum domain. If this spread is large enough to cover some of the zeros in $H_1(\delta)$, distortion in the spatial domain of the Bragg scattered light profile is expected. Specifically, assume that an incident Gaussian light field $E_{in}(r)$ is given by

$$E_{in}(r) = \frac{E_{ino}}{\sigma_1\sqrt{2\pi}} \exp\left\{\frac{-r^2}{2\sigma_1^2}\right\} \tag{4.1-9}$$

where r is the radial coordinate shown in figure 4. 2. Its angular spectrum, given by (4.1-7) with $\phi' = -\delta\phi_B = \delta\lambda/2\Lambda$, becomes

$$\tilde{E}_{in}(\delta) = E_{ino} \exp\left\{\frac{-1}{2}\left(\frac{\pi\sigma_1}{\Lambda}\right)^2\delta^2\right\} \tag{4.1-10}$$

where σ_1 represents the 1/e point of the incident Gaussian field. For a Gaussian laser beam whose width is five times greater than the sound signals wavelength ($\sigma_1/\Lambda=5$), the 1/e point of the angular spectrum is given by $\delta_{1/e} = 210.09$. When operating with Bragg cells, one would like to work with maximum diffraction into the first order. This point of operation occurs when the value of α is an odd multiple of π for cells with a large Q value. Looking

at figure 4.6a, it is shown that the angular spread of the incident beam spans beyond the first zero of $|H_1(\delta)|$ for $\alpha=\pi$. Physically, it means that some contribution from the plane waves of the beam are diminished while others are not scattered at all. Therefore, reconstruction of the beam at the exit of the Bragg cell may show distortion. To avoid this distortion, one may work with $\alpha = 3\pi$ instead of $\alpha = \pi$ because the transfer function in figure 4.6b indicates that the first zero of the transfer function has moved beyond $\delta_{1/e}$ at $\alpha=3\pi$. Before verifying this point, it is instructive to develop an explicit expression that represents the diffracted field. This is done by substituting (4.1-10) into (4.1-8b) and using (4.1-5b) to obtain the following expression for $E_1(r')$:

$$E_1(r) = \int_{-\infty}^{\infty} \tilde{E}_{inc} e^{(\frac{\pi\sigma_1}{2\lambda})^2 \delta^2} \left\{ (-j\frac{\alpha}{2}) e^{j\frac{\delta Q}{4}} \operatorname{sinc} \sqrt{(\delta Q/4)^2+(\alpha/2)^2} \right\} e^{j\frac{\pi\delta}{\Lambda} r} d\left(\frac{\delta}{2\Lambda}\right) \quad (4.1\text{-}11)$$

where $(-r',\delta/2\Lambda)$ are identified as the Fourier transform variables. Figure 4.6 plots the normalized intensity profile of the Bragg scattered beam, $I_1(r') = |E_1(r')|^2$. The input Gaussian beam has also been plotted at the center of the two output beams as a reference. Notice that the output profile is distorted more at $\alpha=\pi$ than it is at $\alpha=3\pi$. That is, the profile still has somewhat of a Gaussian shape at $\alpha=3\pi$, in fact, it has a low-pass version of the input Gaussian beam.

The discussion above illustrates beam distortion in the Bragg scattered beam when either a thick hologram or an acousto-optic Bragg cell is illuminated by a narrow laser beam. By inspecting the transfer function of the Bragg cell for a specific Q value and input beam

size, one can predict distortion phenomena intuitively without using complicated mathematics.

4.2 Physical Interpretations and Insights

Using the multiple plane wave scattering formalism, we developed a general technique to predict the spatial profile of a diffracted laser beam. Similar to methods outlined in chapter 2.0, this theory applies to two-dimensional geometries only. One limitation of this and all other preceding theories lie in its neglect of transducer height. By not incorporating this dimension into the overall theory, experimentally observed effects may not be accurately predicted. For example, McNeill and Poon[50] used the approach in section 4.1.3 to predict the profile of a Gaussian beam after interacting with a rectangular sound column. While the theory correctly predicted the profile along the x-axis, no further insight is given about the profile along the y-axis.

The major shortcoming of the 2-D approach lies in its assumption that a finite width sound field with perfectly straight wave fronts exists. Similarly, a rectangular transducer possessing a 'y' dimension that is significantly shorter than its 'z' dimension will produce a profile that spreads within the cell according to Fresnel diffraction. Thus, the sound wave would be even less of a plane wave along its y-dimension. Lastly, ordinary diffraction of the sound wave as it propagates will produce an interaction region that is different from one made up by a single plane wave.

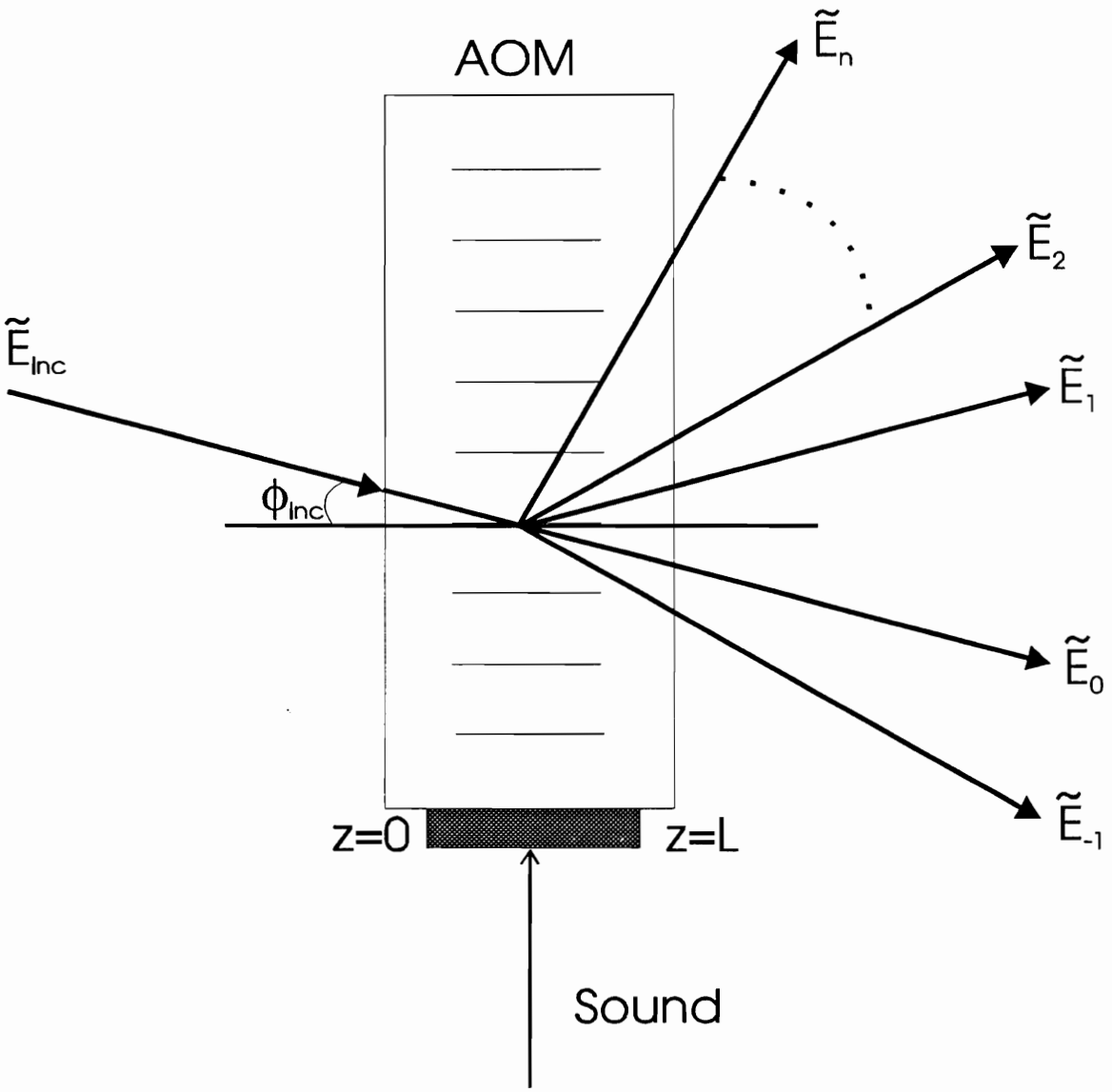

Fig. 4.1: Sound-Light Interaction using rectangular sound column model.

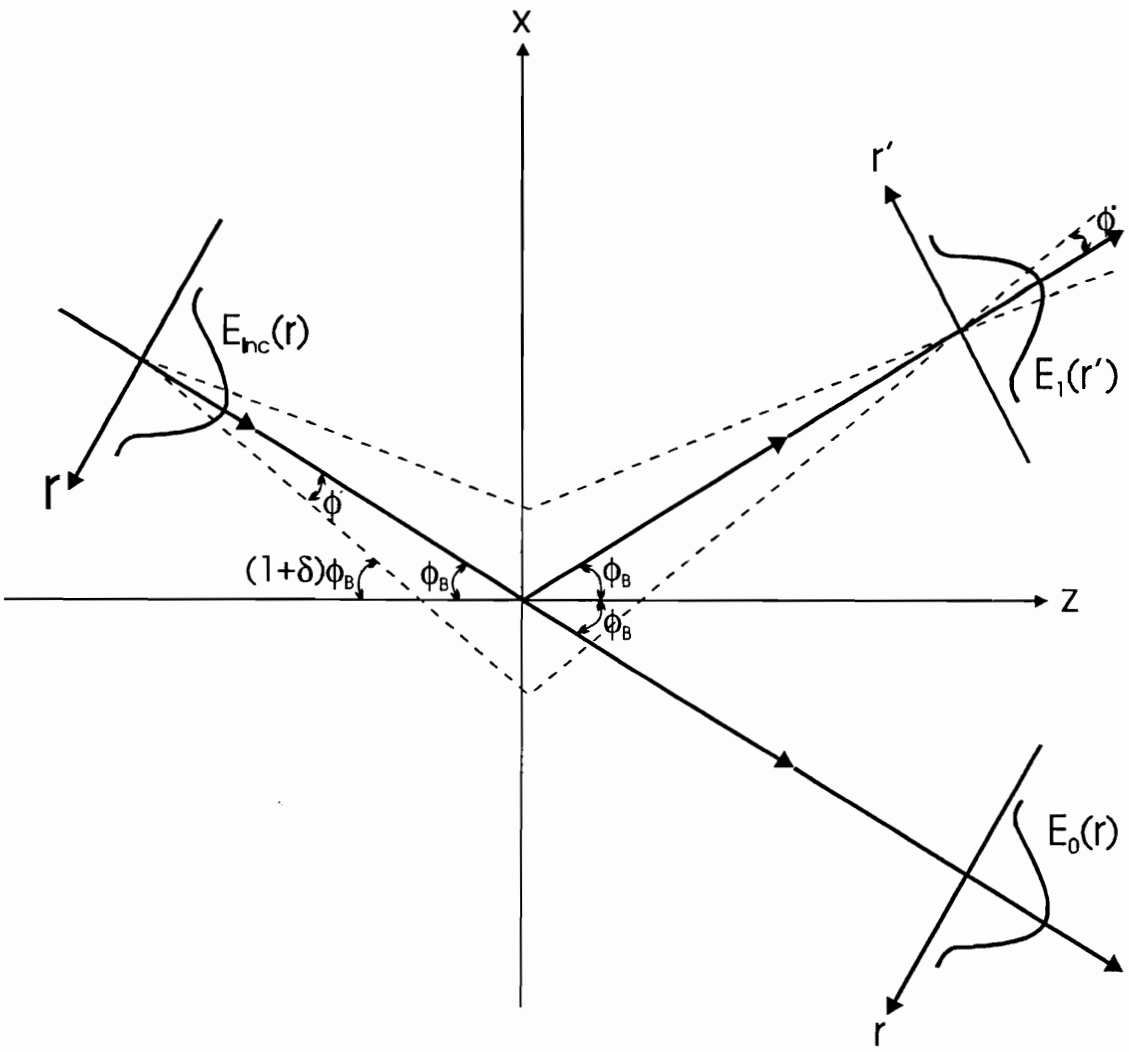

Fig. 4.2: Diffraction geometry for upshifted Bragg operation.

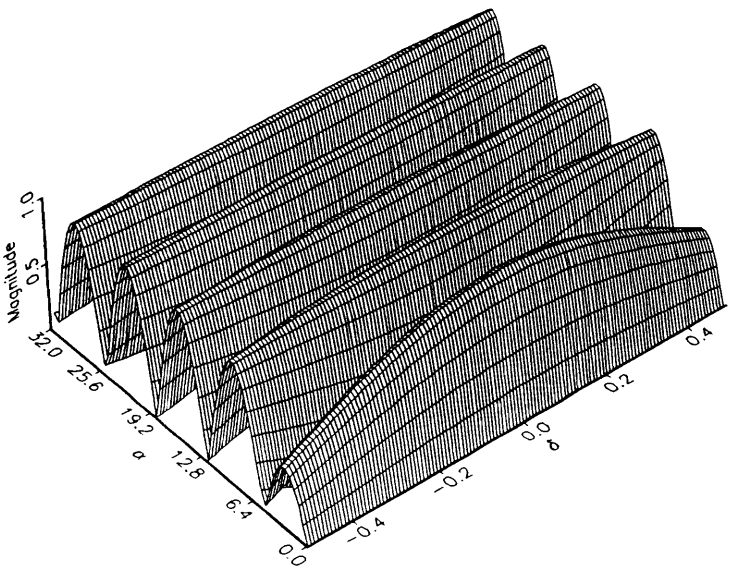

(a)

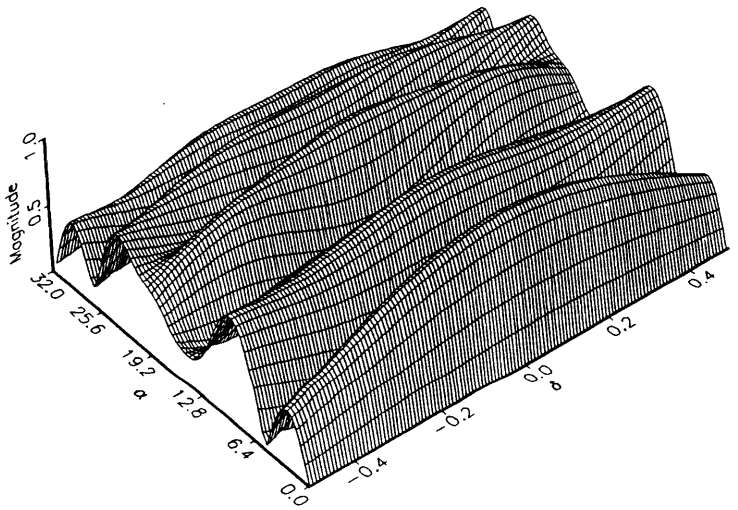

(b)

Fig. 4.3: Numerical plots of $|H_i(\delta)|$ as a function of the peak phase delay, α, for Q=14.64. (a) Ideal solution involving two diffracted orders, (b) solution involving ten diffracted orders.

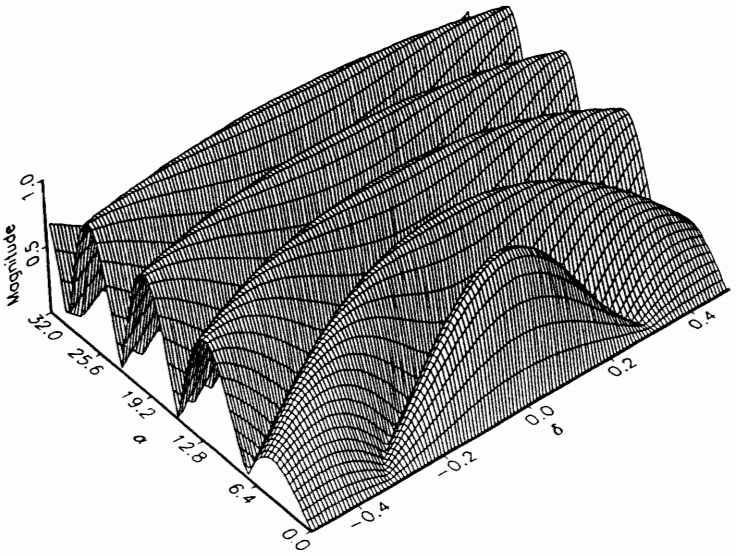

(a)

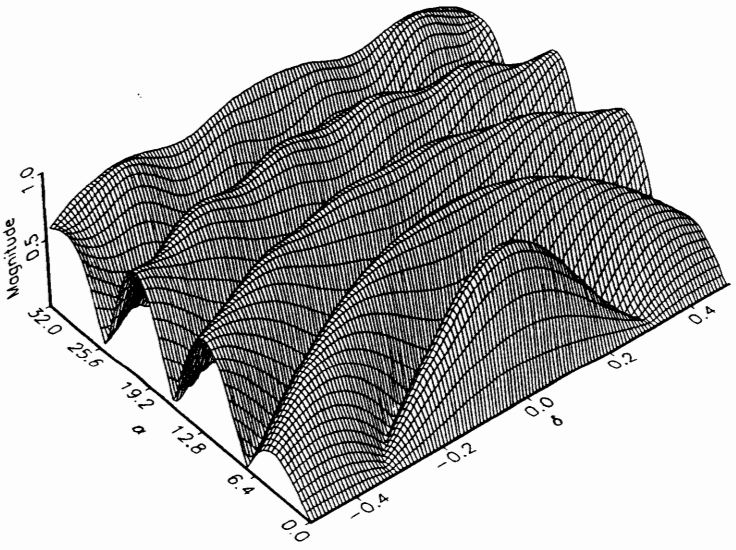

(b)

Fig. 4.4: Numerical plots of $|H_i(\delta)|$ as a function of the peak phase delay, α, for Q=40. (a) Ideal solution involving two diffracted orders, (b) solution involving ten diffracted orders.

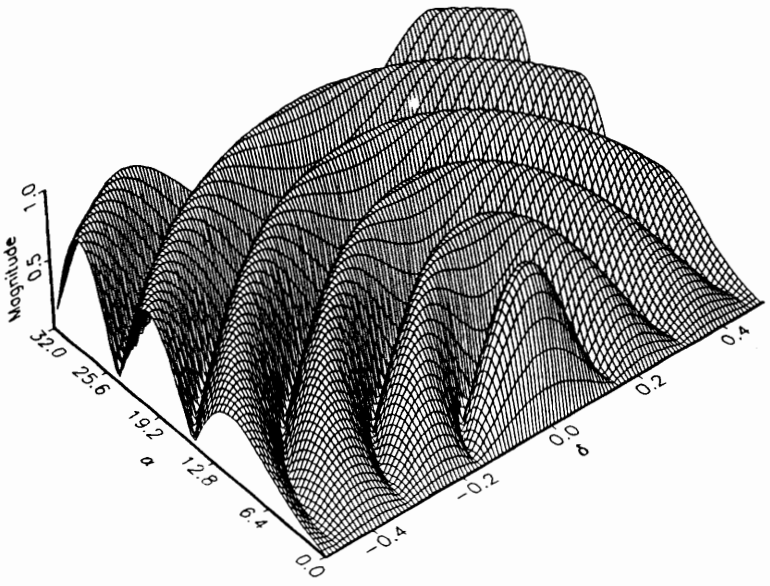

(a)

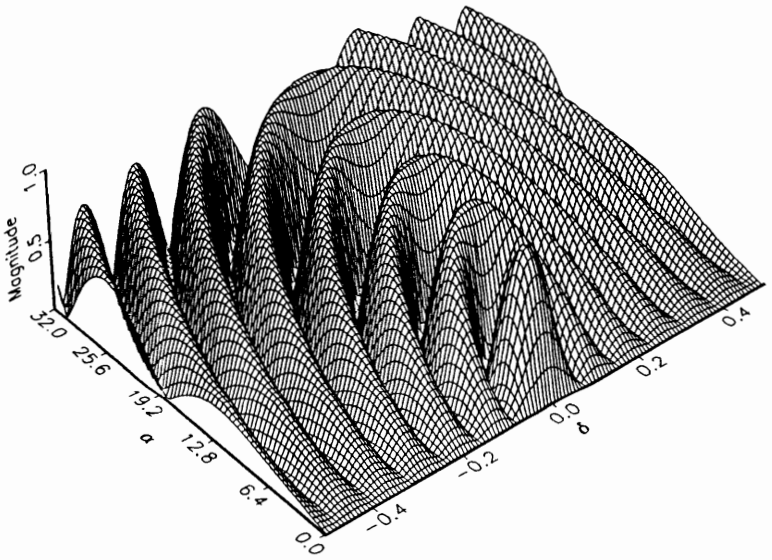

(b)

Fig. 4.5: Numerical plots of $|H_1(\delta)|$ as a function of a, (a) Q=80, (b) Q=160.

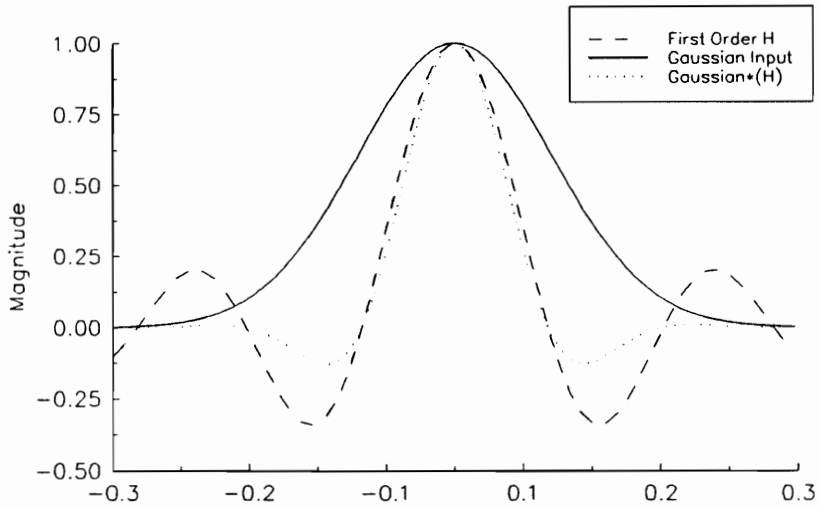

(a)

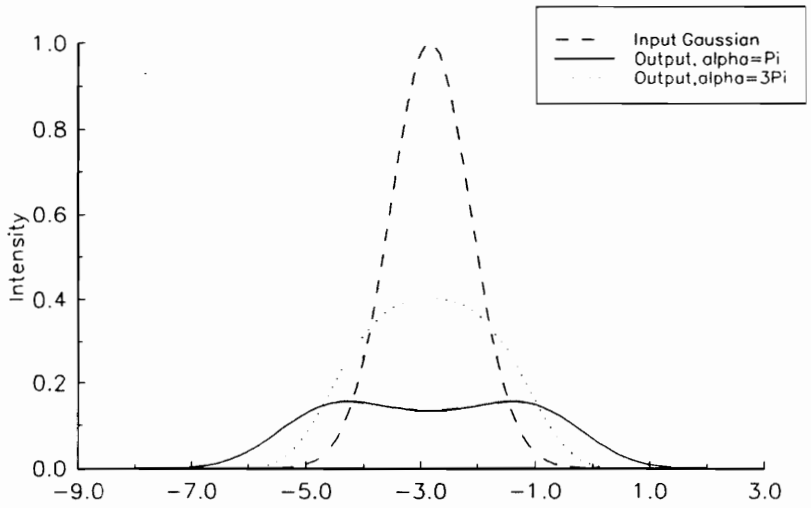

(b)

Fig 4.6: (a) Curves showing the 1/e point of the Gaussian spectrum coincide with the first zero of $H_1(\delta)$. (b) Beam distortion occurs at $\alpha=\pi$ and disappears at $\alpha=3\pi$.

5. Strong Acousto-Optic Interaction in Two Transverse Dimensions

5.1 Basic Overview

This chapter develops more robust acousto-optic interaction theories than the transfer function formalism presented in chapter 4. The primary advantages incorporated into the "split-step" type algorithms presented in sections 5.2 and/or 5.3 include: (1) three-dimensional strong acousto-optic Bragg diffraction, (2) arbitrary light and sound field interaction, (3) controlled placement of an incident light beam within the Bragg cell, and (4) greater insight into the physical process. Two different split-step algorithms provide numerical solutions to separately derived acousto-optic interaction expressions. Each method uses Fresnel diffraction to propagate an incident Gaussian light beam through an acoustically perturbed Bragg cell.

The first method, called the Fourier-optics approach, builds upon the work of Van Cittert[26] and Brillouin[19] by expanding their original prediction of acousto-optic interaction within thick cells (as it pertains to the rescattering of already diffracted light) to three-dimensions. Basically, the Fourier-optics approach divides the Bragg cell into many slices perpendicular to the optical axis (i.e. the primary direction of light propagation). A thin phase grating approximates the acoustic perturbations present in each slice. The method multiplies the incident optical beam by the thin phase grating and propagates the resulting field the width of one slice using Fresnel diffraction. The multiplication followed by propagation process

continues until the incident optical beam traverses the entire Bragg cell.

The wave-equation approach, presented in section 5.3, represents the second method. The fundamental theory begins with Maxwell's equations and ends with a set of coupled differential equations for strong acousto-optic interaction. The wave-equation approach is a numerical method that solves this coupled equation and consequently the three-dimensional acousto-optic interaction problem. The basic principle behind the process is that diffraction (or propagation) takes place in the spectrum domain and interaction takes place in the spatial domain. This allows only simple multiplications in their prospective domains. The wave-equation approach also allows the location (along the nominal direction of sound) of the incident light beam within the Bragg cell. The beam location does not have an effect on the diffracted beam if the sound field is uniform. However, when the sound field is not uniform, the beam location may influence the acousto-optic interaction process. Lastly, a Gaussian sound beam replaces the ideal rectangular sound column to illustrate how different sound field profiles affect the process. Special attention is given to how changes in the transverse dimensions of the sound beam (beam waist) affect certain characteristics of the diffracted beam.

5.2 Fourier-Optics Approach

5.2.1 Description of the Algorithm

Figure 5.1 depicts the geometric configuration and axis conventions for acousto-optic Bragg diffraction. Incident light propagates predominantly in the positive z-direction and

sound in the positive x-direction. The y-direction is directed out of the page and is perpendicular to direction of light and sound. Physically, the y-direction allows us to include cell height into the acousto-optic interaction process. All previous two-dimensional theories assume that light and sound interact at the y equal zero plane (i.e. The figure shown is in the x-z plane located at y=0.). A specific plane wave in the angular spectrum is denoted by the angles ϕ and θ (counterclockwise positive) for light and sound, respectively. Operation in the Bragg regime ensures that the light beam is incident at the Bragg angle, $\phi_B = \lambda/2\Lambda$. Analytically, this represents an axis rotation through ϕ_B and causes the incident Gaussian light beam on the x-y plane (perpendicular to the x-z plane shown in figure 5.1) to be

$$\psi(x,y,z=0) = \exp\left[-\frac{[x\cos(\phi_B)]^2 + y^2}{w_0^2}\right]\exp[jK\,x\sin(\phi_B)], \qquad (5.2\text{-}1)$$

where w_0 is the beam waist, $K=2\pi/\Lambda$ is the propagation constant for sound, and $z=0$ signifies that the light beam is adjacent to the entrance side of the Bragg cell. The algorithm propagates this two-dimensional beam (in the z direction) through a rectangular sound column whose distance equals the width of the sound cell.

The Fourier-optics method begins by dividing the acousto-optic cell into thin slices of width, Δz. Each slice acts as a thin phase grating during interaction and a homogeneous medium during propagation. Within the algorithm, the incident light field propagates through each slice twice, once in the presence of sound and once in the absence of sound. This statement will be clearer after inspecting figure 5.2a. Figure 5.2b illustrates the physical

interpretation of the algorithm as a rescattering of already diffracted light. The slices have an almost infinitesimal thickness, Δz, and hence acts as a weak phase grating that generates two additional orders for each incident one.[51] Note, the algorithm assumes that the slices coincide with each other and the space between the slices are for illustration purposes only. During the first step the incident light field is multiplied by an inhomogeneous, non-diffracting sound field (i.e., thin phase grating). The exact mathematical form of the inhomogeneity is given later in this section. Maintaining the formalism used in reference[42], a forward Fourier transform is used to obtain the angular plane-wave spectrum of the incident light field. During the next step the slice is considered to be homogeneous and diffracting, with diffraction implemented using the spatial transfer function for propagation,

$$H(k_x, k_y; \Delta z) = \exp\left[\frac{j(k_x^2 + k_y^2)}{2k_0}\Delta z\right]. \qquad (5.2\text{-}2)$$

The angular plane-wave spectrum is multiplied by the spatial transfer function in equation (5.2-2) to simulate diffraction through a homogeneous medium of width Δz. An inverse Fourier transform of this result is performed to obtain the homogeneously propagated field, and the result represents the total field after executing one loop of the algorithm. The resulting field is then multiplied by the thin phase grating as outlined in the first step and propagated by the spatial transfer function. This process is repeated until the incident beam traverses the entire width of the acousto-optic cell. The flow chart in figure 5.3 illustrates the complete Fourier-optics algorithm.

Using the operator formalism developed by Korpel et. al.[52] the split-step algorithm may be compactly written by the following expression:

$$\psi(x,y,z+\Delta z) = F^{-1} H F M \psi(x,y,z) \qquad \Delta z \to 0 , \tag{5.2-3}$$

where the order of evaluation is from right to left. $\psi(x,y,z)$ represents the incident light beam, $M(x,y,z)$ is the phase grating multiplier, $H(k_x,k_y)$ is the spatial transfer function, and F and F^{-1} pertain to the forward and inverse Fourier transforms, respectively. Reviewing figures 5.2b together with equation (5.2-3) further reinforces the fact that Bragg diffraction is simply the rescattering of already diffracted light.

Modelling the physical process begins with an expression for the small perturbations in the index of refraction. $\delta n(x,y,z,t)$ denotes these regions of rarefaction and compression caused by the acousto-optic effect. The mathematical expression for $\delta n(x,y,z,t)$ is

$$\delta n(x,y,z,t) = C' s(x,y,z,t) , \tag{5.2-4}$$

where $C' = n_0 C/2$ is a real material constant. n_0 is the refractive index of the medium in the absence of sound, and $C = -pn_0^2$, where p denotes the strain-optic (or photoelastic) coefficient. Normally $\delta n \ll 1$, therefore it is assumed that equation (5.2-4) can be expanded to

$$\delta n(x,y,z,t) = \frac{C'}{2} S_e(x,y,z) \exp[-jKx] \exp[j\Omega t] + \frac{C'}{2} S_e^*(x,y,z) \exp[jKx] \exp[-j\Omega t] \tag{5.2-5}$$

where Ω is the sound frequency, K is the propagation constant for sound, $s_e(x,y,z)$ is the complex envelope of the sound wave, and $s_e^*(x,y,z)$ is its complex conjugate. To this point, the fact that the medium has a time varying inhomogeneous refractive index has not been addressed. However, because the acoustic frequency is much smaller than the optical frequency by several orders of magnitude, a static refractive index model can be applied. If the instantaneous change of δn is taken at t=0, equation (5.2-5) reduces to

$$\delta n(x,y,z,t) = \frac{C'}{2} S_e(x,y,z) \exp[-jKx] + \frac{C'}{2} S_e^*(x,y,z) \exp[jKx]. \qquad (5.2\text{-}6)$$

Notice that the sound field is an arbitrary three-dimensional function that propagates in the x-direction.

Returning to the test condition presented in chapter 4, $\delta n(x,y,z)$ can be arranged to allow for direct comparison with the transfer function formalism. The process begins by substituting for C' in equation (5.2-6) and letting $S_e(x,y,z)=S(x,z)=S^*(x,z)=|S|$, where |S| is a real constant. These changes lead to the following simplification of the refractive index variation,

$$\delta n(x,y,z) = \frac{n_0}{2} C |S| \cos(Kx). \qquad (5.2\text{-}7)$$

Reexamining the split step method defined by equation (5.2-3), allows the first operation in the method, which represents acousto-optic interaction, to be written as

$$M\psi(x,z) = \psi(x,z)\exp[-jk_v \delta n(x,z)\Delta z], \tag{5.2-8}$$

where k_v is the free space propagation constant of the incident light beam. Substituting equation (5.2-7) into (5.2-8) and performing some additional algebra enables the final form of the interaction process to become

$$M\psi(x,z) = \psi(x,z)\exp[-j\alpha \Delta \xi \cos(Kx)]. \tag{5.2-9}$$

where $\alpha = n_0 k_v C|S|L/2$ and $\Delta\xi = \Delta z/L$. Equation (5.2-9) together with (5.2-2) and (5.2-3) provide a complete method for the interaction between a Gaussian light beam and a rectangular sound column. It is clear that the two-dimensional test case can be expanded to include three dimensions by simply reintroducing the y-coordinate into (5.2-9). This introduction is simpler when considering the optical field instead of the sound field. Namely, the light field serves as a envelope in equation (5.2-9) and therefore introducing y into $\psi(x,y,z)$ states that you have an arbitrary light field incident on an infinite plane wave. In fact this is what we will present as our 3-D solution in section 5.2.4. To introduce the y dimension into the general theory we begin with equation (5.2-6) because this is where the 3-D sound field envelope last exists in our theoretical development. In general, $\delta n(x,y,z)$ becomes complicated for theoretical solutions, however for numerical solutions one need only to define $S_e(x,y,z)$ and $S^*_e(x,y,z)$ to define $\delta n(x,y,z)$. This portion of the algorithm makes it possible to model acousto-optic interaction between arbitrary 3-D light and sound fields. We chose $S_e(x,y,z)$ to be a real constant in the simulation results that follow (i.e. equation

(5.2-7) applies to the sound field purtabations for 3-D interaction).

5.2.2 Simulation Results for Gaussian Light Profiles

At z = 0, we assume the light field to be incident on the left edge of the acousto-optic cell as shown in figure 3.2. The Fourier-optics algorithm presented in section 5.2.1 propagates this beam through the cell (in the z-direction) until it exits at the right edge. The resulting diffracted field is propagated by the free space transfer function an additional distance of 84cm. This additional step allows the simulation results to agree with those taken from experiments (experimental measurements were conveniently taken 84 cm from the exit of the acousto-optic modulator). The spatial and spectral properties of the diffracted beams are written to a text file where they are plotted using a commercial plotting package.

The Fast Fourier Transform (FFT) algorithm responsible for a bulk of the computations was selected from reference[53]. The discrete Fourier transform was written in the following form:

$$F(k) = \sum f(n) \exp(-j2\pi kn/N) \qquad (5.2\text{-}10)$$

$$f(n) = \sum F(k) \exp(j2\pi kn/N) \qquad (5.2\text{-}11)$$

where equation (5.2-10) is the forward transform and (5.2-11) is the inverse transform. The appropriate size of the array was determined by trial and error. The confining constraints were the overall computation time, and the relative density of the sample points and discrete frequencies in the spatial and spectral domains, respectively. A 512x512 FFT generates plots

of sufficient detail in each domain.

To aide in the implementation of the algorithm, all distance related parameters are normalized with respect to the wavelength of light inside the acousto-optic cell. The wavelength of this light source equals 632.8nm, which corresponds to the Helium-Neon laser in the experimental setup. Because the refractive index of dense glass equals 1.5, the wavelength of light within the Bragg cell becomes 422nm. The spot size of the input laser beam was measured at 0.84mm, therefore, the input laser beam waist corresponds to a normalized value of 1000 inside the algorithm. All other scaling factors are handled by considering the Gaussian characteristics of the input laser beam.

5.2.3 Comparison with Analytical Results

Figures 5.4 through 5.6 show that the Fourier-optics based numerical simulations agree with plots produced by directly solving equations (4.1-8a) and (4.1-8b). While the solutions for the wave-equation approach also appear on these plots, discussion of the specific details are deferred until section 5.3.3. These plots represent spectrum plots for the light field at the exit of the acousto-optic cell (i.e. $z = L$, the width of the cell). The Gaussian spectrum shown symmetric about the point, $\phi/\phi_B = 1.0$, denotes the amount of light diffracted into the first diffracted order. Likewise, the two mounds symmetric about $\phi/\phi_B = -1.0$, denote the zero diffracted order. These curves show that at $\pm \phi_B$ all of the incident light is deflected out of the zero order and into the first order. This agrees with previous theories pertaining to a plane wave of light incident on a rectangular sound column. An important observation to point out is that for incident angles slightly off the Bragg angle, it is still possible to deflect

light into the first order. In all three figures, α is set equal to π, the normalized value of the sound field amplitude and the peak phase delay of the light through the acoustic medium (refer to equations 4.14 a and b in chapter 4). Because the analytical solutions assume ideal Bragg diffraction, only the zeroth and first diffracted orders need to be considered. The comparison between numerical and analytical results is justified if the power in the higher orders (i.e. minus-1, plus-2, etc.) remain negligible. Practically, this means that $Q \gg 1$. Section 4.1 shows that there is no measurable difference between numerical and analytical results when $Q \geq 40$. However, because the value of Q calculated for the experimental setup equals 14.64, the power present in the higher orders is not negligible. Namely, some of the differences between the numerical and analytical results in the figures can be attributed to small amounts of power in the higher orders. The effect of changing the optical beam waist while holding α and Q constant is also evident in figures 5.4 -5.6. The primary purpose for these graphs is to show that the Fourier-Optics method correctly tracks known results. Figure 5.7 plots results that include four diffracted orders. Notice that the amplitude in the minus-1 and plus-2 orders compare well with that of the zeroth order. Since we measured our experimental results in the spatial domain instead of the spectrum domain, only simulation results are shown in the plot. Reference[15] provides experimental measurements that verify the results due to changing the waist of the incident Gaussian beam and to considering higher diffracted orders. Since our simulation results agree well with the methods used in the cited reference, is it our assumption that they will also agree with experimental data taken in the spectrum domain.

5.2.4 3-D Simulation Results

Up to this point, numerical results have applied to two-dimensional (x and z) acousto-optic systems. This section provides results that show acousto-optic interaction in three-dimensions. Section 3.1.2 presents the physical layout for three-dimensions, where x and y denote the transverse coordinates, and z denotes the primary propagation direction for incident light. Sound is assumed to propagate in the x direction with transverse coordinates given by y and z. Although the Fourier-optics theory provides for arbitrary light and sound fields, a rectangular sound column serves as the sound source. This choice reduces the computation time and additional memory requirements to run the algorithm. To replace the sound column with an arbitrary sound field, calculation of the sound field throughout the interaction region should occur before the light field is propagated. This will produce a three-dimensional array of complex values at all points of interest in the x, y and z directions. If the sound field is Gaussian, it may be analytically calculated as it propagates in the x direction.

Extending the numerical algorithm to include three dimensions follows directly from two-dimensional results presented in section 5.2.1. Because the Fourier-optics method assumes plane wave fronts for the sound field, it is expected that changes along y will be minimal. Physically this means that components of the incident light beam reflects off acoustic plane waves possessing the same sound strength along the y axis. Essentially this is equivalent to saying that most of the acousto-optic interaction occurs in the x-z plane. Refer to figure 5.1 and assume that it lies in the x-z plane (i.e. $y = 0$ plane). Next assume that the x-y plane passes through this figure such that exactly equal amounts of the plane appear

above and below the paper. Now it should be clear that one may view the three-dimensional solution as multiple two-dimensional solutions. With no loss of generality, the same idea may be applied to three-dimensional plots in the spectrum domain. Figure 5.8a shows spectrum plots of the zero and first diffracted orders. Notice that while the expected split occurs in the zero order, Gaussian characteristics remain along the K_y direction. Using our discussion of multiple two-dimensional planes to describe the figure, we see that at $K_y = 0$ the diffraction pattern has its largest values. If we look at the next curve located at $K_y \approx 0.1$, we notice that it has the same shape as before but at a slightly lower amplitude since the incident light field is Gaussian in the y-direction. Other plots of the spectrum in the K_x-K_z planes at K_y = constant show that the shape of the zero diffracted order equals that at the $K_y = 0$ plane, except it is reduced by the amplitude of the Gaussian beam. Figure 5.8b shows that the first order beam maintains its Gaussian form in both dimensions. Figures 5.9a -5.9d show three-dimensional spectra for beam widths of 211um and 105um, respectively. Notice that the shapes of these curves follow the general trend of the two-dimensional graphs in figures 5.4 - 5.6, the smaller the beam waist, the more the diffracted order spreads. Looking closely at the spectrums in figure 5.9, it is clear that as the beam waist shrinks the spectrum spreads in both the K_x and K_y directions. For example, comparing figure 5.8a to figure 5.9c shows that the spectrum for the smaller beam waist is much larger in both the K_x and K_y directions. For completeness, figures 5.10 and 5.11 show spatial distributions corresponding to the spectrum plots in figure 5.8 and 5.9. As will be shown in chapter 6, the spatial plots shown in figure 5.10 compare well with the experimental measurements.

Because we institute a plane wave model for the sound field profile, no significant changes along y are expected or predicted by the Fourier-Optics algorithms. This may be explained from a two-dimensional perspective, and follows from the discussion above. Namely, acousto-optic interaction in the y = 0 and the y = constant planes is more or less identical, with the exception that the diffracted orders may be "modulated" by the shape of the input light field in the y-direction. This limit can be overcome by changing the input sound beam profile. In any event, this method is not only applicable to rectangular sound columns, but it is also applicable to thick phase gratings. Section 5.3 presents the wave-equation approach where a Gaussian sound field interacts with the incident light beam. Therefore simulation results that investigate changes along y are incorporated into that section with no loss of generality.

5.3 Wave Equation Approach

5.3.1 Fundamental Theory

The work outlined in this section closely follows the original work of Korpel.[44] It is included here to provide greater insight into acousto-optics and to justify the scalar wave equation for strong acousto-optic interaction. The theory begins with Maxwell's equations and applies them to an acoustically perturbed medium. The chief aim is to discuss under what conditions can polarization of the incident and scattered light fields be neglected. Regarding sound, our theory assumes that the change in permittivity is a scalar function and causes no cross coupling of polarization states.

First, consider an optical field $\mathbf{E}_0(\mathbf{r},t)$ incident on a homogeneous isotropic medium characterized by permeability μ and permittivity ε. Next, assume this field satisfies the source free form of Maxwell's equations, i.e.,

$$\nabla \times \mathbf{H}_0(\mathbf{r},t) = \varepsilon \, \partial \mathbf{E}_0(\mathbf{r},t)/\partial t \,, \tag{5.3-1}$$

$$\nabla \times \mathbf{E}_0(\mathbf{r},t) = -\mu \partial \mathbf{H}_0(\mathbf{r},t)/\partial t \,, \tag{5.3-2}$$

$$\nabla \cdot \mathbf{E}_0(\mathbf{r},t) = 0 \,, \tag{5.3-3}$$

$$\nabla \cdot \mathbf{H}_0(\mathbf{r},t) = 0 \,. \tag{5.3-4}$$

The time varying permittivity is written as

$$\varepsilon(\mathbf{r},t) = \varepsilon + \varepsilon'(\mathbf{r},t) \,, \tag{5.3-5}$$

where $\varepsilon'(\mathbf{r},t)$ represents the acoustically induced perturbations in the medium.

With the sound signal present within the medium, the total field $\mathbf{E}(\mathbf{r},t)$ must satisfy the following:

$$\nabla \times \mathbf{H}(\mathbf{r},t) = (\partial/\partial t)[\varepsilon(\mathbf{r},t)\mathbf{E}(\mathbf{r},t)], \tag{5.3-6}$$

$$\nabla \times \mathbf{E}_0(\mathbf{r},t) = -\mu(\partial/\partial t)\mathbf{H}(\mathbf{r},t), \tag{5.3-7}$$

$$\nabla \cdot [\varepsilon(\mathbf{r},t)\mathbf{E}(\mathbf{r},t)] = 0, \tag{5.3-8}$$

$$\nabla \cdot \mathbf{H}(\mathbf{r},t) = 0. \tag{5.3-9}$$

$\mathbf{E}(\mathbf{r},t)$ is the sum of the incident and scattered light field,

$$\mathbf{E}(\mathbf{r},t) = \mathbf{E}_0 + \mathbf{E}'(\mathbf{r},t). \tag{5.3.10}$$

Therefore, the scattered field must also satisfy the following equations:

$$\nabla \times \mathbf{H}'(\mathbf{r},t) = \partial \mathbf{D}'(\mathbf{r},t)/\partial t, \tag{5.3-11}$$

$$\nabla \times \mathbf{E}'(\mathbf{r},t) = -\mu \partial \mathbf{H}'(\mathbf{r},t)/\partial t, \tag{5.3-12}$$

$$\nabla \cdot \mathbf{D}'(\mathbf{r},t) = 0, \tag{5.3-13}$$

$$\nabla \cdot \mathbf{H}'(\mathbf{r},t) = 0. \tag{5.3-14}$$

where

$$\mathbf{D}'(\mathbf{r},t) = \varepsilon_0 \mathbf{E}'(\mathbf{r},t) + \mathbf{P}'(\mathbf{r},t) \tag{5.3-15}$$

and

$$\mathbf{P}'(\mathbf{r},t) = \varepsilon'(\mathbf{r},t)[\mathbf{E}_0(\mathbf{r},t) + \mathbf{E}'(\mathbf{r},t)], \tag{5.3-16}$$

Equations (5.3-11) - (5.3-16) show that the product of the perturbation $\varepsilon'(\mathbf{r},t)$ and the total field $\mathbf{E}(\mathbf{r},t)$ define an induced polarization $\mathbf{P}(\mathbf{r},t)$. Furthermore, the scattered field itself is

derived from this polarization field.

To aide in the theory that follows, it is useful to express $\mathbf{E}'(\mathbf{r},t)$ and $\mathbf{H}'(\mathbf{r},t)$ in terms of the Hertz vector $\mathbf{\Pi}'(\mathbf{r},t)$. This leads to the following expressions for the scattered fields:

$$\mathbf{H}'(\mathbf{r},t) = \varepsilon \nabla \times \partial \mathbf{\Pi}'(\mathbf{r},t)/\partial t \tag{5.3-17}$$

$$\mathbf{E}'(\mathbf{r},t) = \nabla \nabla \cdot \mathbf{\Pi}'(\mathbf{r},t) - \mu \varepsilon \partial^2 \mathbf{\Pi}'(\mathbf{r},t)/\partial t^2 . \tag{5.3-18}$$

Equations (5.3-6) through (5.3-9) are satisfied if $\mathbf{\Pi}'(\mathbf{r},t)$ satisfies the equation

$$\nabla^2 \mathbf{\Pi}'(\mathbf{r},t) - \mu \varepsilon \frac{\partial^2 \mathbf{\Pi}'(\mathbf{r},t)}{\partial t^2} + \frac{\mathbf{P}'(\mathbf{r},t)}{\varepsilon} = 0 . \tag{5.3-19}$$

The solution to (5.3-19) can be expressed in the form of the retarded potential,

$$\mathbf{\Pi}'(\mathbf{r},t) = \frac{1}{4\pi\varepsilon} \int \frac{\mathbf{P}'(\mathbf{r}',t - R/\upsilon)}{R} dv' , \tag{5.3-20}$$

where the integration is over the interaction volume, $R = |\mathbf{r} - \mathbf{r}'|$, $\upsilon = (\mu\varepsilon)^{(-1/2)}$ is the velocity of light in the medium, and dv' is a differential volume element of space. It should be noted that (5.3-20) is an integro-differential equation since $\mathbf{P}'(\mathbf{r},t)$ itself contains the unknown $\mathbf{E}'(\mathbf{r},t)$. This becomes clear by substituting (5.3-20) and (5.3-16) into (5.3-18):

$$\mathbf{E}'(\mathbf{r},t) = \frac{1}{4\pi\varepsilon} \int \frac{1}{R} \left(- \mu\varepsilon \frac{\partial^2}{\partial t^2} + \nabla\nabla\cdot \right) \varepsilon'(\mathbf{r},t - R/\upsilon)[\mathbf{E}_0(\mathbf{r}',t - r/\upsilon) + \mathbf{E}'(\mathbf{r}',t - r/\upsilon)]dv' . \tag{5.3-21}$$

Equation (5.3-21) signifies where Bhatia and Nobel[27] began their preliminary investigations

concerning acousto-optic interaction.

By adding the Hertz vector of the incident field, $\mathbf{\Pi}_0(\mathbf{r},t)$, to equation (5.3-19) it is possible to derive a general expression for the interaction process. Beginning with the source field:

$$\nabla^2 \mathbf{\Pi}_0(\mathbf{r},t) - \mu\varepsilon \frac{\partial^2 \mathbf{\Pi}_0(\mathbf{r},t)}{\partial t^2} = 0, \tag{5.3-22}$$

and using the Hertz vector $\mathbf{\Pi}(\mathbf{r},t)$ of the total field,

$$\mathbf{\Pi}(\mathbf{r},t) = \mathbf{\Pi}_0(\mathbf{r},t) + \mathbf{\Pi}'(\mathbf{r},t), \tag{5.3.23}$$

it is apparent that

$$\nabla^2 \mathbf{\Pi}(\mathbf{r},t) - \mu\varepsilon \frac{\partial^2 \mathbf{\Pi}(\mathbf{r},t)}{\partial t^2} + \frac{\mathbf{P}'(\mathbf{r},t)}{\varepsilon} = 0. \tag{5.3-24}$$

The relation between $\mathbf{E}(\mathbf{r},t)$ and $\mathbf{\Pi}(\mathbf{r},t)$ is similar to (5.3-18):

$$\mathbf{E}(\mathbf{r},t) = \nabla\nabla\cdot\mathbf{\Pi}(\mathbf{r},t) - \mu\varepsilon \frac{\partial^2 \mathbf{\Pi}(\mathbf{r},t)}{\partial t^2} \tag{5.3-25}$$

Substituting (5.3-16) into (5.3-24) and using (5.3-25) yields

$$\nabla^2\mathbf{\Pi}(\mathbf{r},t) - \mu\varepsilon(\mathbf{r},t)\frac{\partial^2 \mathbf{\Pi}}{\partial t^2} = -\frac{\varepsilon'(\mathbf{r},t)}{\varepsilon}\nabla\nabla\cdot\mathbf{\Pi}(\mathbf{r},t). \tag{5.3-26}$$

The $(\nabla\nabla\cdot)$ term in (5.3-26) represents the polarization effects induced by the sound wave onto the incident light beam. This term is totally neglected for the two-dimensional

interaction geometry. For a three-dimensional configuration, this term has minimal effects on the overall interaction process.

Because equation (5.3-21) deals directly with the total electric field, it is easier to show that the $\nabla\nabla\cdot$ operator may be neglected in that equation than in (5.3-26). In two-dimensional configurations, where the y-dimension is commonly neglected, the $\partial/\partial y\mathbf{E}(\mathbf{r},t)$ equals zero. If the incident field is polarized along the y-direction, the $\nabla\nabla\cdot$ operator drops out of the equation. More formally, the desired term in (5.3-21) becomes

$$\begin{aligned}\nabla\nabla\cdot\varepsilon'\mathbf{E} &= \nabla[\varepsilon'\nabla\cdot E + (\nabla\varepsilon')\cdot E] \\ &= \nabla(\varepsilon'\frac{\partial E_y}{\partial y} + E_y\frac{\partial\varepsilon'}{\partial y}) = 0.\end{aligned} \tag{5.3-27}$$

The last term in (5.3-27) must equal zero because neither E_y nor ε' depend on y. In three dimensional configurations, the $\nabla\nabla\cdot$ operator does not vanish because both $\mathbf{E}$ and ε' possess all three coordinates. Therefore, to justify the use of a scalar wave equation for three-dimensional acousto-optic interaction, polarization effects will be shown to be minimal. Throughout this argument the temporal variation of ε' is assumed to be much slower than that of the optical field $\mathbf{E}$. The $\partial/\partial t$ term produces results on the order of $k\varepsilon$ times the $\mathbf{E}$ field, where k is the propagation constant for light. $\nabla\nabla\cdot$ produces the following terms:

$$\nabla(\nabla\cdot\varepsilon'E) = (\nabla^2\varepsilon')E + 2(\nabla\cdot E)\nabla\varepsilon' + \varepsilon'\nabla(\nabla\cdot E) \tag{5.3.-28}$$

Each term in (5.3-28) must be negligible when compared to that produced by $\partial^2/\partial t^2$ (i.e. $k^2\varepsilon'\mathbf{E}$). The first is at most on the order $K^2\varepsilon'\mathbf{E}$. The second term has an upper bound equal to $kK\varepsilon\mathbf{E}$. Because $K \ll k$, both terms compare insignificantly to $k^2\varepsilon E$. Remember that light is assumed to propagate nominally in the positive z-direction. **E** must be perpendicular to this direction and therefore the last term in (5.3-28) is at most of the order $k^2\sin(\phi_{inc})\mathbf{E}$. However, because $\phi_{inc} \ll 1$ (paraxial approximation), this term may also be neglected.

The $\nabla\nabla\cdot$ term in equation (5.3-26), may be neglected by using the same arguments outlined above. Consequently, equation (5.3-25) becomes:

$$\mathbf{E}(\mathbf{r},t) = -\mu\varepsilon\,\frac{\partial^2\Pi(\mathbf{r},t)}{\partial t^2}. \tag{5.3-29}$$

Finally, differentiating (5.3-26) twice and using (5.3-29) leads to the following equation for strong acousto-optic interaction in three dimensions:

$$\nabla^2\psi(\mathbf{r},t) - \mu\varepsilon_0\,\frac{\partial^2\psi(\mathbf{r},t)}{\partial t^2} = \mu\varepsilon'(\mathbf{r},t)\,\frac{\partial^2\psi(\mathbf{r},t)}{\partial t^2} \tag{5.3-30}$$

where $\psi(\mathbf{r},t)$ refers to an arbitrary polarization component.

5.3.2 Description of the Algorithm

The wave-equation approach begins with the scalar wave equation in (5.3-30) with ε' defined as follows:

$$\varepsilon'(\mathbf{r},t) = \varepsilon_0 C \, \mathrm{Re}\left[S_e(\mathbf{r}) \exp\left[j\Omega t - Kx\right]\right]. \tag{5.3-31}$$

$S_e(\mathbf{r})$ is the complex envelop, C is a material constant, Ω is the temporal sound frequency, and K is the propagation constant for sound. $\psi(\mathbf{r},t)$ is assumed to be time harmonic and is defined as

$$\psi(\mathbf{r},t) = \sum \mathrm{Re}\left[\psi_{em}(\mathbf{r}) \exp\left[j\{(\omega + m\Omega)t - k_{mx}x - k_{mz}z\}\right]\right], \tag{5.3-32}$$

where m is an integer, ω is the temporal light frequency, k_{mx} and k_{mz} are the propagation constants for the mth order light field, and ψ_{em} is the complex envelope of the mth order light field at frequency $(\omega + m\Omega)$. The propagation constants, k_{mx} and k_{mz}, can be described by reviewing figure 5.1 and figure 3.2. Light travels in the nominal z-direction at an angle ϕ_B with respect to the z-axis. This means the propagation vector is made up of two components, k_x, and k_z, defined as follows:

$$\begin{aligned} k_x &= k_0 \sin(-\phi_B) \\ k_z &= k_0 \cos(-\phi_B). \end{aligned} \tag{5.3-33}$$

Applying this concept to figure 3.2 allows us to express the propagation constants for each diffracted order in a form similar to that in (5.3-33). Notice that the light beam is incident at an angle equal to $-\phi_B$ thereby allowing for upshifted interaction. The incident order emerges from the acousto-optic interaction as the zero diffracted order with propagation constants equal to those in equation (5.3-33). From discussions in chapter 3, we know that the first

diffracted order is deflected in a direction that is $2\phi_B$ greater than that of the zero order. This effectively leads to propagation in the ϕ_B direction. Due to the finite interaction region, higher orders are produced in directions $2\phi_B$ away from the zero and first diffracted orders, respectively. Hence, $\mathbf{E}_{(-1)}$ and $\mathbf{E}_{(-2)}$ both travel in directions $\pm 3\phi_B$ with respect to the z-axis. Clearly there is a pattern where a diffracted order appears at every odd multiple of ϕ_B. Consequently the propagation constants, k_{mx} and k_{mz} can be represented by:

$$\begin{aligned} k_{mx} &= k_0 \sin\left[(2m-1)\phi_B\right] \\ k_{mz} &= k_0 \cos\left[(2m-1)\phi_B\right]. \end{aligned} \tag{5.3-34}$$

Substituting (5.3-31) and (5-3-32) into (5.3-30) yields a mth order set of coupled differential equations for acousto-optic interaction.

$$\begin{aligned} \psi_{e(m),xx} + \psi_{e(m),yy} - 2jk_0[\psi_{e(m),x} k_{mx} + [\psi_{e(m),z} k_{mz}] \\ + \frac{1}{2}k^2{}_0 CS_e(r)\psi_{e(m-1)} + \frac{1}{2}k^2{}_0 CS_e^{*}(r)\psi_{e(m+1)} \end{aligned} \tag{5.3-35}$$

The physics behind equation (5.3-35) imply that mth order scattered light in z depends on interactions between adjacent orders (m±1) with sound and the effect of propagational diffraction. Restricting the system of equations to four diffracted orders, m = -1, m = 0, m = 1, and m = 2 leads to:

$$\psi_{e(-1),xx} + \psi_{e(-1),yy} - 2jk_0[\psi_{e(-1),x}\sin(-3\phi_B) + \psi_{e(-1),z}\cos(-3\phi_B)] + \frac{1}{2}k_0^2 CS_e^*(\mathbf{r})\psi_{e(0)} = 0 \tag{5.3-36a}$$

$$\psi_{e(0),xx} + \psi_{e(0),yy} - 2jk_0[\psi_{e(0),x}\sin(\phi_B) + \psi_{e(0),z}\cos(\phi_B)] + \frac{1}{2}k_0^2 CS_e(\mathbf{r})\psi_{e(-1)} + \frac{1}{2}k_0^2 CS_e^*(\mathbf{r})\psi_{e(1)} = 0 \tag{5.3-36b}$$

$$\psi_{e(1),xx} + \psi_{e(1),yy} - 2jk_0[\psi_{e(1),x}\sin(\phi_B) + \psi_{e(1),z}\cos(\phi_B)] + \frac{1}{2}k_0^2 CS_e(\mathbf{r})\psi_{e(0)} + \frac{1}{2}k_0^2 CS_e(\mathbf{r})\psi_{e(2)} = 0 \tag{5.3-36c}$$

$$\psi_{e(2),xx} + \psi_{e(2),yy} - 2jk_0[\psi_{e(2),x}\sin(3\phi_B) + \psi_{e(2),z}\cos(3\phi_B)] + \frac{1}{2}k_0^2 CS_e(\mathbf{r})\psi_{e(1)} = 0 \tag{5.3-36d}$$

where the subscripts xx, yy, and z refer the $\partial^2/\partial x^2$, $\partial^2/\partial y^2$, and $\partial/\partial z$, respectively. From figure 3.2 and equation (5.3-34), $k_{(-1)x} = -k_0\sin(3\phi_B)$, $k_{(-1)z} = k_0\cos(3\phi_B)$, $k_{(0)x} = -k_0\sin(\phi_B)$, $k_{(0)z} = k_0\cos(\phi_B)$, $k_{(1)x} = k_0\sin(\phi_B)$, $k_{(1)z} = k_0\cos(\phi_B)$, $k_{(2)x} = k_0\sin(3\phi_B)$, $k_{(2)z} = k_0\cos(3\phi_B)$, and ϕ_B is the Bragg angle defined earlier. Because $\phi_B \ll 1$, the sine and cosine of the Bragg angle (or 3 times the Bragg angle) equals zero and one, respectively. The above equations reduce to the

following simplified form:

$$\psi_{e(-1),z} = -\frac{j}{2k_0}[\psi_{e(-1),xx} + \psi_{e(-1),yy}] - \frac{j}{4}k_0 CS_e^{*}(\mathbf{r})\psi_{e(0)} = 0 \tag{5.3-37a}$$

$$\psi_{e(0),z} = -\frac{j}{2k_0}[\psi_{e(0),xx} + \psi_{e(0),yy}] - \frac{j}{4}k_0 CS_e(\mathbf{r})\psi_{e(-1)} - \frac{j}{4}k_0 CS_e^{*}(\mathbf{r})\psi_{e(1)} = 0 \tag{5.3-37b}$$

$$\psi_{e(1),z} = -\frac{j}{2k_0}[\psi_{e(1),xx} + \psi_{e(1),yy}] - \frac{j}{4}k_0 CS_e(\mathbf{r})\psi_{e(0)} - \frac{j}{4}k_0 CS_e^{*}(\mathbf{r})\psi_{e(2)} = 0. \tag{5.3-37c}$$

$$\psi_{e(2),z} = -\frac{j}{2k_0}[\psi_{e(2),xx} + \psi_{e(2),yy}] - \frac{j}{4}k_0 CS_e(\mathbf{r})\psi_{e(1)} = 0. \tag{5.3-37d}$$

Equations (5.3-37a) through (5.3-37d) are programmed using the split step method outlined in figure 5.12. Simulation results are presented in the following section.

$S_e(\mathbf{r})$ denotes an arbitrary sound beam. For demonstration purposes, the sound beam is chosen to be Gaussian. The profile of the Gaussian beam is assumed to have plane wavefronts close to the surface of the acoustic transducer. The sound field is assumed to exist in the y-z plane and travel nearly normal to the direction of the incident light field. The standard expression for diffraction of a Gaussian beam propagating in the x-direction is given

by equation (5.3-38) below:

$$S_e(y,z:x) = \frac{Aw_0}{w(x)} \exp\left[\frac{-(y^2+z^2)}{w^2(x)}\right] \exp\left[-j\frac{(y^2+z^2)}{2R(x)}\right] \exp\left[-j\phi(x)\right] \qquad (5.3\text{-}38a)$$

$$w^2(x) = w_0^2\left[1+(\frac{x}{x_R})^2\right], \quad x_R = K\frac{w_0^2}{2} \qquad (5.3\text{-}38b)$$

$$R(x) = \frac{(x^2+x_R^2)}{x}, \quad \phi(x) = -\tan^{-1}(\frac{x}{x_R}) \qquad (5.3\text{-}38c)$$

where w_0 is the arbitrary beam waist of the sound field. Equation (5.3-38c) removes the possibility of having x = 0 as a possible point of observation. Furthermore, since x = 0 gives the location of the transducer, including this point in the calculations does not represent the physical situation. Obviously, having the incident light beam far enough away from the transducer to have the entire incident light field interact with the diffracting sound field is desirable. This was accomplished by ensuring the center of the incident light beam was at least a distance equal to its beam waist away from the transducer. That is, if the light beam waist was 422um, then the beam was located approximately a distance of 500um away from the transducer (i.e. in the x-direction) to ensure interaction of the whole light field. As a starting point we assume the light and sound fields interact around x=L/2, where L is the width of the transducer. The sound pressure is defined in terms of the on axis amplitude of the sound field at x=L/2 to be $|S_e| = Aw_0/w(L/2)$. Looking closely at equation (5.3-37), notice that the terms $(j/4)k_0CS_e$ (or S_e^*) in each equation is similar to that for α defined in

equation (5.2-9). In fact we have $k_0C|S_e|/4$ which differs from α by a factor of 2L. Therefore if we multiply each side of (5.3-37) by L and let the derivative be with respect to ζ (where $\zeta = z/L$) instead of z, we have the same form as (5.2-9). Remember the peak amplitude of the Gaussian sound field equals $|S_e|$ and hence $\alpha = k_0C|S_e|L/2$. This allows (5.3-37) to be normalized to

$$\psi_{e(-1),\zeta} = -\frac{jL}{2k_0}[\psi_{e(-1),xx} + \psi_{e(-1),yy}] - j\frac{\alpha}{2}S_e^*(x,y,z)\psi_{e(0)} = 0 \qquad (5.3\text{-}39a)$$

$$\psi_{e(0),\zeta} = -\frac{jL}{2k_0}[\psi_{e(0),xx} + \psi_{e(0),yy}] - j\frac{\alpha}{2}S_e(x,y,z)\psi_{e(-1)} - j\frac{\alpha}{2}S_e^*(x,y,z)\psi_{e(1)} = 0 \qquad (5.3\text{-}39b)$$

$$\psi_{e(1),\zeta} = -\frac{jL}{2k_0}[\psi_{e(1),xx} + \psi_{e(1),yy}] - j\frac{\alpha}{2}S_e(x,y,z)\psi_{e(0)} - j\frac{\alpha}{2}S_e^*(x,y,z)\psi_{e(2)} = 0 \qquad (5.3\text{-}39c)$$

$$\psi_{e(2),\zeta} = -\frac{jL}{2k_0}[\psi_{e(2),xx} + \psi_{e(2),yy}] - j\frac{\alpha}{2}S_e(x,y,z)\psi_{e(1)} = 0 \qquad (5.3\text{-}39d)$$

The normalized sound field is given as:

$$S_e(y,z:x) = \frac{w(L/2)}{w(x)}\exp\left[\frac{-(y^2+z^2)}{w^2(x)}\right]\exp\left[-jk\frac{(y^2+z^2)}{2R(x)}\right]\exp[-j\phi(x)] \qquad (5.3\text{-}40)$$

Equation (5.3-40) states that the magnitude of the diffracted profile remains Gaussian, however, it now has an amplitude that decreases and a waist that increases with propagation. Within any transverse plane, the sound field intensity assumes its peak value on the beam axis and drops to 14% of its original value when either transverse coordinate (y, z) coincides with the radial distance w(x). Therefore, w(x) is regarded as the beam radius or beam width. It assumes its minimum value, w_0, at the x=0 plane, and $2w_0$ refers to the spot size. The beam waist increases with x reaching $\sqrt{2}w_0$ at $x = x_R$ and increases monotonically with x thereafter. Equation (5.3-38c) gives an expression for the radius of curvature for the propagating Gaussian beam. At $x = x_R$ the radius of curvature has its minimum value and therefore the wavefront has its greatest curvature. Starting at x = 0, the radius of curvature first decreases from infinity (a plane wave) to a minimum value before starting to increase again. For large values of x, the radius of curvature approximately equals x. The effect of changing the radius of curvature and beam width appears in section 5.4. In particular, the parameters above enables us to choose a sound field with sufficient curvature to modify the incident optical field. As evident in section 5.4, we find that curvatures along y have a significant impact on the shape of the zero diffracted order.

5.3.3 Comparison with Fourier-Optics Approach

Figure 5.12 shows the flow diagram for the wave-equation approach. A major disadvantage of this method is that separate FFTs must be calculated for each individual order. This leads to execution times on the order of "n-times" that for the Fourier-optics method. Like the Fourier-optics method, this method propagates the solution at the exit of

the Bragg cell 84cm to simulate the experimental situation. Figures 5.4-5.6 show that our results agree well with the previously verified Fourier-optics method. Likewise, figure 5.13 shows qualitative agreement with the three-dimensional plots in figure 5.10. For completeness, figure 5.14 provides plots of the minus-1 and second diffracted orders. Since the wave-equation method uses a Gaussian sound field, we approximated the rectangular sound column with a large sound waist for the sound beam. In the figures for comparison we used a symmetric sound waist equal to 10.0cm. Although this method incorporates diffraction of the sound field into the diffraction process, the plots in figure 5.13 and 5.14 are really results due to interaction with a rectangular sound field. This is because a sound waist of 10cm looks like a plane wave to the incident light beam. As in the case for the Fourier-Optics approach, the spatial distribution plots were generated for a distance of 84cm from the exit of the Bragg cell. Again, the purpose of these graphs is to show that the wave-equation approach agrees well with the Fourier optics approach. Unique findings due to using a Gaussian sound field is included in following section.

5.4 Physical Interpretations and Insights

Up to this point we have been primarily concerned with validating the two split-step methods. Chapter 6 presents experimental results that verify simulation results in figures 5.10 and 5.13. This section also verifies results for two-dimensional spatial plots in figure 6.3. This section looks deeper into three-dimensional acousto-optic interaction. First, we use the Fourier-optics approach to investigate the effects caused by using large Q values. Next, we use the wave-equation approach to investigate how changes in the sound beam's waist and

radius of curvature affect the interaction process. We include three-dimensional plots in the spatial domain with special attention given to how the sound cell modifies the profile of the zero and first diffracted orders. Our desire is to discover cases when the first diffracted order deviates from its expected Gaussian shape in a noticeable way.

Two-dimensional effects of large Q values were presented in chapter 4 via the transfer function formalism. Here we also investigate diffraction efficiency and beam shaping as a function of Q. Because three-dimensional transfer functions are not yet available for Bragg cells, we chose values of Q in an ad hoc manner based solely on the two-dimensional transfer function. Chapter 4 also investigates how strong sound pressures affect two-dimensional acousto-optic interaction and how beam distortion appears and disappears at certain values of α. Figure 5.15 (a-d) show three-dimensional spatial plots of the first diffracted order for large values of Q. The graphs are consistent with those presented in chapter 4 and reference[50]. It is important to note that figure 4.6b uses a normalized scale while figure 5.15d scales its data in millimeters. This difference is due in part to how each algorithm produces its data. The transfer function approach in section 4.1.3 relies only on the ratio of the optical beam waist to the sound wavelength (i.e. σ_1/Λ). The Fourier-optics approach (and the wave equation approach) accepts the beam waist and sound wavelength in millimeters. Comparing the input Gaussian beam's width to the width of the distorted diffracted order provides a basis for relating the two algorithms. In figure 4.6b, the ratio of the Gaussian light beam's spot size to the width of the diffracted order is approximately 2.34, where the normalized width of the input beam and the diffracted beam equals 2.78 and 6.5, respectively. Likewise, the ratio of

the two beams in figure 5.15d equals 2.6 since the input Gaussian beam's width equals 0.84mm and the diffracted order's width is 2.2mm. The discrepancy between the two ratios is caused by σ_1/Λ. That is, figure 4.6b corresponds to the case where $\sigma_1/\Lambda = 5$ and figure 5.15d corresponds to $\sigma_1/\Lambda = 4.2$. By increasing the beam waist from 422um to 508um (i.e. $\sigma_1/\Lambda = 5$) the ratio of the input Gaussian beam's width to the width of the distorted order equals 2.38, which is almost identical to the ratio computed in figure 4.6b. This change also caused the intensities of the diffracted orders to be equal.

The results presented in figure 5.15 is determined from the interaction between a Gaussian light beam and a rectangular sound column. Since results due to the wave-equation approach for sound waists equal those from the Fourier-Optics approach, either method may be used to produce the plots in figure 5.15. In fact, to ensure the integrity of the algorithms, the four graphs in figure 5.15 (a-d) were produced separately by each method. Using a point by point comparison, the two method agreed to within 5 significant digits. Now we investigate how the sound waist affects the intensity of the zero and first diffracted orders. Equation (5.3-40) describes the sound field envelope for a symmetric Gaussian acoustic beam. However, figure 3.4 implies that the beam waist of the sound field may be different in the y and z directions. We denote these waists as w_y and w_z, respectively. The actual Bragg cell introduced in chapter 6 has a width of 5.7cm and a height equal to 2.5cm. This further implies that different initial beam waists (and therefore radius of curvatures) exist for the y and z directions. Many different combinations may be chosen for a particular sound field. We chose to investigate the effects of each waist separately, thereby leaving the combined

effect of different waists for a later discussion. In fact, we expect this combined effect to exist within the two extremes.

We begin with investigating the effects cause by changing w_z. As a baseline, we start with $w_y = w_z = 10$cm since the sound field approximates a plane wave at these waists. However, when w_z decreases from 10cm to 1cm, the profile of the sound field no longer resembles a plane wave front and the amount of light diffracted into the first order reduces. Figure 5.16 plots the diffraction efficiency as a function of w_z, where Q equals 14.64, w_y equals 10cm, the light beam waist equals 422um, and the distance away from the transducer equals 0cm (i.e. at the exit of the transducer). Diffraction efficiency is defined as the ratio of the peak intensity of the first diffracted order divided by the peak intensity of the incident light beam.

$$\text{Diffraction Efficiency} = \frac{I_1}{I_{inc}}, \tag{5.4-1}$$

where I_1 and I_{inc} refer to the first order and incident light beams, respectively. Since the output is already normalized to the input light intensity, diffraction is automatically produced by the wave-equation approach. As w_z falls below the width of the acousto-optic cell, 5.7cm, the efficiency falls off more rapidly. This is due to the effective reduction of the acousto-optic interaction region. In other words, the Bragg cell begins to resemble a thinner cell and the effect the sound field has on the light beam resembles the Raman Nath effect. When the sound field becomes narrower, the ability of the cell to deflect light into only the first order

diminishes. Because the sound wave diffracts as it propagates, one may expect the diffraction efficiency to decrease as the incident beam moves away from the transducer. Because the amplitude of the sound field falls as it spreads, the wider interaction region is negated by a decreasing sound pressure. That is, the effective α of the sound field decreases and acousto-optic interaction no longer operates with at the peak phase delay condition. In addition, for distances away from the transducer less than x_R, the sound field's radius of curvature continues to decrease (i.e. the curvature of the actual sound field profile increases). For the case when the initial beam waist, w_z, equals 2cm (i.e. well within the width of the sound cell), x_R approximately becomes 12 meters. Normally the width of a sound cell, say 10cm or less, is much less than our computed x_R. Figure 5.17a and 5.17b show two-dimensional plots of the zero and first diffracted orders due to a light beam interacting with a Gaussian sound field that has an initial beam waist w_z = 2cm and w_y = 10cm. Both figures assume the light beam is incident 1mm away from the transducer. Less light is deflected into the first order than in figure 5.13 (where the sound field approximates a plane wave). Also, there is no splitting in the zero order since the sound field no longer resembles a plane wave (due to the Gaussian fall off at the edges of the cell). Moving the light beam even further away from the transducer has little effect on the profiles of the diffracted orders. However, it has significant impact on the amplitude of the diffracted orders. This is due to the reduction of the sound field as it propagates in the x direction.

We now turn our attention to changing the waist of sound field beam along the y direction (i.e. w_y). Because we are dealing with a finite height transducer, approximating the

sound field as an infinite plane wave does not accurately model the system. Beam waists smaller than 2.5cm (the actual height of our experimental cell) can affect the light beam since the curvature of the sound beam may be seen by the incident light beam. The real constraint is the relative sizes of the light beam and the sound beam. Our investigation begins with w_y = 10mm where the results are identical to those in figure 5.13. That is, the sound field resembles a plane wave whenever w_y and w_z are greater than 10cm. Next we reduce w_y to 1mm which corresponds to an initial sound beam diameter (spot size) of 2mm, i.e., still larger than the incident light beam's spot size 0.84mm. We investigate the interaction when the sound field has traveled 1mm away from the transducer. According to equation (5.3-38b) and (5.3-38c) this corresponds to a nominal beam waist and radius of curvature at interaction equal to 1.02mm and 986mm, respectively. The sound field profile still resembles a plane wave and therefore the diffracted orders should resemble those of figure 5.13. From discussions in section 5.2.3, an incident light beam can see the curvature caused by the Gaussian sound field. The effects of this field is shown in figure 5.18a and 5.18b. While the first diffracted order maintains its Gaussian shape, the zero order looses some of its dip in the center and the right hump seems to spread in the y direction. This effect is emphasized in figure 5.20c, where the initial sound waist equals 0.5mm (i.e. spot size = 1mm) and the beam waist and radius of curvature at interaction becomes 0.53mm and 61.8mm, respectively. Because our experimental Bragg cell has a height of 2.5cm (i.e. ± 12.5mm), the curvature on the order of those above provides sufficient deviation away from planar wavefronts to affect the incident light beam. Interaction with these wavefronts provides the splitting along the y

direction. Physically, the curved wavefronts of the propagating sound field generate a more complex spatial field that is made up of more than one spatial frequency (plane wave). The incident light field interacts with this field and therefore produces a diffracted field that is corrupted by the additional spatial frequencies. The exact component of the sound field that causes splitting in the y-direction is an area for further study.

Figure 5.19 demonstrates that a sound profile with a curvature in the y direction has an effect on the diffraction efficiency and the overall shape of the zero diffraction order. Furthermore, it shows for the first time that additional information is given by the three-dimensional split-step algorithm. As in the case for w_z, it is important to investigate the effects of light beam location on the results of figure 5.18. We expect the sound field to spread as it propagates away from the transducer in the x direction . This allows interaction between the incident light field and a wider cross-section of the sound field. However, the sound field still reduces in amplitude as it propagates and therefore provides interaction with a weaker sound field. Figure 5.19 plots diffraction efficiency versus beam location for w_y = 1mm and w_z = 10.0cm. This choice of w_y and w_z allows the sound field to resemble a cylindrical wave that also coincides with experimental parameters of the sound cell used. For example, the acousto-optic cell used in the experiments has an effective acoustic beam height of 2mm which is equal to the spot size of our simulated sound beam. Remember that by choosing a waist equal to 10.0cm along the z-direction simply says that we have a plane wave along z (i.e. no curvature along the propagation direction of the light beam through the cell). These findings agree with experimental observations. That is, diffraction into the first order

reduces as the light beam is incident further away from the transducer.

Both split-step algorithms were used to generate the data in figure 5.15 through 5.20. Although many more graphs could have been presented to investigate the three-dimensional interaction process, this sample shows some of the powerful attributes of the methods. For the first time, we show that it is possible to incorporate sound diffraction and the y-dimension into the interaction process. Experimental verification of the data presented in this section requires special purpose acousto-optic Bragg cells, therefore, only simulation results are presented at this time. One should note that experimental results show splitting in the x and y directions of the zero order as will be shown later in figures 6.4a and 6.4b. We believe that the curvature in the y direction discussed above contributes to the observed distortion.

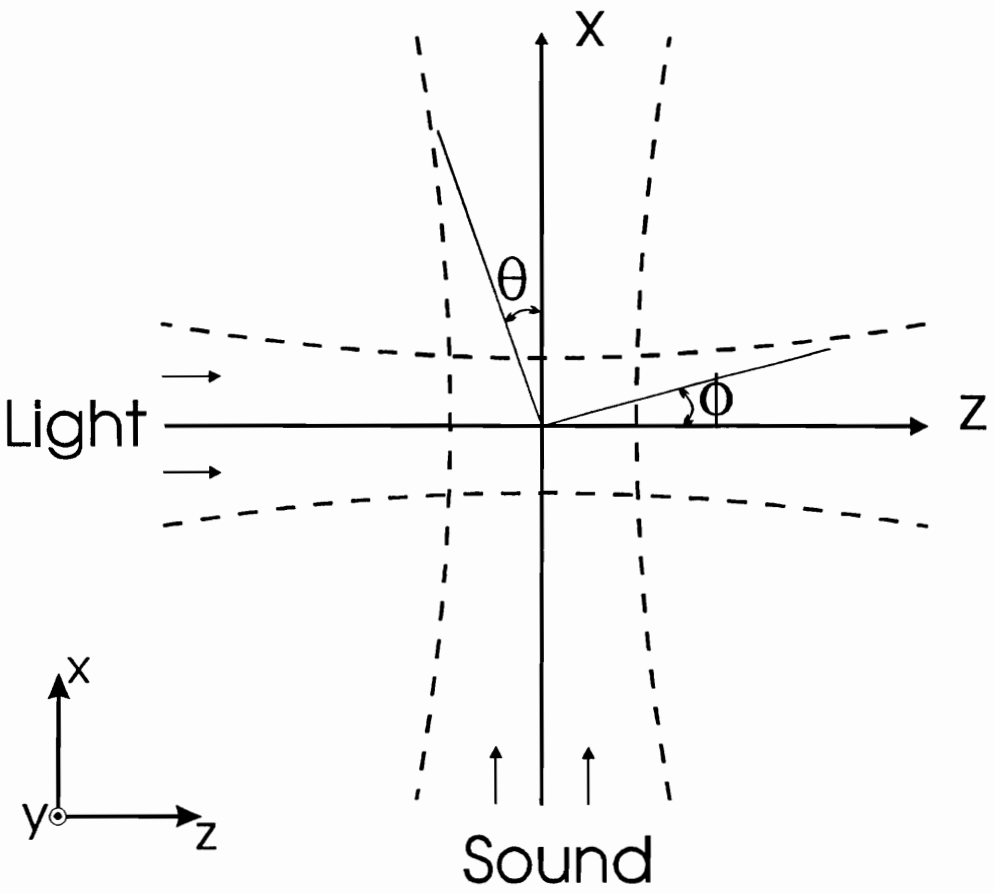

Fig. 5.1: Geometric configuration for acousto-optic interaction.

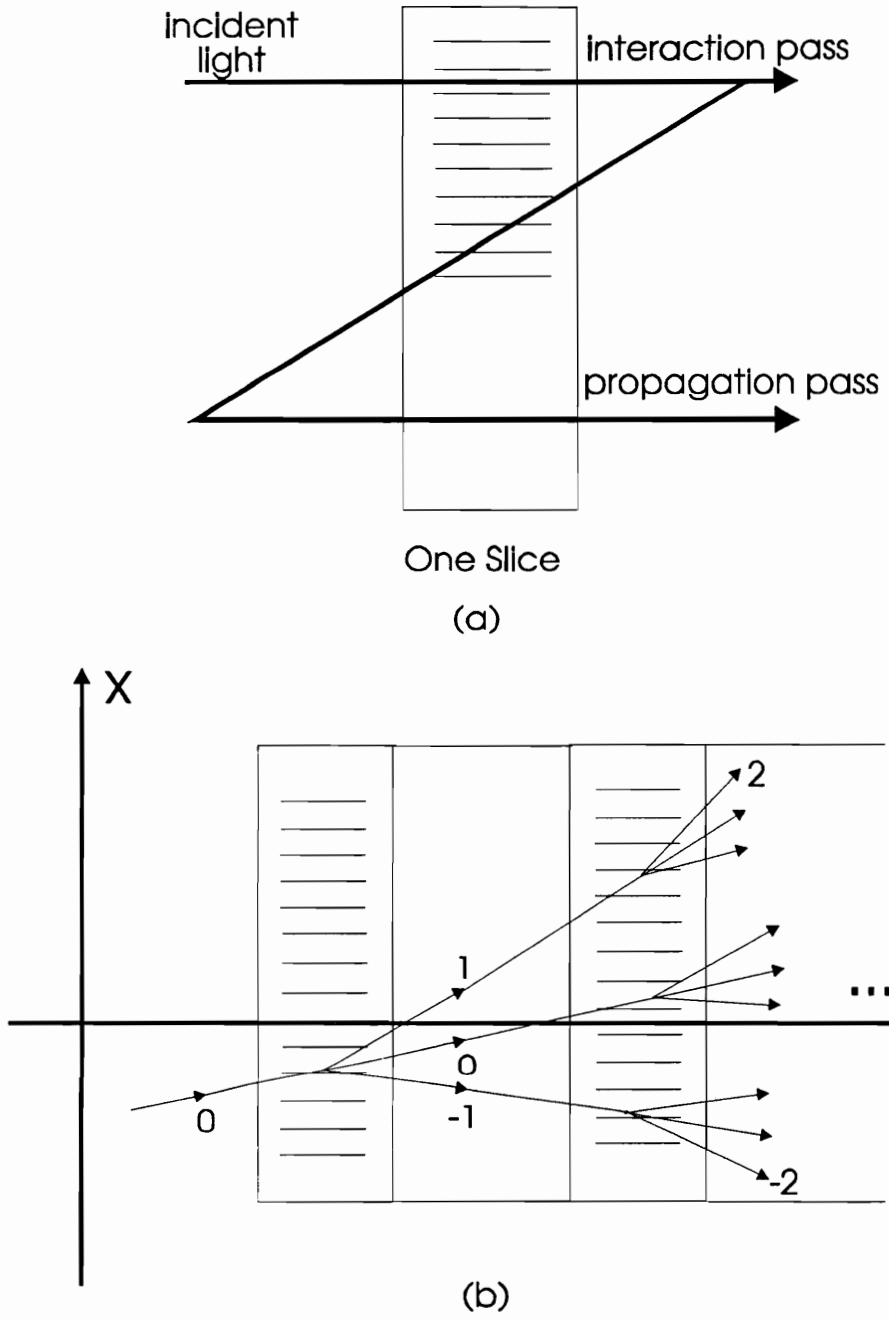

Fig. 5.2: (a) Split-step method propagates light thru each slice by alternating between interaction and diffraction, (b) Bragg diffraction implemented using cascaded thin phase gratings.

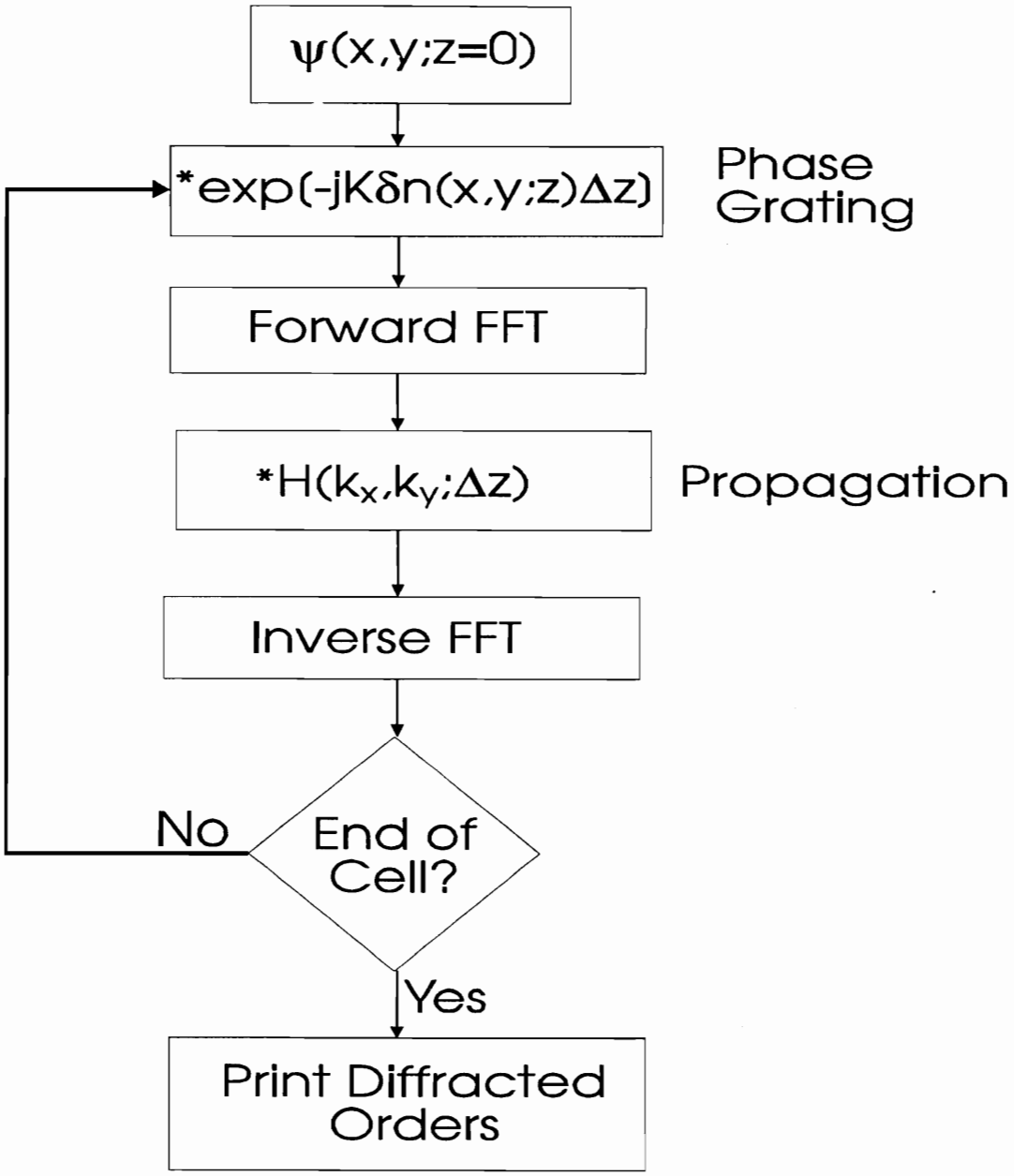

Fig 5.3: Flow diagram illustrating the Fourier-optics split-step algorithm.

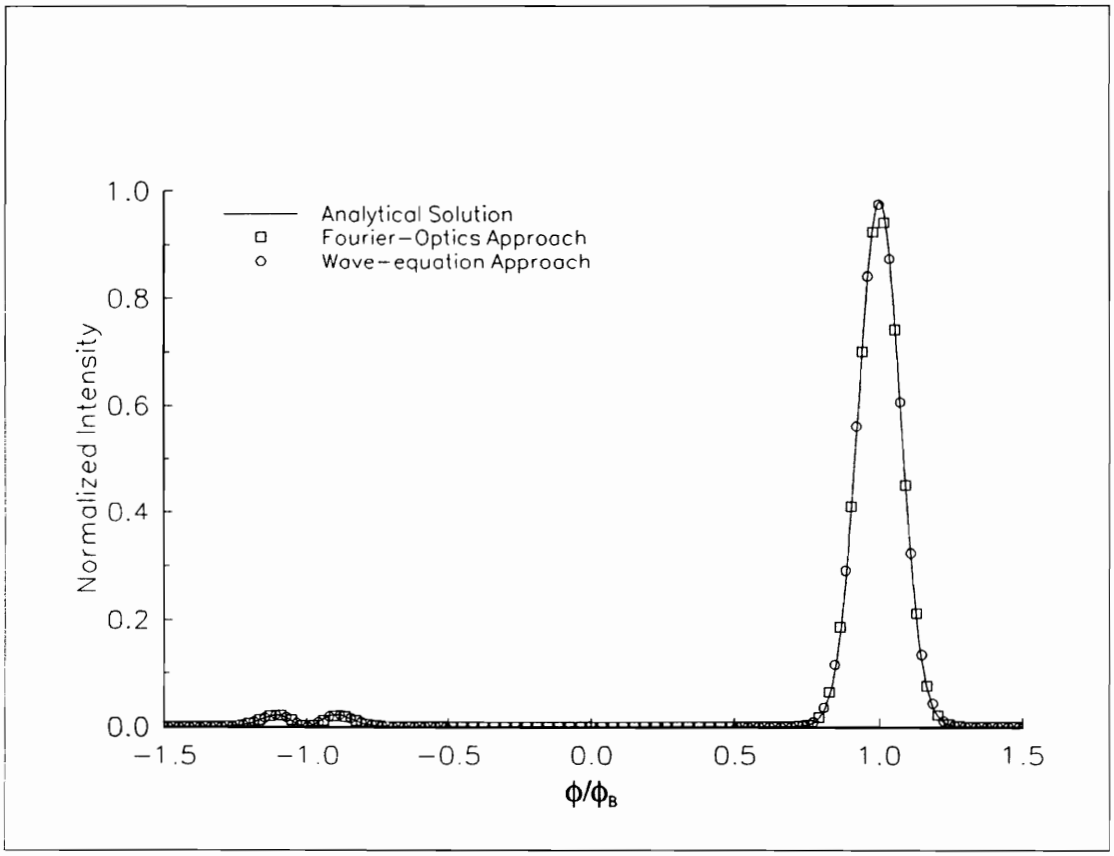

Figure 5.4: Comparison between analytical and simulation results. w_0 = 422um, $\alpha = \pi$, and Q= 14.64. For the Wave-equation approach, w_z = 10 cm, w_y = 10 cm, propagation distance = 0, and laser beam incident 1 mm away from transducer..

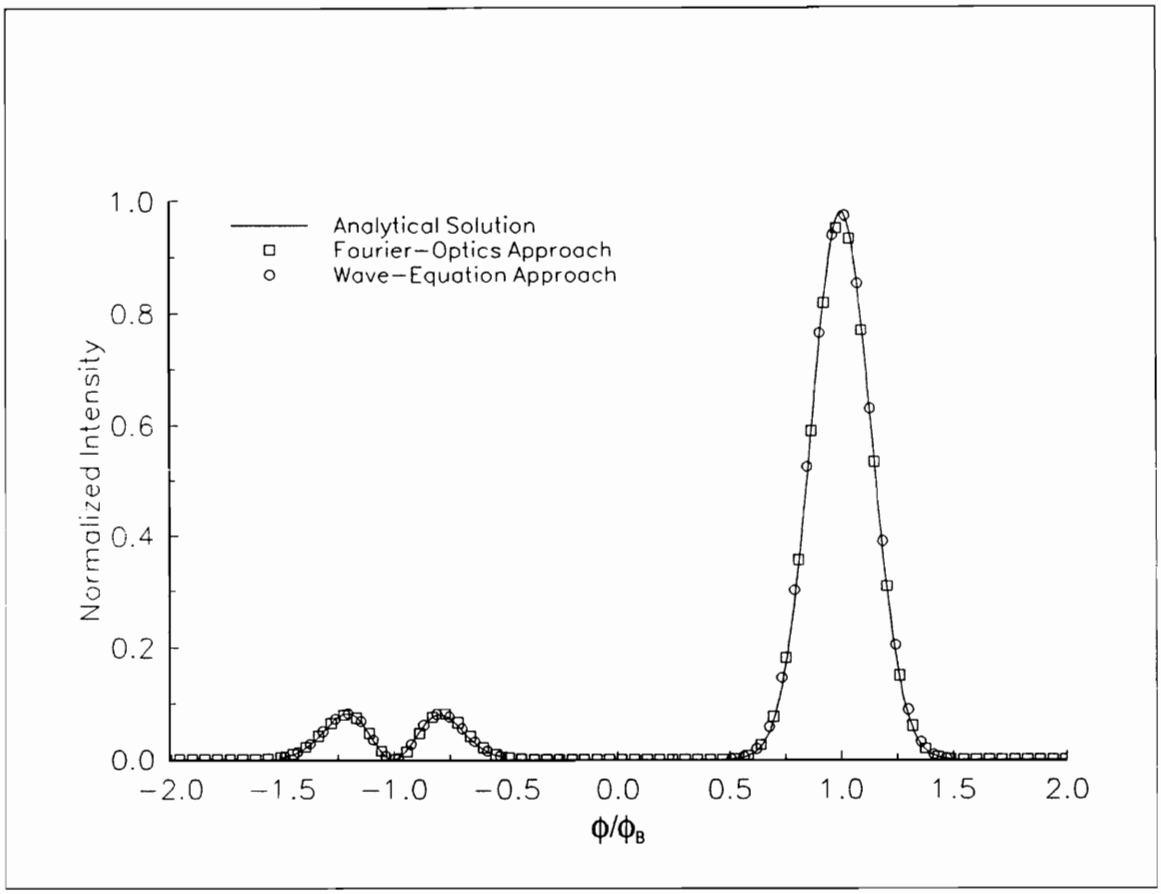

Figure 5.5: Comparison between analytical and simulation results. w_0 = 211um, $\alpha = \pi$, and Q= 14.64. For the Wave-equation approach, w_z = 10 cm, w_y = 10 cm, propagation distance = 0, and laser beam incident 1 mm away from transducer..

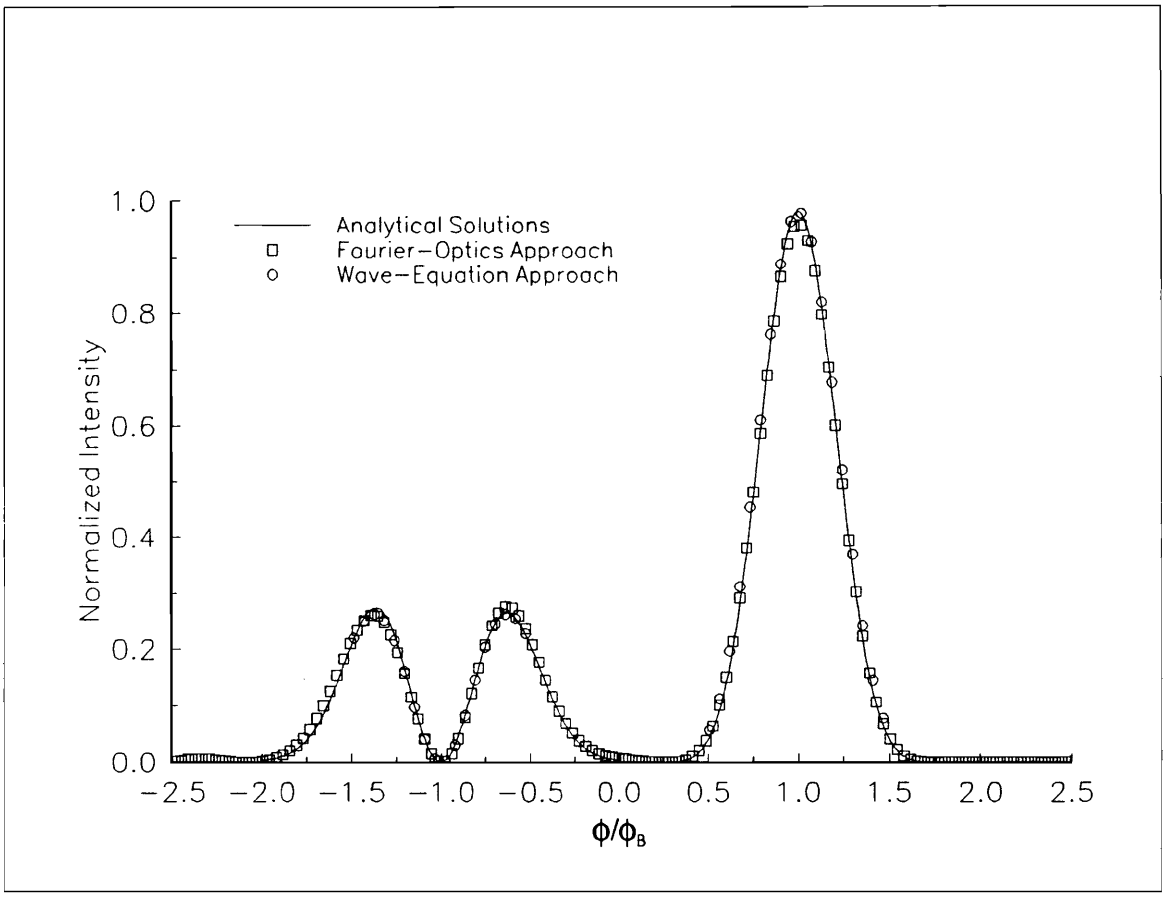

Figure 5.6: Comparison between analytical and simulation results. w_0 = 105um, $\alpha = \pi$, and Q= 14.64. For the Wave-equation approach, w_z = 10 cm, w_y = 10 cm, propagation distance = 0, and laser beam incident 1 mm away from transducer..

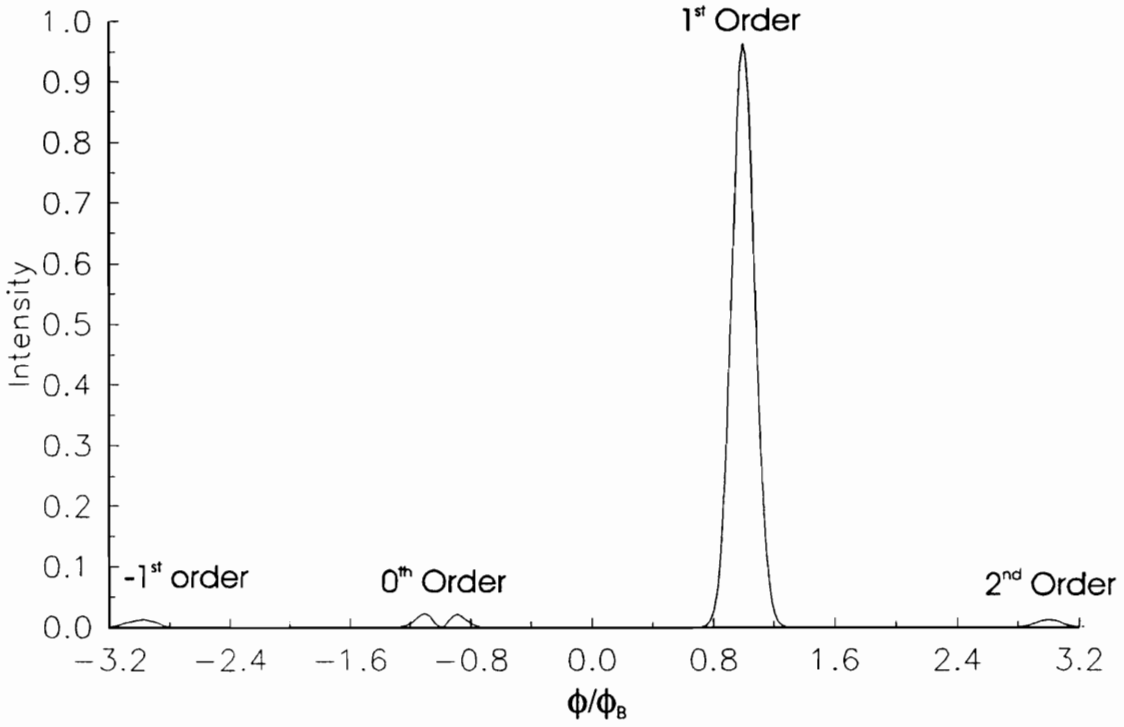

Figure 5.7: Fourier-optics simulation results showing 4 diffracted orders. The spectrum is normalized to the Bragg angle.

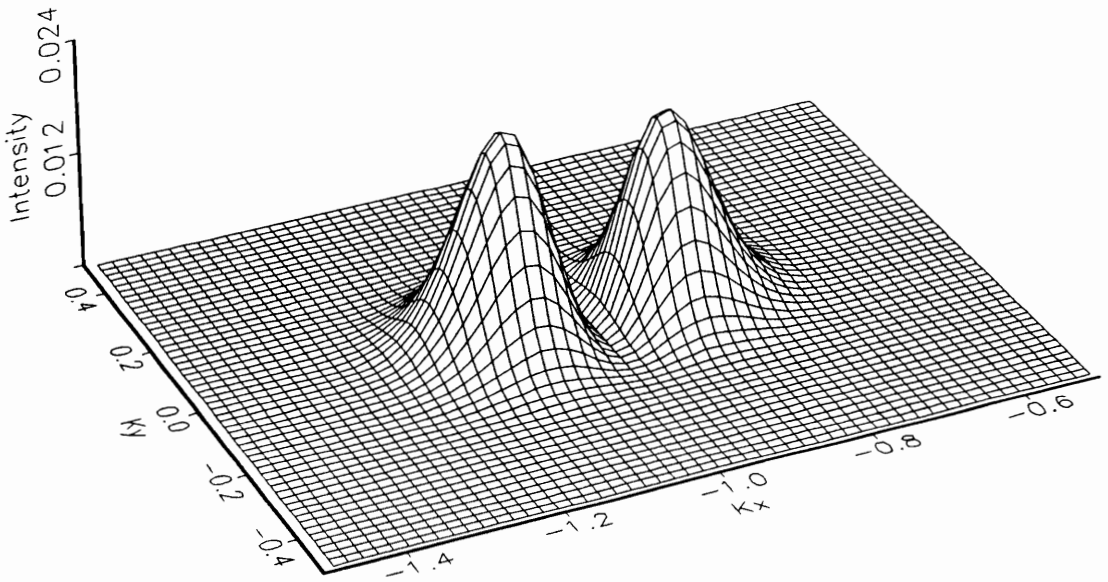

(a)

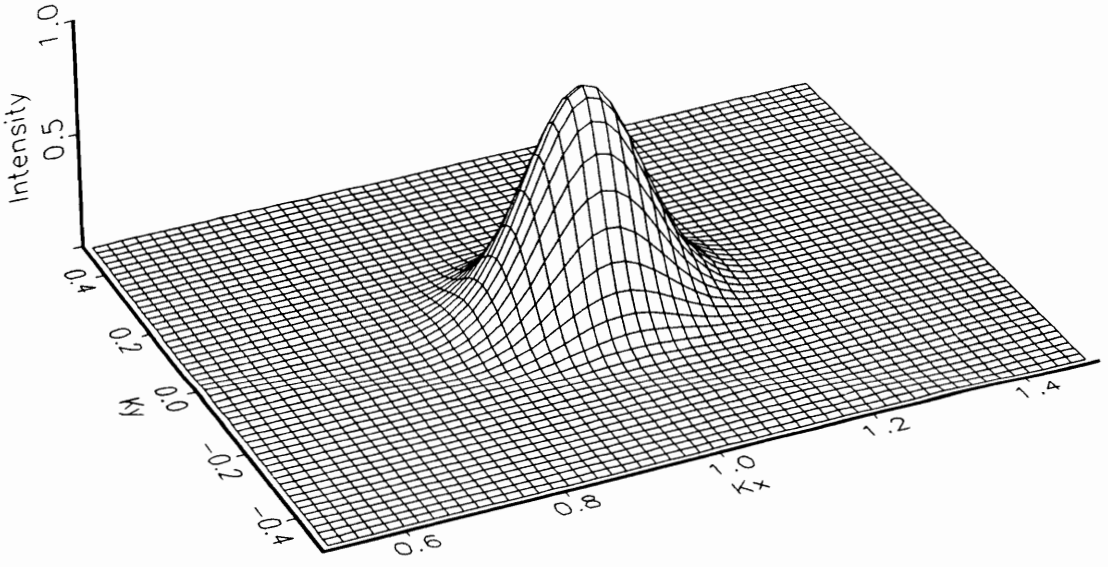

(b)

Fig 5.8: 3-D simulation results for (a) zero-order, (b) first order. The angles are normalized to the Bragg angle, w_0 = 422um, $\alpha=\pi$, Q=14.64..

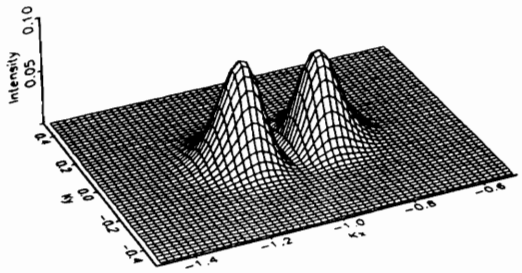

(a)

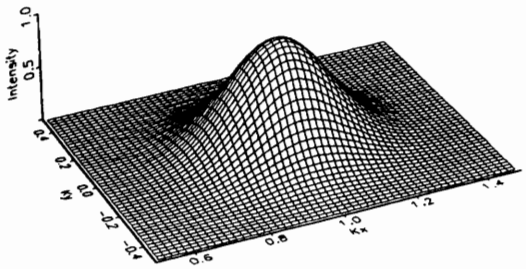

(b)

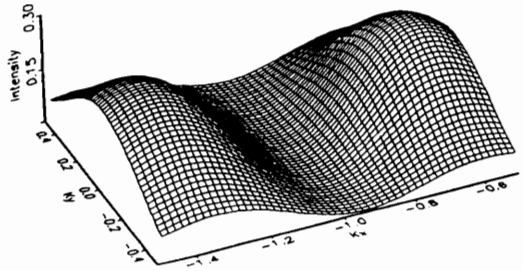

(c)

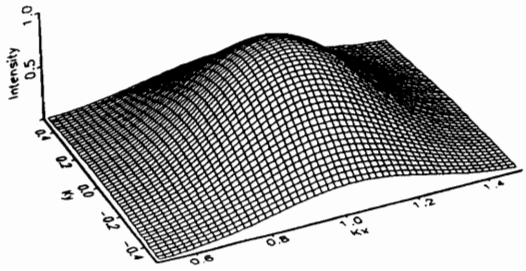

(d)

Fig 5.9: 3-D simulation results for w_0 =211um and w_0 =105 um. (a,c) zero-order, (b,d) first order. The angles are normalized to the Bragg angle, $\alpha=\pi$, Q=14.64.

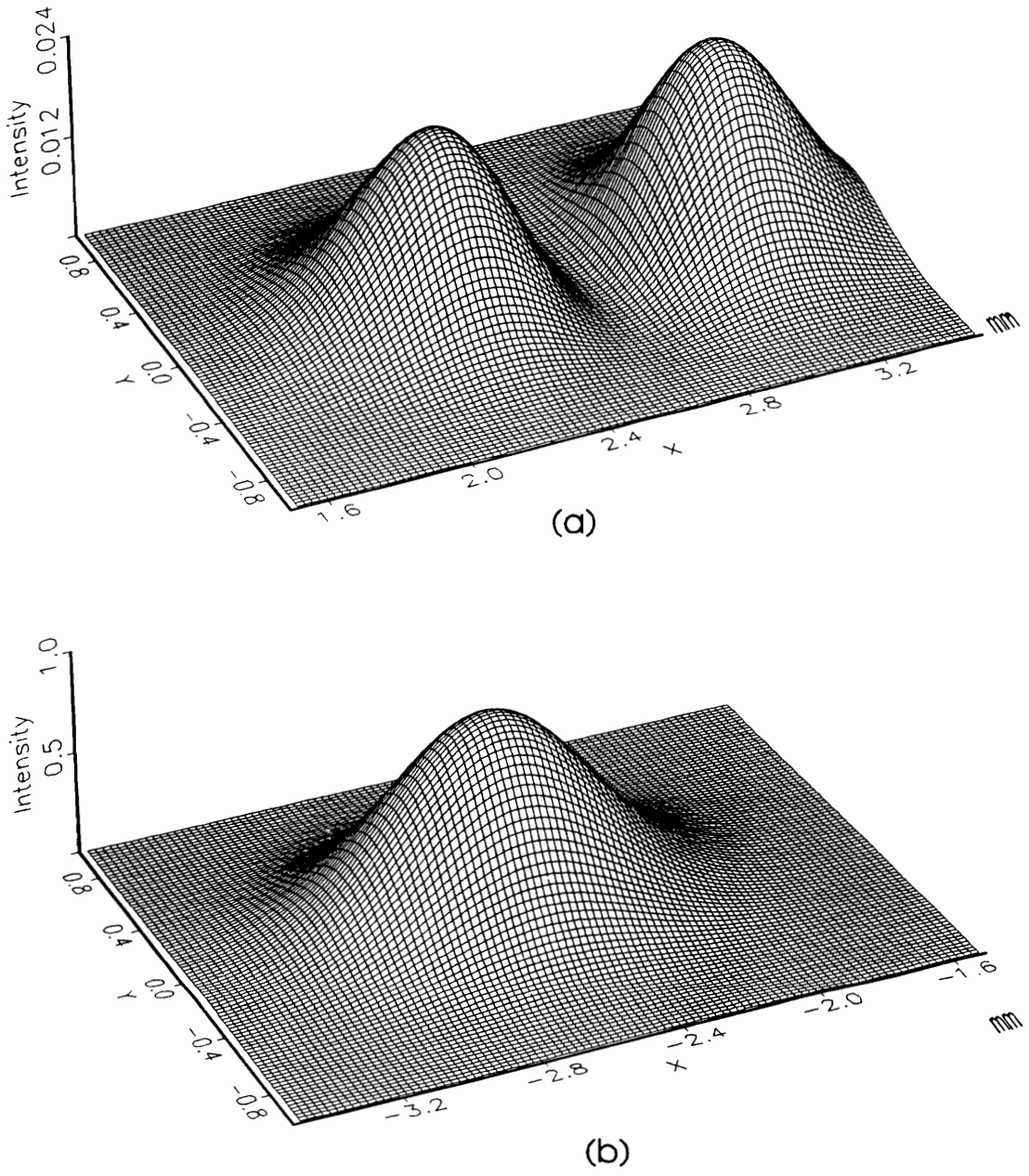

Fig. 5.10: (a) Spatial plot due to zero-order spectrum in 5.8a. (b) Spatial plot due to first-order spectrum in 5.8b.

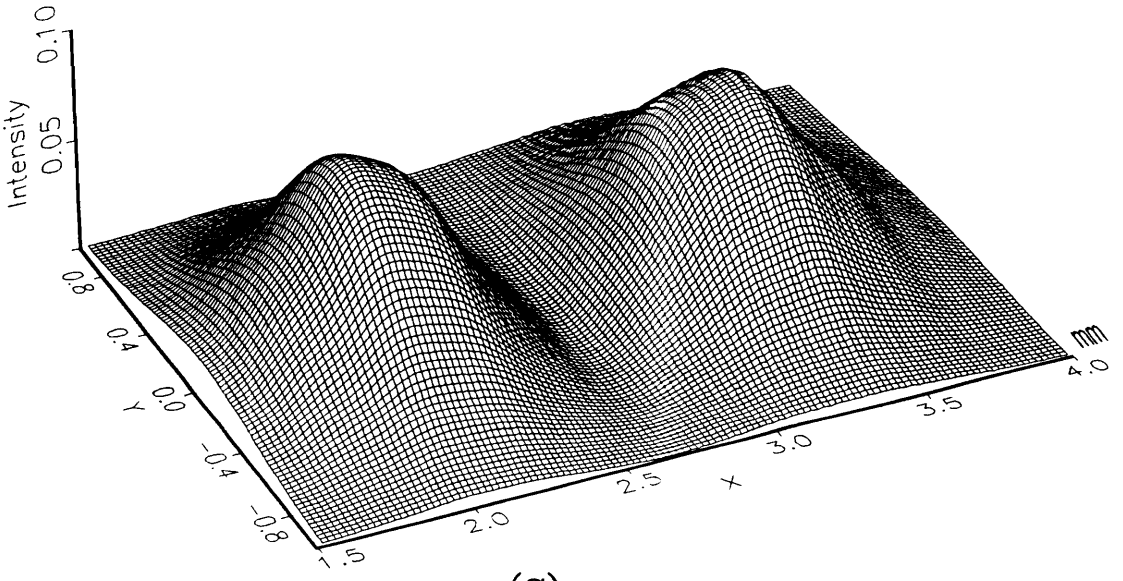

(a)

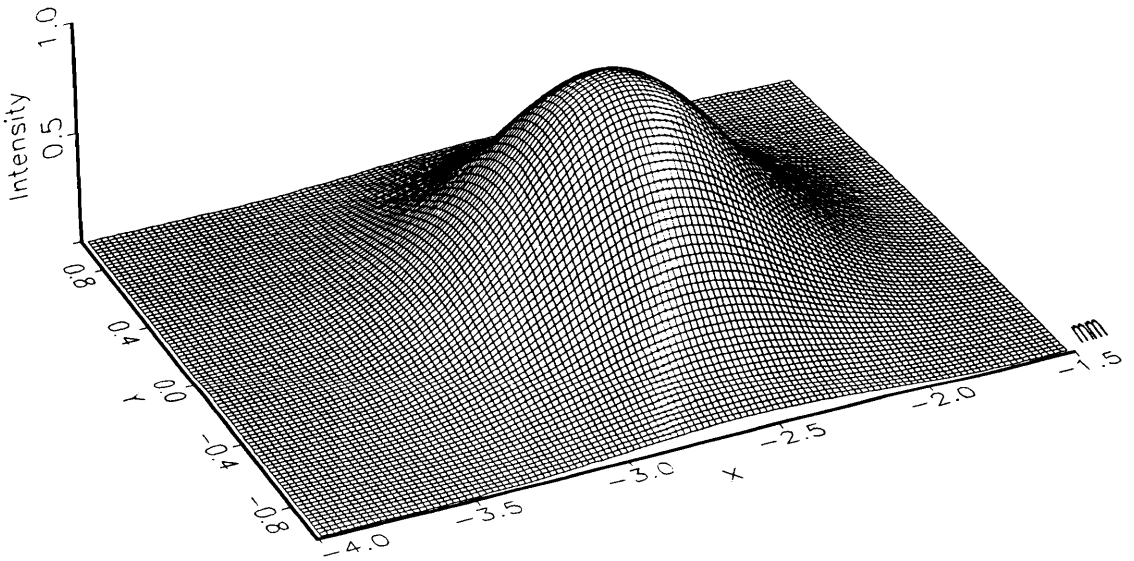

(b)

Fig. 5.11: (a) Spatial plot due to zero-order spectrum in 5.9a. (b) Spatial plot due to first-order spectrum in 5.9b.

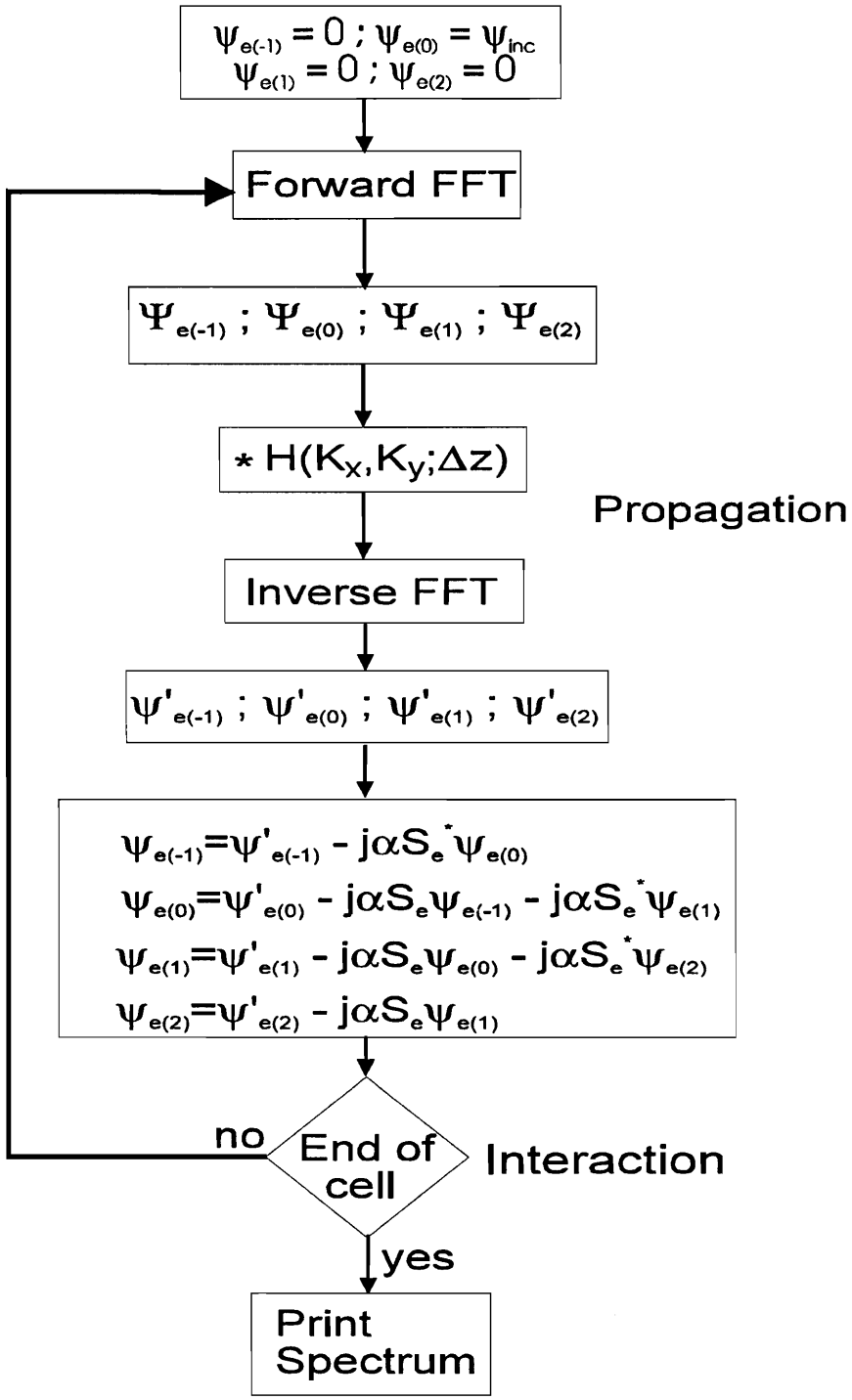

Figure 5.12: Flow Diagram illustrating wave-equation approach.

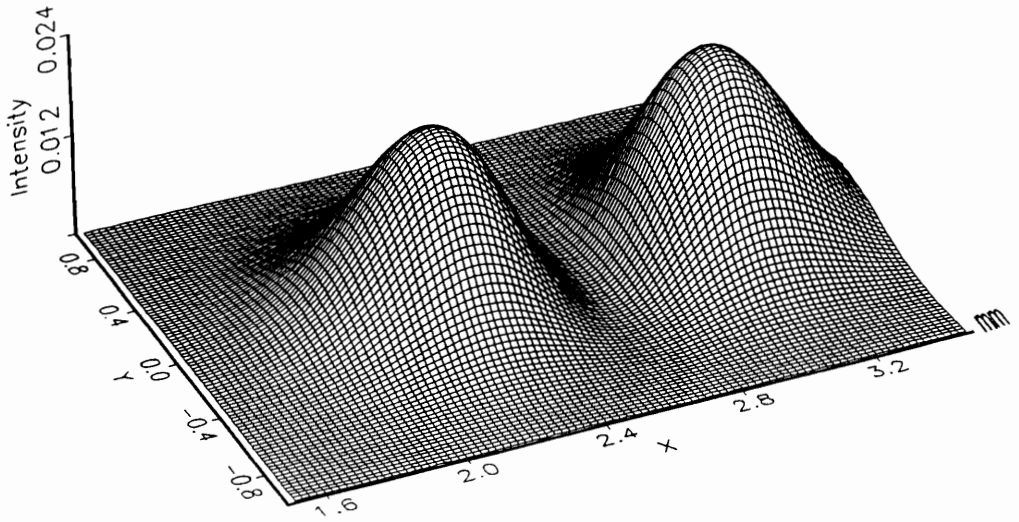

(a)

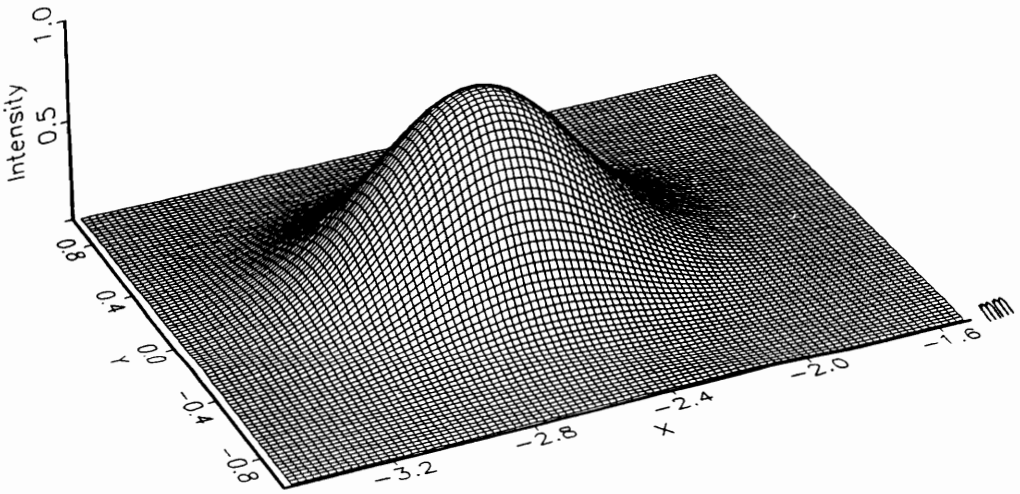

(b)

Fig. 5.13: Spatial distribution due to spectrums given in fig. 5.8, w_0 = 422 um. w_y = 10cm, w_z = 10 cm, z = 84cm, and laser beam 1mm away from transducer, (a) Zero-order, (b) First order.

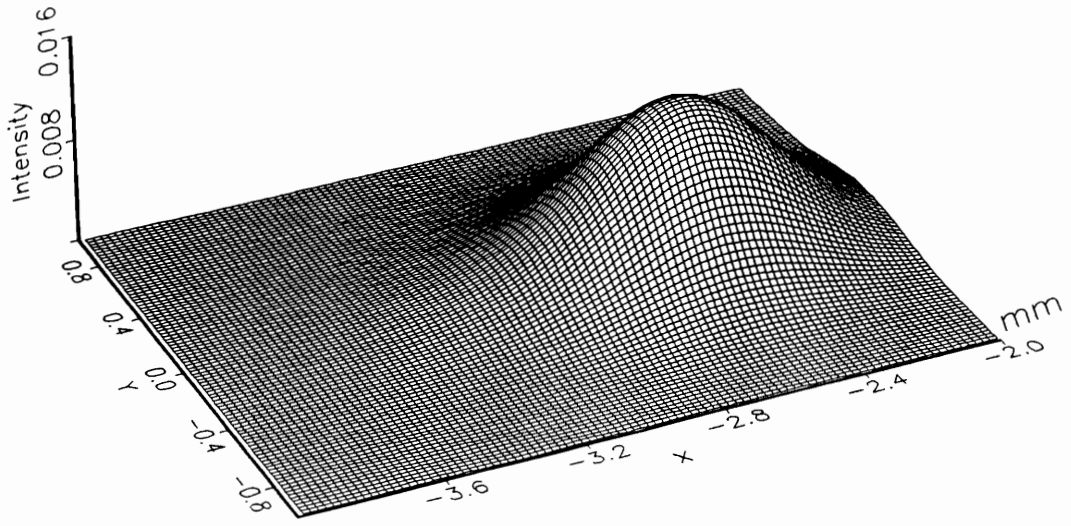

(a)

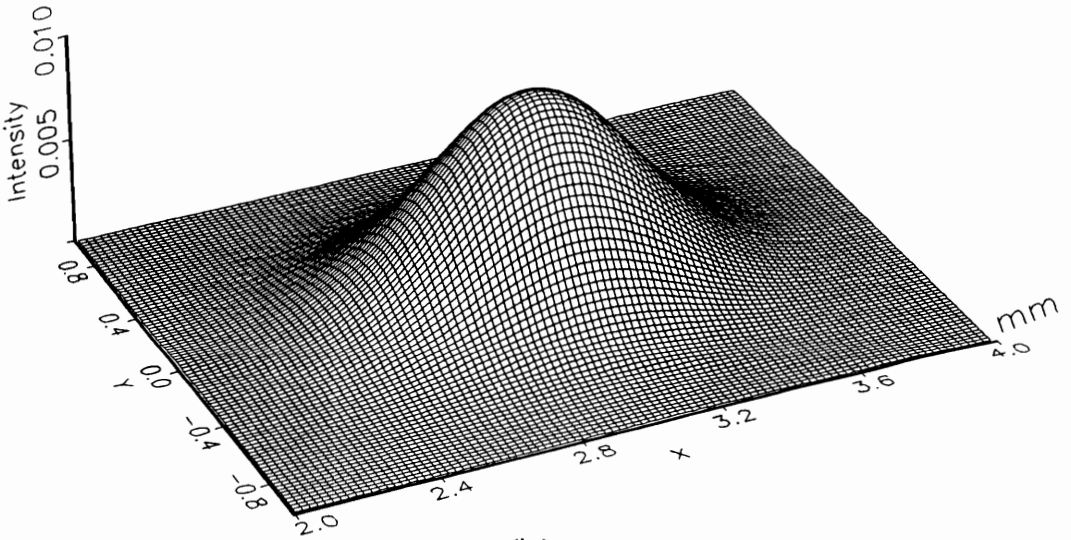

(b)

Fig. 5.14: Spatial distribution due to high order spectrums not shown in fig. 5.8, w_0 = 422 um.w_y = 10cm, w_z = 10 cm, z = 84cm, and laser beam 1mm away from transducer, (a) Minus-one order, (b) Second order.

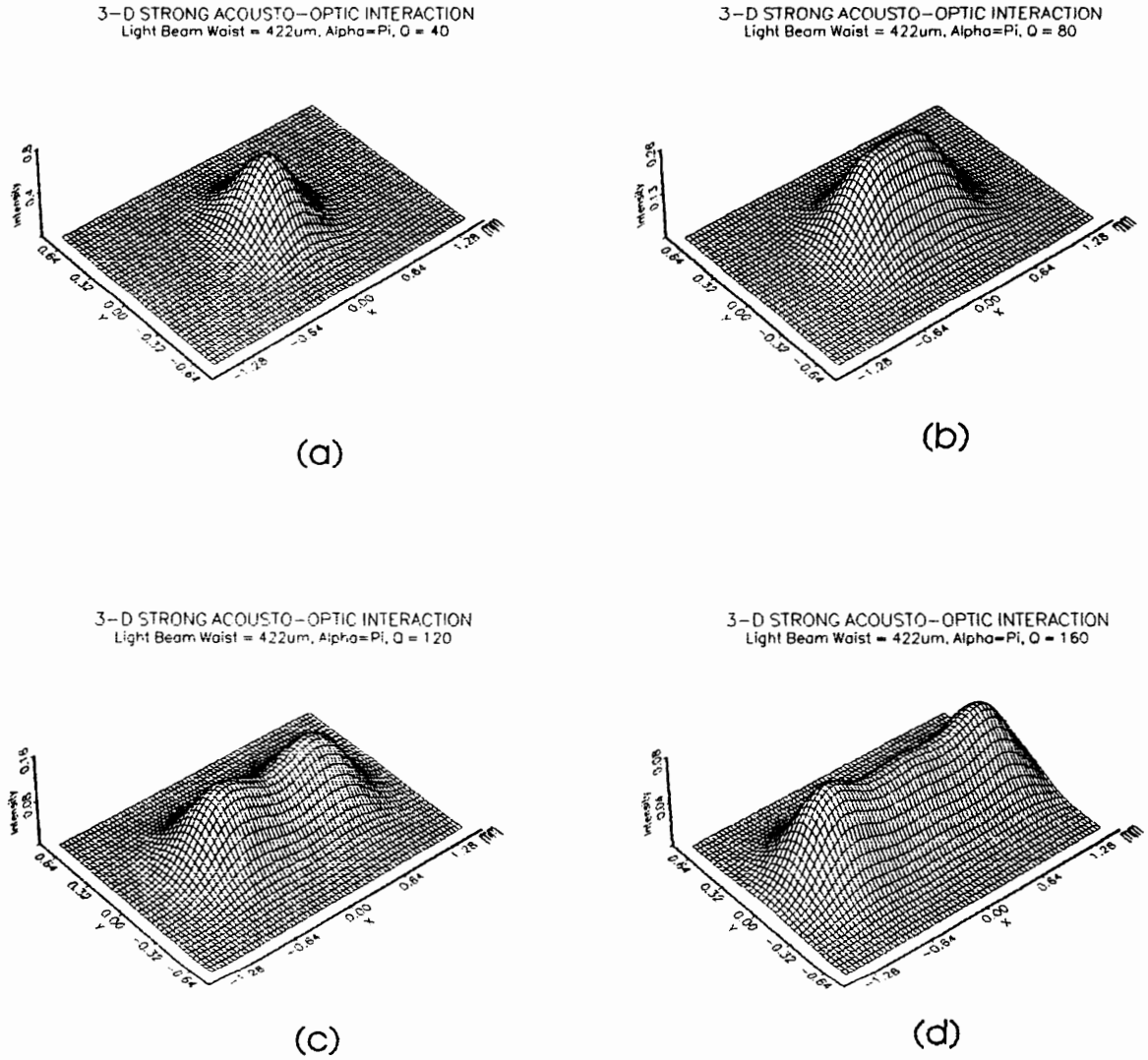

Figure 5.15: First diffracted order as a function of Q using Fourier-optics method.

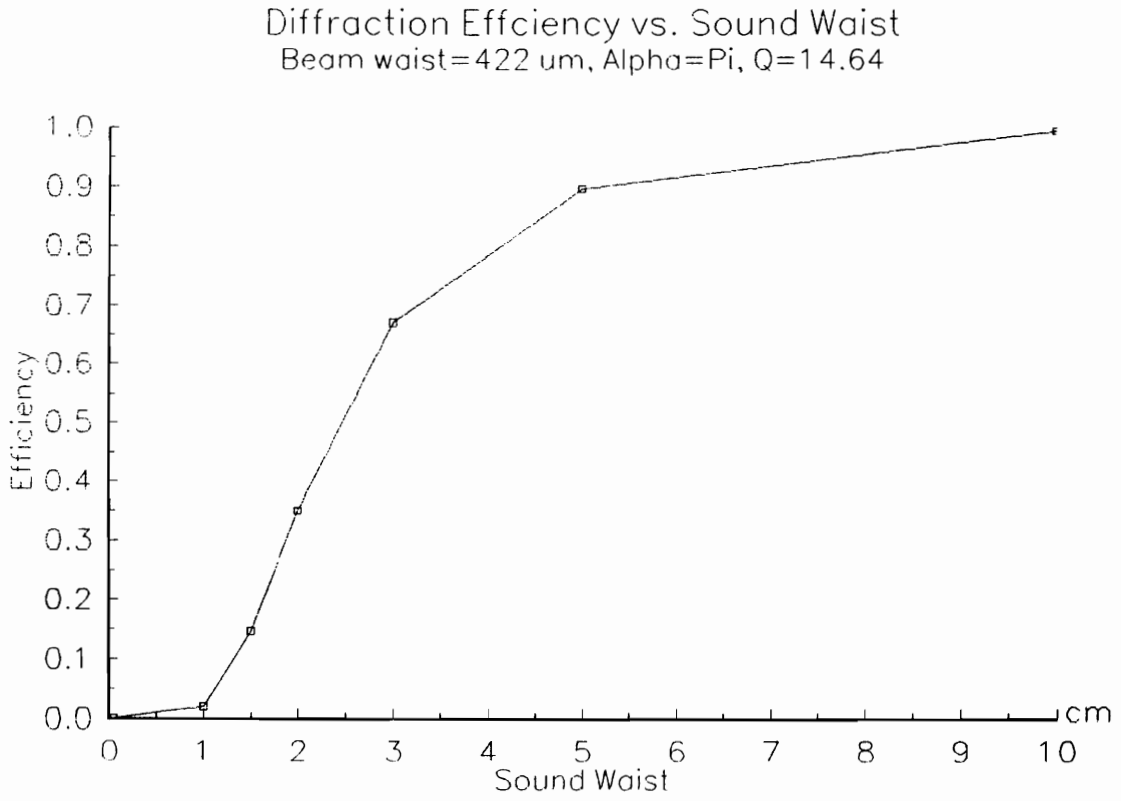

Figure 5.16: Diffraction Efficiency vs. Sound waist (w_z) when Q=14.64 and $\alpha=\pi$. w_y = 10cm, z = 84cm, and laser beam is 1mm away from transducer.

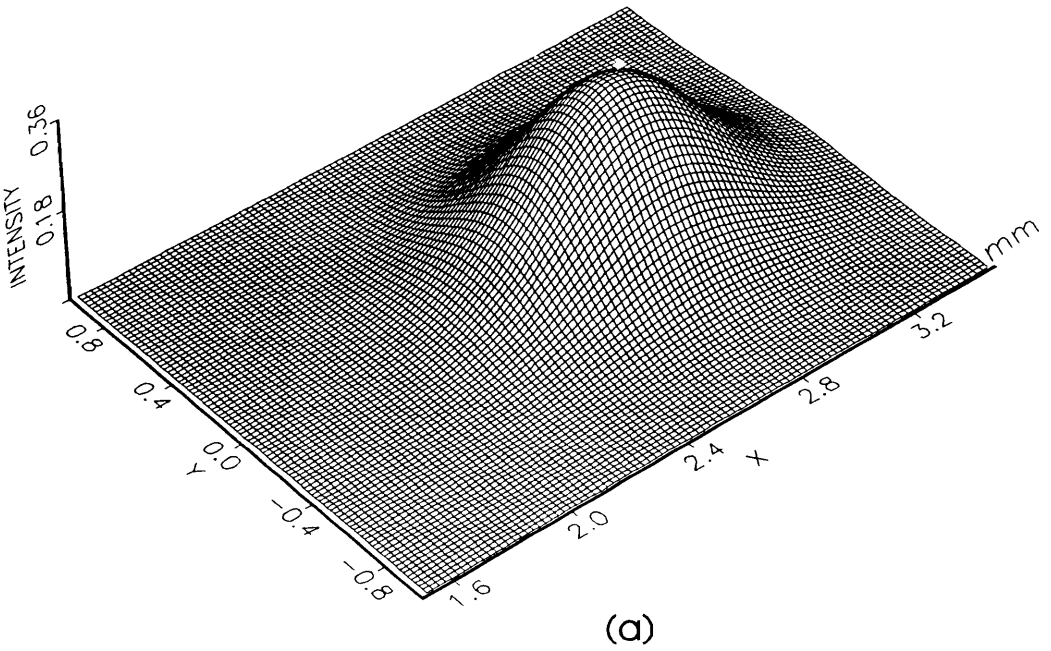

(a)

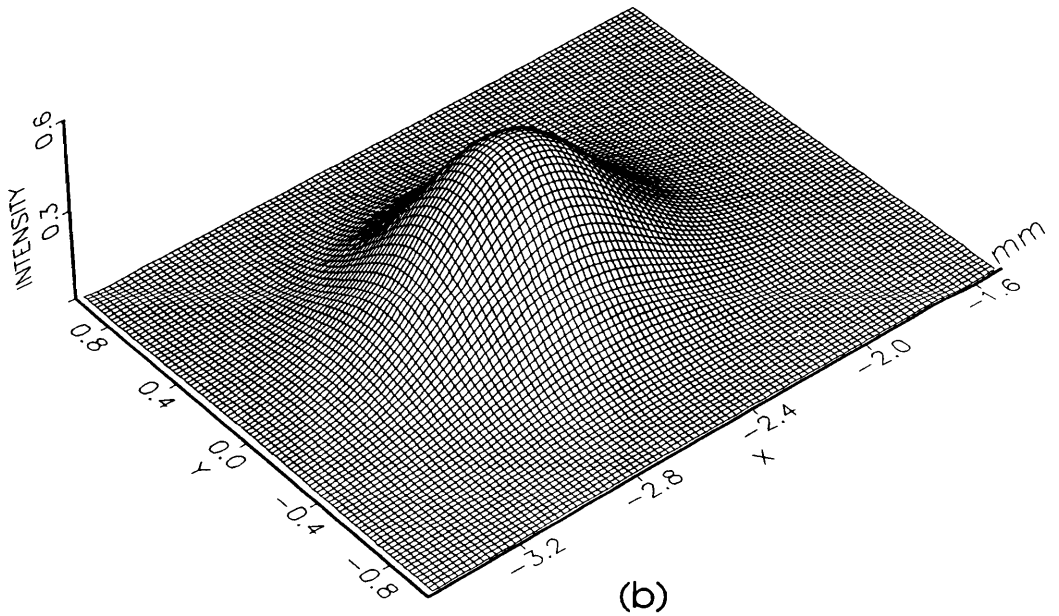

(b)

Fig. 5.17: Spatial distribution for (a) Zero-order, (b) First order when w_z = 2.0cm, w_y = 10.0cm, and the laser beam is 1mm away from transducer.

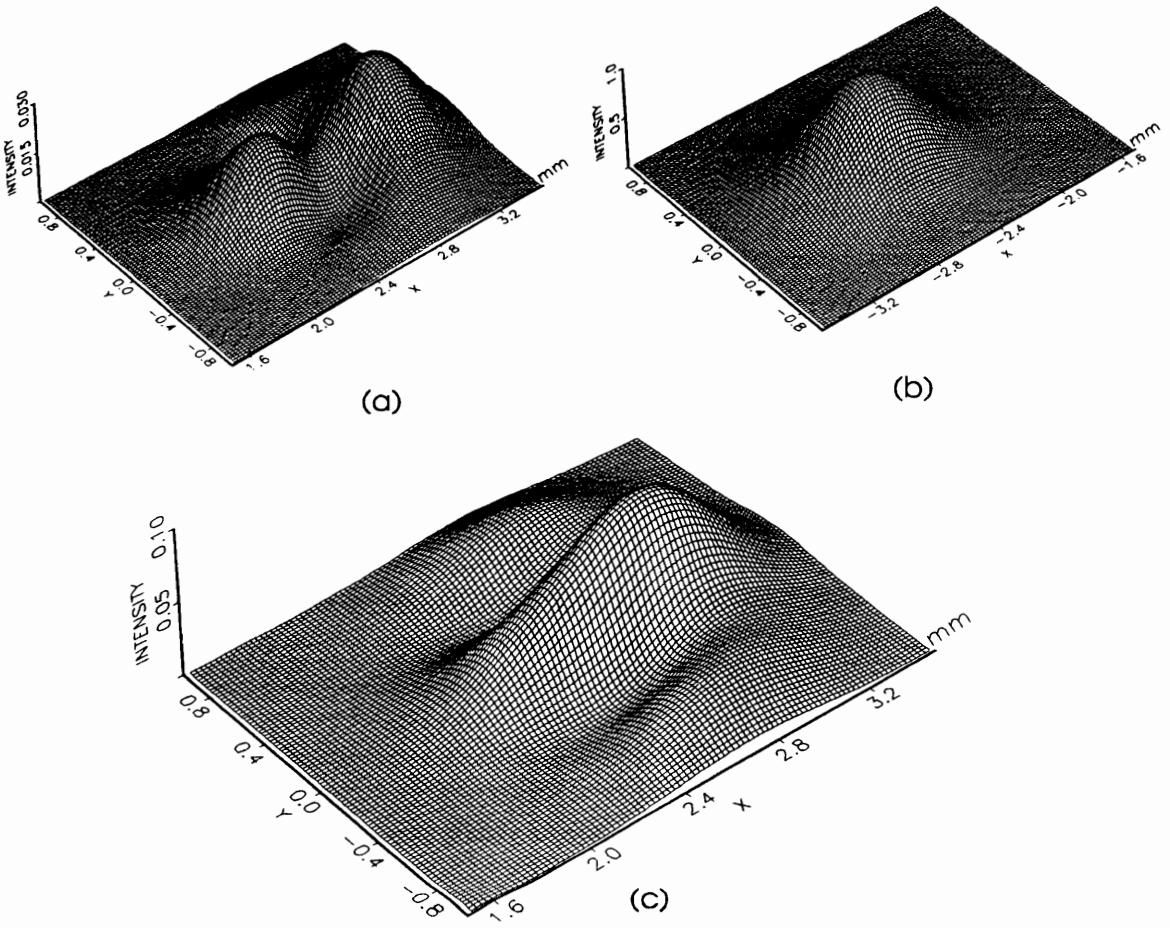

Figure 5.18: Splitting in both the x and y directions of the zero order, w_z = 10.0cm, (a) w_y = 1mm (c) w_y = 0.5mm. Laser beam is 1mm away from transducer.

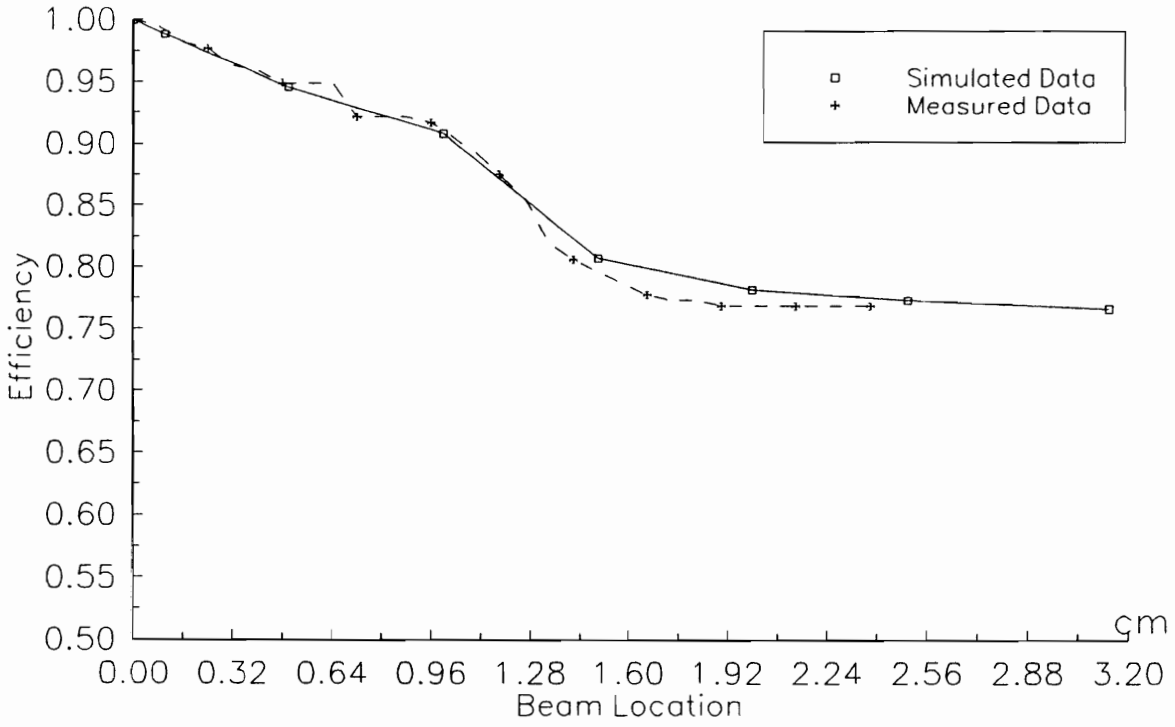

Figure 5.19: Diffraction Efficiency vs. Beam location: Q=14.64, $\alpha=\pi$, w_y = 1mm, w_z = 10cm (chosen to coincide with experimental values).

6. Physical Experiments

6.1 Basic Overview

This chapter presents experimental results that verify the split-step algorithms offered in chapter 5. Section 6.1.1 provides a detailed description of the experimental setup. We include names and model numbers of experimental equipment, detailed device parameters, and physical layout. Section 6.1.2 presents techniques used to record measured data. Where appropriate data is superimposed onto graphs previously shown in section 5.

6.1.1 Optical Setup

Figure 6.1 shows the experimental setup used to collect measured data. As seen in the figure, this is a relatively simple setup. The major components in the figure consists of a Hughes 15mW Helium-Neon (He-Ne) laser with nominal wavelength 632.8 nm, an Intraction Corporation (model AOM-40) acousto-optic modulator with a 40 Mhz center frequency and 20 Mhz bandwidth, and a laboratory built photodetector.

The light source is a continuous wave He-Ne laser with a specified beam diameter of 0.81mm measured at the $1/e^2$ power point. The beam divergence is rated at 1.0 mrad/meter. The AOM has an interaction medium made of flint glass with an index of refraction approximately equal to 1.5.[15] The length of the interaction region is 5.7 cm in the z-direction, and its height is 2.0 mm in the y-direction. The entire device is position on a rotation stage with an axis of rotation in the y-direction (vertical), where the rotation stage is used to

achieve the proper incident light beam angle necessary for Bragg diffraction. A photodetector is placed on a translation stage that moves in the x and y direction (both perpendicular to the optical axis). In addition, a 50um pinhole is placed in front of the photodiode to sample the light field at different positions within the diffracted light beam. To obtain a sample of the output light field, the translation stage is moved to position the pinhole of the detector on the positive x side and positive y side of the field and then manually moved across the field plane in the negative x direction. Once the most negative x position is reached the vertical stage is moved one step in the negative y direction and the process is repeated. Continuing this grid like sampling of the field plane allows the 2-D transverse measurement of the acousto-optically diffracted optical pattern.

Before proceeding to the experimental results, there are certain layout measurements that were taken to aide in designing better computer simulations. The distance between the laser and the acousto-optic modulator and the distance between the AOM and the photodetector has to be known to build adequate computer models of the system. This is due to normal diffraction that takes place when a coherent laser beam propagates in free space. The distance between the laser and AOM is 4.3cm, and the distance between the AOM and the photodetector is 84.0cm. Because the width of the acousto-optic cell is 5.7cm, the entire distance that the laser beam travels (outside the laser housing of course) is 94.0cm. We chose the location of the field (with respect to the optical axis) measured at the input plane of the photodetector arbitrarily with special attention paid to the separation between neighboring diffracted orders. The only criteria used was that the orders must be clearly visible by direct

human observation. One other important parameter (used in the wave-equation approach only) considers how close the laser beam is to the acousto-optic transducer when the interaction takes place. The basic idea is that the closer the laser beam is to the transducer, the more the sound wave should look like a plane wave.

6.1.2 Experimental Results

Figure 6.2 shows a one-dimensional profile of a laser beam propagated in free space. Notice that the beam waist (i.e. the distance between the $1/e^2$ points) of the incident laser beam is approximately equal to 0.422um. In the figure we assume the laser beam exits the housing of the laser and propagates 84 cm, where it is detected by a photodetector. Unpropagated data refers to the laser beam exactly at the exit of the acousto-optic cell (i.e. before propagating the additional 84 cm to the photodetector). The measured sample points taken 84cm away from the acousto-optic Bragg cell are place over the simulated curve to ensure our numerical methods are properly calibrated to our experimental setup. Normal characteristics of Gaussian wave propagation dictate that the beam spreads as it propagates. Included in this propagation is also a reduction in amplitude. This figure aides in proper calibration of the algorithm and explains why the maximum amplitude of the diffracted order is significantly less than the incident beam. Normalization of both the simulated and measured data helped to alleviate some scaling difficulties.

Figure 6.3 compares one dimensional plots of measured data with simulation results from the Fourier-optics and wave-equation approaches. We collected the data by positioning

the pinhole at the maximum intensity of the first diffracted order. To record experimental data, the translation stage was positioned to one side of the orders and moved across the entire diffraction plane. Clearly the measured data has the same qualitative shape as that shown in chapter 5 for the Fourier-optics and wave-equation approaches. In the wave-equation plots, w_y = 10cm, w_z = 10cm, and the distance away from the transducer is 84cm. In figure 6.3c the null in the zero order does not reach zero because the laser beam was incident some distance away from the acoustic transducer (about 5mm). However, when the distance between the transducer and the laser beam passing through the cell is made less than 1 mm as in figure 6.3b, the curves are closely matched. In both cases, the first diffracted order seem to be unaffected by the relatively short distance away from the transducer. Refer the section 5.4 where the effects of this distance is discussed in greater detail.

Figures 6.4a and 6.4b show two-dimensional plots of the zero diffracted order when the laser beam to transducer separation is 4.5mm and less than 1mm, respectively. Notice that in figure 6.4a, that the shape of the measured beam does not match the simulation results in figure 5.13a very well. The reason for this mismatch is that the sound wave emanating from the transducer diffracts as it propagates. The Fourier optics method does not predict this variation, however, because the wave equation approach allows the laser to be placed anywhere within the acousto-optic cell, it models the distorted zero order somewhat more accurately. Figures 6.3b and 6.3c show that the acousto-optic cell operates as expected when the laser beam moves closer to the transducer, which is of practical interest when using an actual acousto-optic cell. That is, the split in the zero diffracted order is more pronounced

in figure 6.3b. This occurs because the sound field profile better approximates a plane wave in this region. Exact modeling is not possible with either of these algorithms because the transducer present in the experimental Bragg cell is neither a plane-wave generator nor a Gaussian wave generator. It is proper to consider the sound field as a spectrum of plane waves. Since the actual Bragg cell consists of eight individual transducers, the sound field profile may not be uniform. In fact, the small differences between the measured and simulated results could be caused by a nonuniformity across the transducers. However, the wave equation approach correctly models the zero diffracted order as verified by viewing figures 6.3b, 6.4a (somewhat), and 6.4b together with 5.13a and 5.19c. Comparing figure 6.4b to figure 5.13a, it should be pointed out that the separation between the two humps are virtually equal in the two graphs. For completeness the first, minus-one and plus-two orders are shown in figure 6.5, respectively. These figures did not vary significantly when the laser beam moved from 4.5mm away from the transducer to 1mm away. Simulations regarding these orders appear in figure 5.13b and 5.14, respectively. Looking closely at the plots in these figures shows qualitative and quantitative agreement between theory and actual measurements. For example, the width of the diffracted order in figure 6.5b, the minus-1 order, is about 1.5 mm. This agrees with the width in figure 5.14c. Furthermore, if we normalize the measured minus-1 order in figure 6.5b by the peak of the measured data for the first diffracted order (.53 volts), it is seen that the normalized peak of the minus-1 order becomes about 0.014. The peak intensity of the measured minus-1 order equals 0.0072 volts. Comparing 0.014 to the normalized intensity of the simulated diffracted order in figure 5.14c

(peak intensity equal to 0.0152) shows good agreement. The difference between the two normalized peaks is attributed most likely to small errors in taking measurement since all measured data was taken by hand. Also the step size of the measure data does not correspond one-to-one with that of the calculated data. This means that it is entirely possible that the peak of the measured data we missed due to coarseness of taking the measurements. Also evident in the comparison between figures 5.14c and 6.5b is the shape of the diffracted orders. It is clear that the measure diffracted order is skewed somewhat. Figure 5.14c also shows some skewing, but not to the degree in figure 6.5b. In short, there seems to be good agreement between our simulation results and the measured data.

Lastly, we want to return to figure 5.19 to show that the wave-equation approach correctly predicts the decrease in diffraction efficiency as the incident laser beam interacts with a sound beam at different distances away from the transducer. All measurements were taken with a Newport Optical Power Meter model 1830-C by placing the acousto-optic cell together with its rotation stage onto a translation stage. This allowed the acousto-optic cell to be moved in the x-direction while the rest of the optical system (i.e. the laser and photodector) remained stable. Using an iris in front of the photodector allowed us to isolate the first diffracted order for measurement. Data was taken manually every 0.8 mm until we traversed the entire aperture of the cell. Actual measurements taken by the power meter placed the peak power for the incident and the first order diffracted beams to be $I_{inc} = 2.35$ mW and $I_1 = 2.16$ mW, respectively. Using equation (5.4-1) allowed us to calculate a measured peak diffraction efficiency equal to 92%. These numbers are consistent with the

manufactures specifications. To be consistent with figure 5.16, we plotted the diffraction efficiency with respect to the first order instead of the incident laser beam (i.e. $I_1/I_{1(max)}$). Figure 5.16 shows results that are only possible with the three-dimensional theory and correctly models the diffraction efficiency as the laser beam is incident some distance from the transducer.

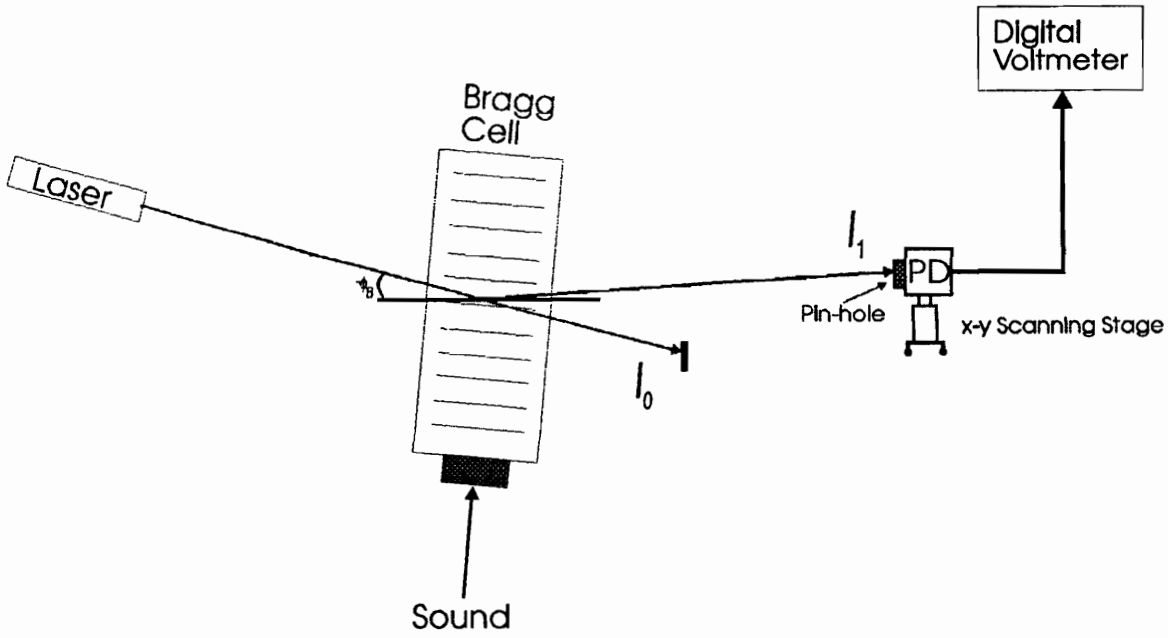

Fig. 6.1: Experimental Configuration.

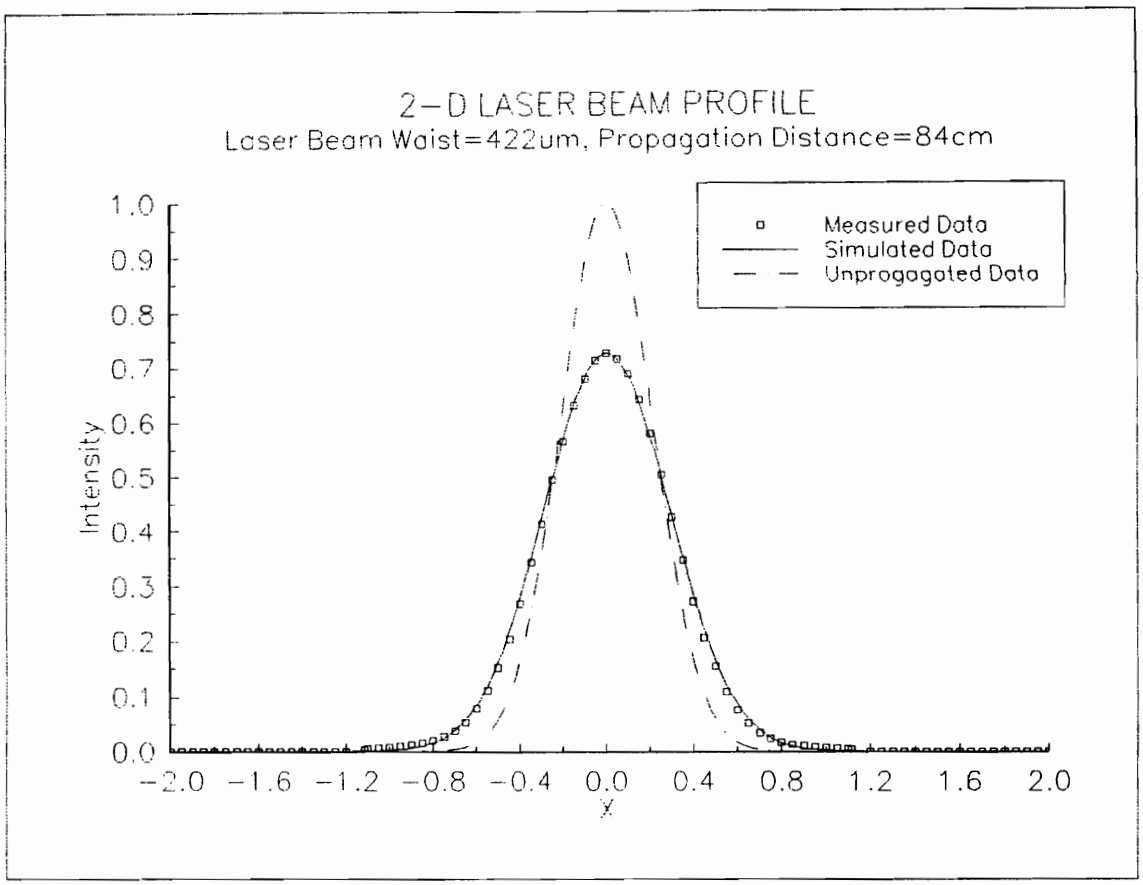

Fig. 6.2: (a) Undiffracted and diffracted laser beams profile used to calibrate the Fourier-Optics and Wave-equation split-step algorithms.

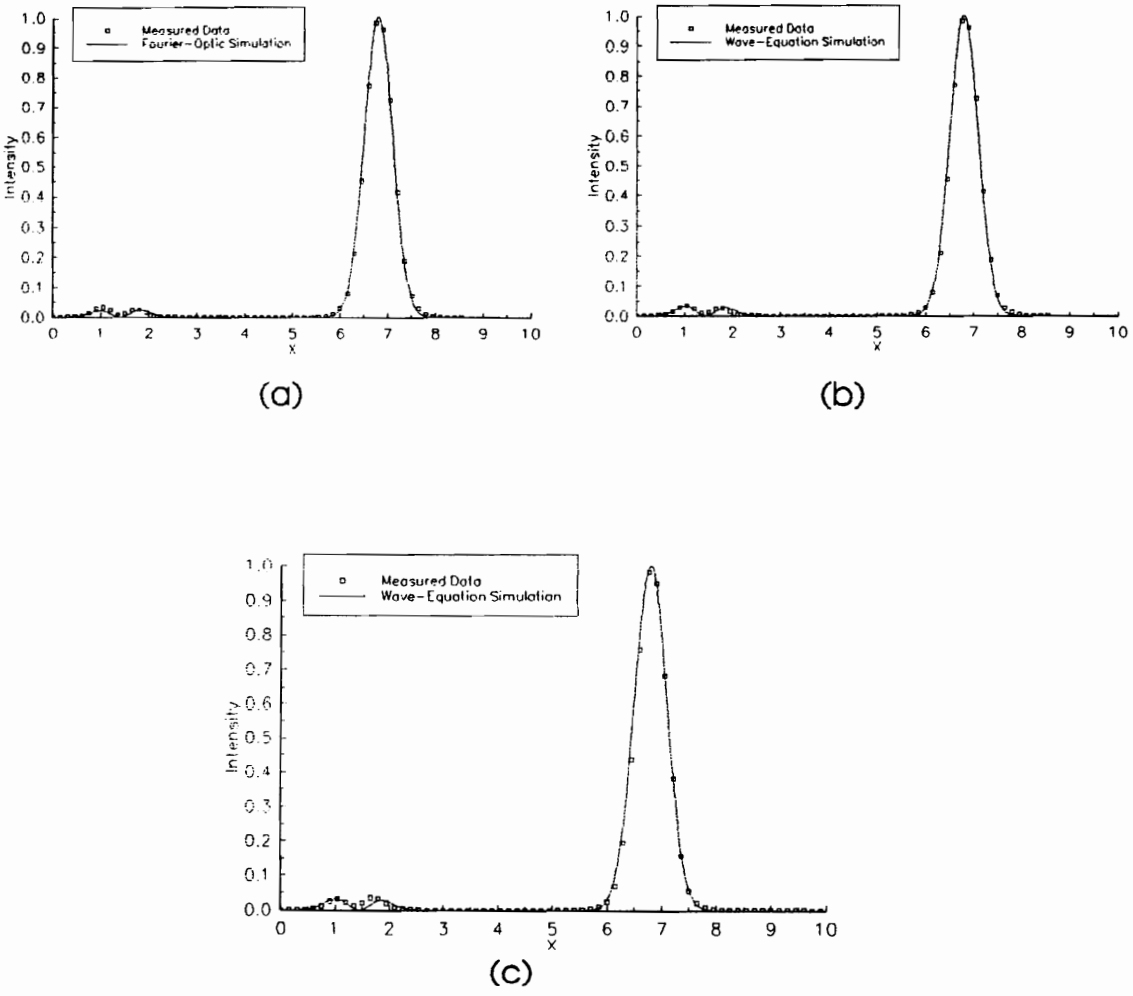

Fig 6.3: Experimental verification of (a) Fourier-optics, (b) Wave-equation with light beam 1mm from transducer, and (c) Wave-equation with light beam 5mm from transducer. w_y=10cm and w_z=10cm for wave-equation plots.

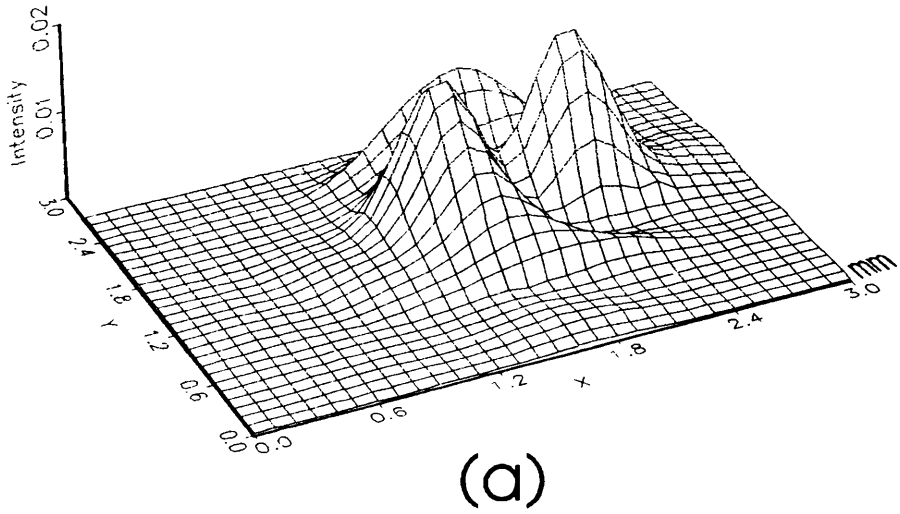

(a)

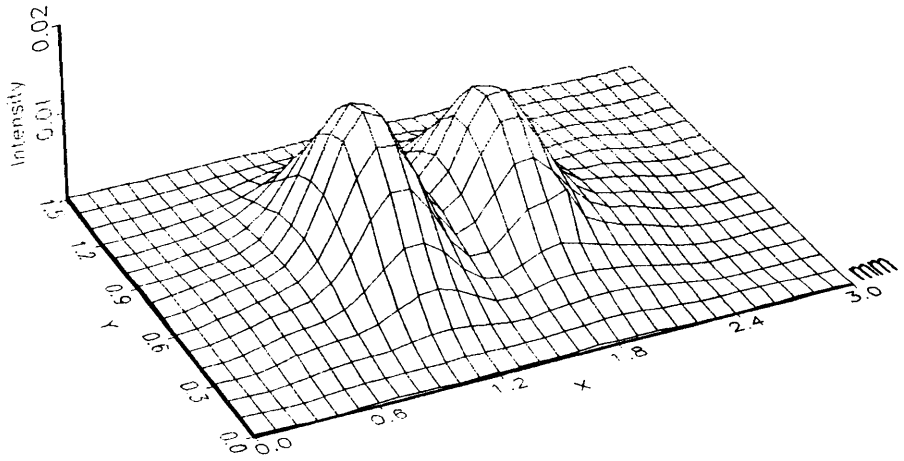

(b)

Fig. 6.4: Measured Zero diffracted order (a) Laser beam 5 mm away from transducer, (b) Laser beam 1mm from transducer.

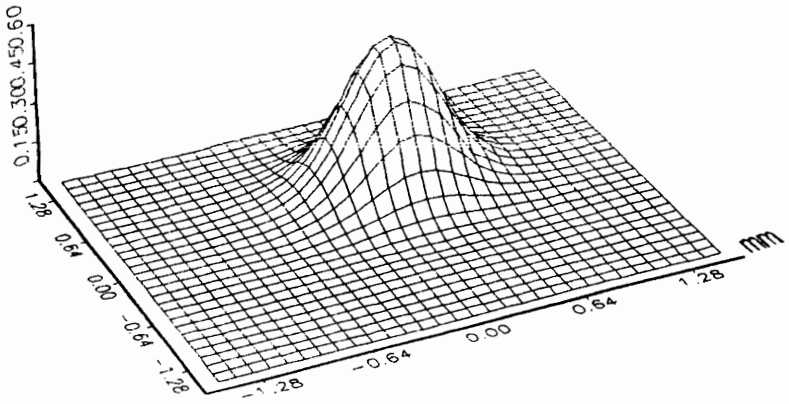

(a)

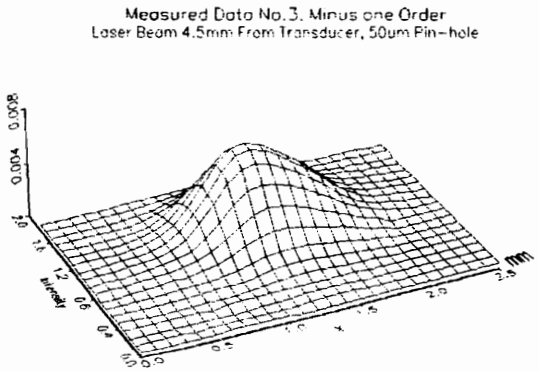

(b)

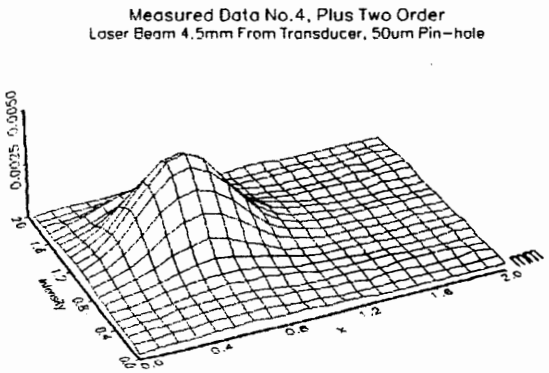

(d)

Fig: 6.5: Measured diffracted orders, (a) First order, (b) Minus-one order, and (c) Plus two- order.

7. Conclusion

7.1 General Discussion

This thesis has presented two different split-step algorithms that solve both the two-dimensional and three-dimensional acousto-optic interaction problem. Each two-dimensional method agreed qualitatively and quantitatively with previously verified analytical results. This is the first time three-dimensional results for strong acousto-optic interactions have been presented, therefore only experimental results are available for comparison. The acousto-optic modulator used in the experiments produced plane-waves very close to the transducer. Therefore, simulations that incorporated sound fields with plane wave-fronts modeled the physical system better when compared to measured data for this particular case. Three-dimensional simulations of acousto-optic interaction illustrated some distortion along the y-direction of the zero diffracted order that previous two-dimensional acousto-optic interaction theories could not even predict. Distortion in the y-direction is viewable in actual physical situations. Our Fourier-Optics approach was not able to predict the distortion along the y-direction in the zero diffracted. This inability was overcome by introducing the wave-equation approach. The wave-equation approach can have Gaussian sound fields that undergo diffraction when propagating through a sound cell. This allowed us to manipulate the effective interaction area along both the width and height of the cell (i.e. the z-direction and y-direction, respectively). By incorporating placement of the incident laser beam along the x-axis into the algorithm, we were able to show effects of diffraction. The affects of this

diffraction manifests itself by decreasing the diffraction efficiency as the location of the incident laser beam moves further away from the acoustic transducer (in the x-direction). Refer th figure 5.19 for greater clarification.

7.1.1. Summary of Original Contributions

For the first time, we have presented solutions to the three-dimensional strong acousto-optic interaction problem consisting of both arbitrary light and sound fields. In addition to solving the problem for interaction between Gaussian light profiles and a rectangular sound columns, we also introduced a three-dimensional Gaussian sound field model for the transducer. We were able to match the results of our two-dimensional models with those of a previously verified method. This achievement helped to validate the Fourier-optics and wave-equation algorithms. Our investigation into wide interaction regions (i.e. large Q) produced results that were consistent with two-dimensional theories. For the first time, we showed that curvatures along the y direction of the sound field add to the distortion of the zero diffracted order. Although an exact match with experimental results was not attained, we illustrated that different sound waist produced varying amounts of distortion. A more accurate model of the experimental transducer may lead to even better correlation between simulations and experiments.

Contrary to previous two-dimensional theories, the wave-equation method correctly predicts the decrease in diffraction efficiency as the incident light beam moves further away from the transducer (i.e. in the x direction, see figure 3.4). This finding is consistent with observed results and is due mainly to the curvature along the y direction of the sound field.

Ilustrating that it is the y dimension that causes the diffraction efficiency to decrease as the light beam is incident some distance away from the transducer has not be shown before. This may aid engineers to properly design systems that depend on the entire width of the acousto-optic cell for deflection. For instance, an image deflected in the direction of the first order will vary in its intensity distribution based on its incident location within the Bragg cell. Consequently, with acousto-optic cells' ever increasing role in future image processing systems, three-dimensional models of the interaction process are necessary and provide greater insight into the entire process. Both beam splitting and broadening of the zero and first diffracted orders can be modeled with the split-step algorithms presented in this research.

7.1.2 Current Research Directions and Goals

Although we have modeled the three-dimensional strong interaction problem with the algorithms outlined in chapter 5, additional insights into the acousto-optic process is still needed. For example, the increasing use of acousto-optic cells in the area of image processing demand accurate three-dimensional models that predict how two-dimensional images will interact with different types of sound fields. We need a generalized three-dimensional transfer function formalism similar to what is presented in chapter 4. Once the model is completed, diffracted orders and their prospective profiles can be immediately obtained from knowledge of the transfer function. The major complication to date is that a general theory to model arbitrary three-dimensional transfer functions does not exist. In addition to the modeling process, the need for acousto-optic cells capable of producing sound fields with arbitrary profiles must be constructed to accurately validate future theoretical

methods. As for the work in this thesis, additional simulations need to be run for varying values of α and Q to identify cases where the first diffracted order shows some deviation in both the x and y directions. As a starting point, one may use the transfer function formalism presented in chapter 4 to identify good candidates for distortion in the x direction. A more ambitious goal is to apply an image onto the incident optical beam to illustrate specific cases where the sound cell performs useful image processing functions. This is currently limited by the amount of computer processing power available.

8. References

1. L. Brillouin, "Diffusion de la lumiere et des rayons X par un corps transparent homogene," Ann. Phys. vol. **17**, pp. 88-122, 1922.

2. L. Magdich and V. Molchanov, "Diffraction of a divergent beam by a periodically modulated layer," Opt. Spectrosc. vol **42**, pp. 299-302, 1977.

3. R. Chu and T. Tamir, "Bragg diffraction of Gaussian beams by periodically modulated media," J. Opt. Soc. Am. vol. **66**, pp. 220-286, 1976.

4. R. Chu and T. Tamir, "Diffraction of Gaussian beams for incidence close to the Bragg angle," J. Opt. Soc. Am. vol. **66** pp. 1438-1440, 1976.

5. R. Chu and T. Tamir, "Diffraction of optical beams with arbitrary profiles by a periodically modulated media," J. Opt. Soc. Am. vol. **70**, pp. 1-6, 1980.

6. A. Korpel and T.-C. Poon, "Explicit formalism for acousto-optic multiple plane wave scattering," J. Opt. Soc. Am. vol. **70**, pp. 817-820, 1980.

7. R. Hardin and F. Tappert, "Applications of the split step Fourier method to the numerical solution of nonlinear and variable coefficient wave equations," SIAM Rev. vol. 15, 423, 1973.

8. A. Hasegawa and F. Tappert, "Transmission of stationary nonlinear optical pulses in dispersive dielectric fibers. I. Anomalous dispersion," Appl. Phys. Lett. vol. 23, p 142, 1973.

9. A. Hasegawa and F. Tappert, "Transmission of stationary nonlinear optical pulses in dispersive dielectric fibers. II. Normal dispersion, "Appl. Phys. Lett. vol. 23, p 171, 1973.

10. R. A. Fisher and W. Bischel, "The role of linear dispersion in plane wave self phase modulation," Appl. Phys. Lett. vol. 23, p 661, 1973.

11. N. N. Bojarski, "The K-space formulation of the scattering problem in the time domain," J. Acoust. Soc. Am. vol. 72, p 570, 1982.

12. P. P. Stepanichen and K. C. Benjamin, "Forward and Backward projection of acoustic fields using FFT methods," J. Acoust. Soc. Am. vol. 71, p 803, 1982.

13. G. L. Payne, D. R. Nicholson, and R. M. Downie, "Numerical solution of the Zakharov equations," J. Comput. Phys. vol. 73, p 486, 1983.

14. D. Yevick and L. Thylen, "Analysis of gratings by the beam-propagating method," J. Opt. Soc. Am. vol. 72, p 1084, 1982.

15. C. Venzke, A. Korpel, and D. Mehrl, "Improved space-marching algorithm for strong acousto-optic interaction of arbitrary fields," Appl. Opt. vol. 31, p 656, 1992.

16. A. R. Hare and G. R. Morrison, "Near-field soft X-ray diffraction modelled by the multislice method," J. Mod. Opt. vol. 41, p 31, 1994.

17. P. Debye and F. W. Sears, "On the scattering of light by supersonic waves," Proc. Nat. Acad. Sci. vol. 18, p 409, 1932.

18. R. Lucas and P. Biquard, "Proprietes optiques des milieux solides et liquides soumis aux vibration elastiques ultra sonores," J. Phys. Rad. vol. 3, p 464, 1932.

19. L. Brillouin, "La diffraction de la lumiere par des ultrasons," Act. Sci. Indust. vol. 59, p 1, 1933.

20. C. V. Raman and N. S. Nagendra Nath, "The diffraction of light by high frequency sound waves, Proc. Ind. Acad. Sci. vol. 2, p 406, 1935.

21. Lord Rayleigh, "The theory of sound," vol. II, sect. 272a. Dover, New York, 1945.

22. C. V. Raman and N. S. Nagendra Nath, "The diffraction of light by high frequency sound waves," Proc. Ind. Acad. Sci. vol. 2, p 413, 1935.

23. C. V. Raman and N. S. Nagendra Nath, "The diffraction of light by high frequency sound waves, Proc. Ind. Acad. Sci. vol. 3, p 75, 1936.

24. C. V. Raman and N. S. Nagendra Nath, "The diffraction of light by high frequency sound waves, Proc. Ind. Acad. Sci. vol. 3, p 119, 1936.

25. C. V. Raman and N. S. Nagendra Nath, "The diffraction of light by high frequency sound waves, Proc. Ind. Acad. Sci. vol. 3, p 459, 1936.

26. P. H. Van Cittert, "Zur Theorie der Lichtbeugung and ultraschallwallen," Physica IV, p 540, 1937.

27. A. B. Bhatia and W. J. Noble, "" Proc. Roy. Soc. Ser. A vol. 220, p 356, 1953.

28. P. Phariseau, "On the diffraction of light by progressive supersonic waves," Ind. Acad. Sci. vol. A44, p 165, 1956.

29. R. Extermann, "" Helv. Phys Acta 10, p185, 1937.

30. W. R. Klein and B. D. Cook, "Unified approach to ultrasonic light diffraction," IEEE Trans. sonics untrson., vol. SU-14, p 723, 1967.

31. B. Benlarbi, P. St. J. Russell, and L. Solymar, "Bragg diffraction of finite beams by thick gratings: two rival theories," Appl. Phys. B vol. 28, p 63, 1982.

32. R. R. Aggarwal, "Diffraction of light by ultrasonic waves (deduction of different theories from the generalized theory of Raman and Nath) Proc. Ind. Acad. Sci. Sect. A vol. 37, p 417, 1950.

33. G. Benedek and T. Greytak, "Brillouin scattering in liquids," Proc. IEEE. vol. 53, p 1623, Oct. 1965.

34. R. W. Dixon and E. I. Gordon, "Acoustic light modulator using optical heterodyne mixing," Bell System Tech. J. vol. 56, p 367, 1967.

35. L. E. Hargrove, "Effects of ultrasonic waves on Gaussian light beams with diameter comparable to ultrasonic wavelength," J. Acoust. Soc. Am. vol. 43, p 857, 1968.

36. A. Korpel, "Visualization of the crossection of a sound beam by Bragg diffraction of light," Appl. Phys. Lett. vol. 9, p 425, 1966.

37. E. I. Gordon, "A Review of acousto-optical deflection and modulation devices," Proc. IEEE, vol. 54, p 1391, 1966.

38. R. Adler, "Interaction between light and sound," IEEE Spectrum, vol. 69, p 48, 1981.

39. A. Korpel, "Acousto-optics, a review of fundamentals," Proc. IEEE vol. 69, p 48, 1981.

40. O. Leroy and J. Claeys, "Diffraction of light by profiled ultrasound," Acustica vol. 55, p 21, 1984.

41. R. Pieper, A. Korpel, and W. Heremn, "Extension of the acousto-optic Bragg regime through a Hamming apodization of the sound field," J. Opt. Soc. Am. A, vol. 3, p 1608, 1986.

42. M. R. Chatterjee, T.-C. Poon and D. N. Sitter Jr., "Transfer function formalism for strong acousto-optic Bragg diffraction of light beams with arbitrary profiles," Acustica vol. 71, p 81, 1990.

43. A. Korpel and W. Bridge, "A Monte Carlo simulation of the Feynman diagram approach in strong acousto-optic interaction," J. Opt. Soc. Am. A, vol. 7, p 1503, 1990.

44. R. Wolfe, "Applied Solid State Science - Advances in materials and device research," Academic Press, New York, 1972.

45. T.-C. Poon and P. P. Banerjee,"Principles of Applied Optics," Richard D. Irwin, Inc., and Asken Associates, Inc., 1991.

46. B. E. A. Saleh and M. C. Teich, "Fundamentals of Photonics," John Wiley and Sons, Inc., 1991.

47. H. Kogelnik, "Coupled wave theory for thick hologram gratings," Bell Syst. Tech J. Vol. 48, p 2908, 1969.

48. P. P. Banerjee and C. Tarn, "A Fourier transform approach to acousto-optic interaction in the presence of propagational diffraction," Acustica vol. 74, p 181, 1991.

49. S. Min and M. R. Chatterjee, "General integral formalism for acousto-optic and holographic Bragg scattering for arbitrary profiles and orientations," Acustica vol. 71, p 81, 1990.

50. M. D. McNeill and T.-C. Poon, "Gaussian beam profile shaping by acousto-optic Bragg diffraction," Appl. opt. vol. 33, p 4508, 1994.

51. A. Korpel, "Acousto-Optics," Marcel Dekker, Inc., New York, 1988.

52. A. Korpel, H. H. Lin, and D. Mehrl, "A convenient operator formalism for Fourier optics and inhomogeneous and nonlinear wave propagation," J. Opt. Soc. Am. A vol. 6, p 630, 1989.

53. W. H. Press, S. A. Teukolsky, W. T. Vetterling, and B. P. Flannery, "Numerical Recipes in C, The art of scientific computing," second edition, Cambridge University Press, 1992."

9. Vita

Mark McNeill was born on June 8, 1965 in Richmond, Virginia and lived in Ruther Glen, Virginia during his entire childhood. While in high school, Mark participated in the band, lettered in varsity football, and served as vice-president of the science club. He graduated with honors from Caroline high school in 1983. After graduation, Mark entered North Carolina Agriculture and Technical State University (A&T) and began his quest for a bachelors degree in Electrical Engineering. While attending A&T, he received a scholarship from the university for his outstanding academic performance. Mark also received summer employment with General Electric in Wilmington, North Carolina and American Telephone and Telegraph Company (AT&T) in Indianapolis, Indiana. He graduated Summa Cum Laude from NC A&T in May, 1987. He joined AT&T Bell Laboratories in Naperville, Illinois in June, 1987 and began his career as a systems engineer. By participating in AT&T's one year on campus program, Mark attended Cornell university for his Master's degree in electrical engineering. He received his degree in August of 1988. Mark rejoined AT&T and worked on several interesting projects involving their premiere telephone switching system. In August of 1990, Mark left AT&T to start work toward his Ph.D. degree at Virginia Tech. Mark joined the Optical Image Processing Laboratory under the direction of Dr. Ting-Chung Poon. He worked on many projects involving acousto-optic interaction. Mark joined the faculty at Bucknell University in Lewisburg, PA (where he currently resides) in January, 1995 as an assistant professor. He successfully defended his dissertation on February 9, 1996.